

MICROCOPY RESOLUTION TEST CHART  
NATIONAL BUREAU OF STANDARDS-1963-A

Unclassified

SECURITY CLASSIFICATION OF THIS PAGE (When Data Entered)

*Witt* (2)

REPORT DOCUMENTATION PAGE

READ INSTRUCTIONS BEFORE COMPLETING FORM

1. REPORT NUMBER 2. GOVT ACCESSION NO. 3. RECIPIENT'S CAT. LOG. NUMBER

AFOSR-TR-88-0032 AD-A126445

TITLE (and Subtitle)  
The Surface Structure, Scattering Losses and Schottky Barrier Model of III-V Compound Semiconductors

5. TYPE OF REPORT & PERIOD COVERED  
Final Report  
9/28/79 - 9/30/82

6. PERFORMING ORG. REPORT NUMBER

AUTHOR(s)  
Bansang W. Lee  
Associate Professor

8. CONTRACT OR GRANT NUMBER(s)  
AFOSR-79-0136D

PERFORMING ORGANIZATION NAME AND ADDRESS  
Department of Electrical Engineering  
Rutgers University  
Piscataway, NJ 08854

10. PROGRAM ELEMENT, PROJECT, TASK AREA & WORK UNIT NUMBERS  
2305/C1 6/11/82

CONTROLLING OFFICE NAME AND ADDRESS  
Air Force Office of Scientific Research/AE  
Building 410  
Bolling AFB, Washington, DC 20332

12. REPORT DATE  
December 21, 1982

13. NUMBER OF PAGES  
158

MONITORING AGENCY NAME & ADDRESS (if different from Controlling Office)

15. SECURITY CLASS. (of this report)  
Unclassified

15a. DECLASSIFICATION/DOWNGRADING SCHEDULE

16. DISTRIBUTION STATEMENT (of this Report)

Approved for Public Release, Distribution Unlimited

17. DISTRIBUTION STATEMENT (of the abstract entered in Block 20, if different from Report)

DTIC ELECTRIC  
S APR 06 1983 D  
E

18. SUPPLEMENTARY NOTES

*to be*  
Published in Journal of Vacuum Science and Technology (in two papers)  
19(3), 1981, pp. 294-300; 21(2), 1982, pp. 577-584.

19. KEY WORDS (Continue on reverse side if necessary and identify by block number)

Surface Atomic Structure, Schottky Barrier Formation, Surface Scattering Losses, III-V Compound Semiconductors

20. ABSTRACT (Continue on reverse side if necessary and identify by block number)

The surface atomic structure of GaP (110) has been determined by low energy electron diffraction (LEED) analysis, which was done via direct comparison of LEED intensities calculated using dynamical (multiple-scattering) programs with experimental data measured at room temperature. The final best-fit structure reveals that the surface P atoms protrude from the ideal surface plane, whereas the Ga atoms are rotated inwards from the plane by an angle of 27°. Further, the outmost interlayer spacing contracts by 5%.

AD A 126445

DTIC FILE COPY

Unclassified

SECURITY CLASSIFICATION OF THIS PAGE(When Data Entered)

A metal-amorphous film-semiconductor (MAS) configuration is suggested to be the physical model of a real Schottky-barrier structure. Based on the MAS model, the origin of Fermi-level pinning, the deviation of the diode ideality factor from its unity value and the transition of interface electronic behavior between covalent and ionic semiconductors have been discussed.

Laser scattering technique was utilized to investigate the surface scattering losses of GaAs waveguides. The result shows that the degrees of surface roughness are proportional to the grit size used to polish the substrate surface.

Unclassified

SECURITY CLASSIFICATION OF THIS PAGE(When Data Entered)

AFOSR-TR- 83-0032

THE SURFACE STRUCTURE, SCATTERING LOSSES AND  
SCHOTTKY BARRIER MODEL OF III-V COMPOUND SEMICONDUCTORS

*AFOSR-79-0136*

Professor Bansang W. Lee

Electrical Engineering

Rutgers, The State University of New Jersey

*Final*

Accession For	
NTIS GRA&I	<input checked="" type="checkbox"/>
DTIC TAB	<input type="checkbox"/>
Unannounced	<input type="checkbox"/>
Justification	
By _____	
Distribution/	
Availability Codes	
Dist	Avail and/or Special
<b>A</b>	



88 04 05 156

## ABSTRACT

### The Surface Structure, Scattering Losses and Schottky Barrier Model of III-V Compound Semiconductors

Professor Bansang W. Lee

The surface atomic structure of GaP (110) face has been determined by low energy electron diffraction (LEED) analysis. LEED intensities have been recorded for the (110) and (111) faces of GaP. An analysis of the structure of the (110) surface of GaP is performed by comparing LEED intensities calculated using dynamical multiple scattering programs with those measured at room temperature. The intralayer multiple scattering is treated exactly using direct summation method, while for the interlayer multiple scattering, the renormalized-forward-scattering method is used. The resulting best-fit structure suggests that the P atoms protrude from the GaP (110) surface plane, whereas the Ga atoms are rotated inward from the plane by angle of  $27^\circ$ , and the surface layer is compressed by 5%. The recorded LEED intensity profiles for GaP (111) have been analyzed. The result suggests that a good Schottky contact would be relatively easy to obtain on the GaP (111) face.

Schottky barriers have been fabricated on n-type GaP (111) crystals. Capacitance-voltage and current-voltage measurements were performed to analyze the electrical properties of the Schottky diodes.

Auger electron spectroscopy data were used to characterize the interface chemical composition. A metal-amorphous film-semiconductor (MAS) configuration is suggested to be the physical structural model of a real Schottky barrier. Based on the MAS structural model, the origin of Fermi-level pinning, the deviation of the diode factor from its ideal value and the transition of interface electronic behavior between covalent and ionic semiconductors have been explained and discussed.

The surface-scattering losses of GaAs waveguide have been investigated. The simple theory of surface scattering and the effective index approximation were combined to calculate surface-scattering losses of a rib waveguide. Different degrees of surface roughness were prepared by polishing the GaAs substrates with alumina powders of different particle sizes. Laser scattering technique was then conducted to characterize the surface geometry of these substrates. The result shows that the degrees of surface roughness of the substrates were proportional to the grit size used to polish them.

## TABLE OF CONTENTS

	PAGE
LIST OF FIGURES	
LIST OF TABLES	
CHAPTER 1	
INTRODUCTION.....	1
CHAPTER 2	
TECHNICAL BACKGROUND.....	7
2.1 Review of Theoretical Formulation for Determination of The Atomic Structure of Solid Surface by Low Electron Intensity Analysis.....	7
2.1.1 Introduction.....	7
2.1.2 Notation for Surface Structure...	8
2.1.3 The Diffraction Pattern.....	12
2.1.4 Physical Model Used in LEED Intensity Calculation.....	16
2.1.5 Dynamical Formulation of LEED....	22
2.2 Theoretical Calculation of Surface Scattering Theory.....	36
2.2.1 Introduction.....	36
2.2.2 Theoretical Calculation of Surface Scattering of a Symmetric Slab Waveguide.....	37
2.2.3 Simple Theory of Surface Scattering for an Asymmetric Slab Waveguide.....	46
2.2.4 The Surface Scattering Losses of a Rectangular Dielectric Waveguide.....	49

TABLE OF CONTENTS (CONTINUED)

	PAGE
CHAPTER 3	
EXPERIMENTAL METHODS.....	55
3.1 Auger Electron Spectroscopy (AES).....	55
3.2 Laser Scattering.....	61
3.3 Anodic Oxidation.....	65
3.4 Electrical Measurements.....	67
3.4.1 Resistivity Measurements.....	67
3.4.2 Current-Voltage (I-V) Characteristics.....	70
3.4.3 Capacitance-Voltage (C-V) Measurement.....	72
3.4.4 Capacitance-Frequency (C-f) and Conductance-Frequency (G-f) Measurements.....	74
CHAPTER 4	
ATOMIC STRUCTURE OF GaP (110) FACE.....	76
4.1 Introduction.....	76
4.2 Experimental Considerations.....	78
4.3 Model and Theoretical Considerations.....	82
4.4 Surface Structure of GaP (110) Face.....	84
4.5 Discussion and Conclusion.....	94

TABLE OF CONTENTS (CONTINUED)

	PAGE
CHAPTER 5	
STRUCTURE MODEL OF III-V COMPOUND SEMICONDUCTOR SCHOTTKY BARRIERS.....	97
5.1 Introduction.....	97
5.2 Structural Model.....	99
5.3 Outline of Experiments.....	102
5.4 Results and Discussion.....	104
5.5 Conclusions.....	125
CHAPTER 6	
INVESTIGATION OF SURFACE-SCATTERING LOSSES OF GaAs WAVEGUIDE.....	126
6.1 Introduction.....	126
6.2 Surface Scattering and Losses.....	128
6.3 Outline of Experiments.....	135
6.4 Results and Discussion.....	137
CHAPTER 7	
SUMMARY AND CONCLUSION.....	145
REFERENCES.....	149
APPENDIX.....	154
VITA.....	159

## LIST OF FIGURES

	PAGE
2.1 Two-dimensional array of unit meshes.....	10
2.2 (a) The five real two-dimensional unit meshes (b) The corresponding reciprocal two-dimensional unit meshes.....	10
2.3 Two examples of Wood's notation for surface structures.....	11
2.4 Generation of LEED pattern from a two-dimensional lattice.....	15
2.5 Cross section normal to the surface, showing the potential inside the crystal and the arrangement of the layers.....	28
2.6 Block diagram of a dynamical computer program.....	35
2.7 Cross section view of a slab waveguide.....	41
2.8 A asymmetric waveguide.....	47
2.9 Cross section of a rectangular dielectric waveguide with dimensions a and b.....	51
3.1 The x-ray energy level diagram of silicon.....	56
3.2 Schematic of the experimental arrangement used for obtained Auger spectra.....	60
3.3 A schematic diagram of laser scattering measurement..	63
3.4 The area scanned by incident laser beam.....	64
3.5 Experimental setup for anodic oxidation.....	66
3.6 Correction factor for resistivity measurement using a four-point probe.....	69
3.7 Resistivity measurement using Van-Der Pauw method....	69
3.8 I-V measurement using electrometer.....	71
3.9 C-V measurement using Boonton capacitance meter.....	73
3.10 C-f and G-f measurements using lock-in amplifier.....	75

LIST OF FIGURES (CONTINUED)

	PAGE
4.1 Schematic diagram of the ultra high vacuum (UHV) system equipped with LEED, AES and ion-sputtering gun for surface analysis.....	80
4.2 Arrangement of surface atom for GaP (110) face.....	81
4.3 (0,1) beam LEED intensity profile of GaP (110).....	90
4.4 (1,0) beam LEED intensity profile of GaP (110).....	91
4.5 (0,1) beam LEED intensity profile of GaP (110).....	92
4.6 (1,1) beam LEED intensity profile of GaP (110).....	93
4.7 Room temperature LEED pattern of GaP (111) face taken at 146V.....	96
5.1 The structural model and equivalent circuit of a real Schottky diode.....	101
5.2 I-V curves of GaP (111) Schottky diodes with various metal film.....	105
5.3 1/C-V curves of GaP (111) Schottky diodes with various metal film.....	106
5.4 AES depth-composition profile of sample No. 3.....	109
5.5 AES depth-composition profile of sample No. 5.....	110
5.6 AES depth-composition profile of sample No. 6.....	111
5.7 AES depth-composition profile of sample No. 8.....	112
5.8 The amorphous resistance versus frequency at zero bias.....	116
5.9 Frequency dependence of the dielectric constant for the amorphous film.....	117
5.10 I-V characteristic of sample Nos. 3 and 8.....	122
5.11 J versus V.....	123
5.12 Interface behavior S values plotted versus chemical heat of formation.....	124

LIST OF FIGURES (CONTINUED)

	PAGE
6.1 Cross section and top view of a rib waveguide.....	129
6.2 A circular plot of intensity vs. rotation angle for sample No. 1.....	138
6.3 The BRDF values of sample No. 1 obtained by scanning along the direction where maximum scattered occurred.....	139
6.4 Average BRDF values obtained by averaging perpendicular to the direction of scan.....	140
6.5 The overall average number (surface roughness) plotted versus the grit size of polishing powders for sample 1 through sample 5.....	143
6.6 The overall average number of samples 6 through 10 plotted versus the grit size of polishing powders.....	144

LIST OF TABLES

	PAGE
4.1 Surface structure for the GaP (110) face.....	89
5.1 Results of C-V and I-V measurements.....	107
5.2 Characteristics of amorphous film found in the GaP (111) Schottky diodes.....	115
6.1 Surface roughness of GaAs samples 1 through 10.....	142

## INTRODUCTION

III-V compound semiconductors are used widely in solid state electronic devices such as light emitting diodes (LED), Gunn effect oscillators, and high frequency field effect transistors on account of their direct and relatively large bandgaps. The free surface properties of III-V compound semiconductors differ profoundly from those of the elemental semiconductors. These differences include surface crystallography, electronics surface states and surface chemical activity. A special role has been played by GaAs and other III-V compound semiconductors, which appear to be promising in promoting monolithic integrated optical circuits. All optical function must be obtained in a single substrate in monolithic integrated optical circuits. The optical components needed to perform complex optical functions can be fabricated in a single crystal of GaAs. Most of the III-V compound semiconductors have large electro-optic effect and good electrical properties for lasering, waveguiding, modulating, switching and detecting of optical signals. The most promising substrate material known to date is GaAs. However, the optical transmission losses in GaAs waveguides cannot be reduced to an acceptable level by the present technologies for material preparation. A detailed understanding of the magnitude of the propagation loss in semiconductor waveguides is needed. Recognizing the useful application and the urgent needs in the field of optical electronics, it is necessary to gain a quantitative

understanding of the free surface and interface properties of the III-V compound semiconductors in order to develop a fabrication technology of the same quality that exists for silicon-based devices.

One of the most fundamental types of information needed about solid surfaces concerns the relative atomic positions. The geometrical arrangement of surface atoms influences most physical and chemical properties of surfaces, such as electronic surface states, oxidation, contact potentials and crystal growth. It has been found that low energy electron diffraction (LEED) is a successful tool to determine the relative atomic positions at surfaces. Incident electrons in the energy range 10-400eV penetrate not more than 5-10<sup>0</sup>Å into the surface region. The wave interference basic to LEED contains an abundance of information about the geometrical configuration of atoms at surfaces. LEED can be used quantitatively to determine the atomic structure of single crystal.

In this thesis, LEED and Auger electron spectroscopy are used to investigate the free surface properties of GaP. Modern surface analytical techniques and standard I-V (current-voltage) and C-V (capacitance-voltage) techniques are applied to characterize the physical mechanism for the metal-semiconductor interaction and formation of the Schottky barriers. In regard to the waveguide transmission losses and surface roughness, a quantitative characterization of the surface "smoothness" of GaAs substrate has been made before the substrate is fabricated into a waveguide, and this qualitative information of the surface will be used to develop the

correlation between the surface roughness and scattering losses of the waveguide.

The theoretical formulism for LEED intensity analysis is reviewed in the first part of the next chapter. The notation of surface structure and the physical origin of the LEED patterns are first described and then the physical model for a one-electron schrodinger equation is constructed from which the multiple scattering theory referred to as dynamical diffraction theory can be developed. The dynamical formulation used in our theoretical calculation is introduced in the last section. The effects of surface atomic thermal vibration (electron-phonon interaction) and inelastic damping which removes electrons from the flux of elastically scattered electrons in the scattering process, are also included in the theoretical calculation to improve the agreement of the calculated LEED intensities.

The theoretical calculation of surface scattering theory is reviewed in the second part of the next chapter. The surface-scattering of a symmetric slab waveguide calculated on the basis of radiation mode is first described and then a simple theory based on the Rayleigh criterion is introduced to calculate the surface scattering losses for an asymmetric slab waveguide. Since it is impossible to measure the scattering losses of the two asymmetric surfaces separately, all the surface properties were lumped into a single parameter in the theory. In integrated optics, however, rectangular strips of dielectric material embedded in other dielec-

tics are used. The theoretical formulation of surface-scattering losses for a rectangular waveguide is derived in the last section. An exact analytical treatment of this problem is impossible, therefore, an approximated analytical approach is used together with the simple theory in solving it.

The experimental methods are described in Chapter Three. The physical origin of Auger electron spectroscopy (AES) and the experimental set up for obtaining the Auger spectra are described. The technique used to characterize the surface geometry of the waveguide is introduced. The method used in forming a rib waveguide for investigating the surface-scattering losses of III-V compound semiconductor waveguides is suggested. Finally, all the electrical measurements with actual data handling are described.

In Chapter Four, the dynamical programs formulated in Chapter Two are applied to the GaP (110) surface for surface atomic structure determination. LEED intensities recorded experimentally with normal incident primary electron beams at both room temperature and low temperature were used in analyzing the surface structure. The atomic structure information such as layer spacing and atomic positions are quantitatively obtained through the analyses of the LEED patterns and the intensity profiles. The LEED patterns and experimental intensities for the GaP (111) face are analyzed, and the surface structure of GaP (110) face is compared with that of GaAs (110) face.

In Chapter Five, the physical mechanism for the metal-semiconductor interaction and forming of the Schottky barriers are discussed. As suggested in Chapter Four, the GaP (111) face was chosen to be the semiconductor surface for Schottky barriers studies. A macroscopic structural model of the real Schottky barrier is suggested. On the basis of the structural model, an electrical equivalent model is derived to address the fundamental behaviors of a real Schottky diode, including the origin of Fermi-level pinning, the barrier heights, and the deviation of the diode factor. Schottky barriers were fabricated on GaP (111) face to demonstrate the structural model. Electrical measurements described in Chapter Three were performed to analyze the electrical properties of the diodes. AES were used to correlate the chemical composition of the metal-semiconductor interface to the structure.

The surface-scattering losses of GaAs waveguide are investigated in Chapter Six. The simple theory of surface scattering introduced in Chapter Two, together with the effective index approximation, is used to calculate the surface-scattering losses of a rib waveguide. The experimental methods to prepare different degrees of surface "smoothness" of GaAs substrates are described. The results of quantitative characterization of the surface geometry of the substrates are reported. The surface geometric information combined with the signal losses measured after the substrate is fabricated into a rib waveguide will be used to develop the correlation between the surface "smoothness" and the surface scattering parameters.

Finally, the summary and conclusions of the thesis along with recommendations for future investigation are presented in Chapter Seven.

## CHAPTER 2

## TECHNICAL BACKGROUND

## 2.1 Review of Theoretical Formulation for Determination of the Atomic Structure of Solid Surface by Low Energy Electron Intensity Analysis

## 2.1.1 Introduction

It has been known for a very long time that low energy electron diffraction (LEED) is a powerful tool in the study of the atomic structure of solid surfaces. However, it is only since the achievement of ultrahigh vacuum (UHV) technology that LEED has been widely used and studied.

By measuring and analyzing coherent elastically backscattered electrons from a crystal surface, LEED can provide the geometric structure of a free-surface (solid-vacuum interface) of a solid, namely, the unit mesh symmetry, the unit mesh constants, the atomic position of the same or different kinds of atoms in the unit mesh, and furthermore, the spatial distance between the surface atomic layers, the shift distance of unit mesh relative to their substrates, and the relationship of the observed surface structure to the nature of chemical bonds of the substrate surface.

### 2.1.2 Notation for Surface Structure

Surfaces are usually named after the planes of bulk crystal to which they are parallel, e.g., (100), (110), etc. Their two-dimensional structure can be characterized in terms of a unit mesh, the smallest unit that can be repeated indefinitely to build up the whole surface. The two sides of the unit mesh will be designated by vectors  $\vec{a}$  and  $\vec{b}$  as shown in Fig. 2.1. The origin of any mesh can be given

$$l\vec{a} + m\vec{b} \text{ ----- (2.1)}$$

relative to the origin of a reference unit cell.  $l$  and  $m$  are integers. In the two-dimensional case, there are five kinds of Bravais lattice as shown in Fig. 2.2(a). The corresponding reciprocal lattices are shown in Fig. 2.2(b). The unit mesh vectors  $\vec{a}^*$  and  $\vec{b}^*$  of the reciprocal lattice are given by<sup>1</sup>

$$\vec{a}^* = 2\pi \begin{pmatrix} a_x & b_x \\ a_y & b_y \end{pmatrix}^{-1} \begin{pmatrix} b_y \\ -b_x \end{pmatrix} \text{ ----- (2.2)}$$

$$\vec{b}^* = 2\pi \begin{pmatrix} a_x & b_x \\ a_y & b_y \end{pmatrix}^{-1} \begin{pmatrix} -a_y \\ a_x \end{pmatrix} \text{ ----- (2.3)}$$

where  $a_x$  and  $b_x$  are the x components of  $\vec{a}$  and  $\vec{b}$ , respectively, and  $a_y$  and  $b_y$  are the y components of  $\vec{a}$  and  $\vec{b}$ , respectively.

If a reconstructed surface is to be described in terms of the bulk exposed plane or if a monolayer of some surface deposit has a different unit mesh from that of the solid surface upon which it is adsorbed, a simple notation devised by Wood<sup>2</sup> is used. Two examples of this notation are illustrated in Fig. 2.3. The unit meshes of the surface and bulk are related by an expression of the form  $(a_s/a_b \times b_s/b_b)R$ . The subscripts s and b are used for a surface mesh and for a bulk exposed plane, respectively. If the deposit mesh is not rotated with respect to the substrate (or bulk) mesh, then the rotation R is simply dropped from the notation. If the deposit mesh is a centered mesh, then a lower-case c will be used before the expression.

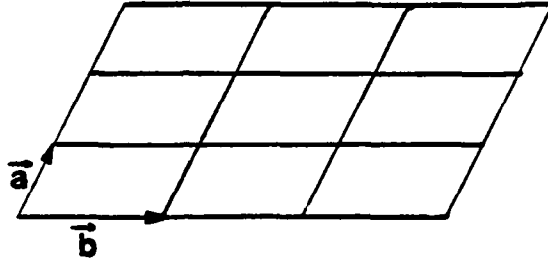


Fig. 2.1 Two-dimensional array of unit meshes.

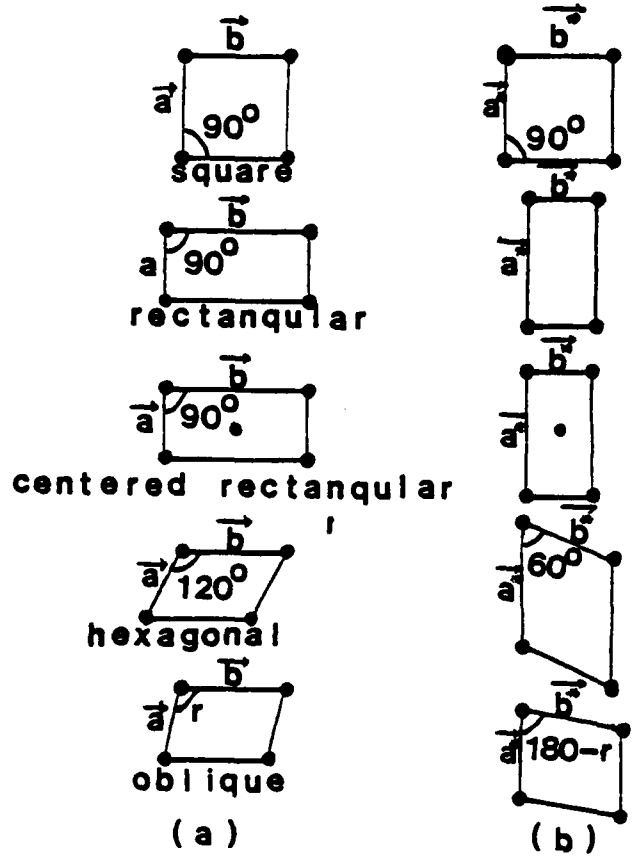


Fig. 2.2 (a) The five real two-dimensional unit meshes.  $\vec{a}$  and  $\vec{b}$  are unit mesh vectors. (b) The corresponding reciprocal two-dimensional unit meshes;  $\vec{a}^*$  and  $\vec{b}^*$  are unit mesh vectors in reciprocal space.

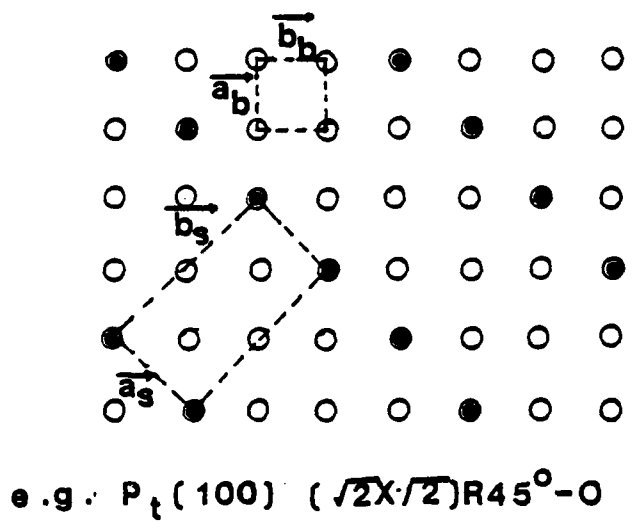
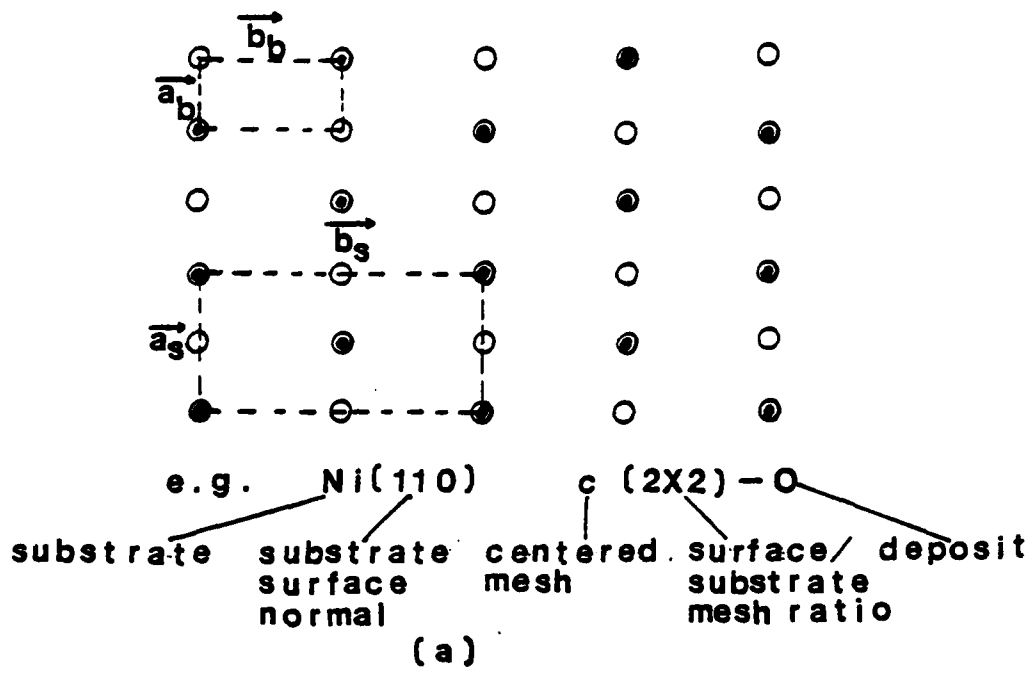


Fig. 2.3 Two examples of Wood's notation for surface structures; (a) Ni (110) face exposed to oxygen, (b)  $P_t$  (100) face exposed to oxygen.

### 2.1.3 The Diffraction Pattern

Assume a mono-energetic, collimated beam of electrons incident normally on a perfect two-dimensional lattice. Because of the periodicity along the direction of surface normal is lost in a two-dimensional case, the constructed interference of scattered waves cannot occur along this direction. This condition leads to the possibility of diffracted beam occurring at all incident energies and hence a diffraction pattern can be observed at all energies.

The unit mesh vectors  $\vec{a}^*$  and  $\vec{b}^*$  of the reciprocal lattice are related to the unit mesh vectors  $\vec{a}$  and  $\vec{b}$  of the real lattice via Eqs. (2.2) and (2.3). The energy  $E$  of the incident electron beams is given by

$$E = \hbar^2 k^2 / 2m \text{-----} (2.4)$$

$$\text{with } k = 2\pi/\lambda \text{ and } \hbar = h/(2\pi) \text{-----} (2.5)$$

where  $h$  is Planck's constant,  $m$  is the mass of electron and  $\lambda$  is the wavelength.

The Ewald sphere construction can then be applied to the two-dimensional diffraction problem as shown in Fig. 2.4. Because of the loss of periodicity in one dimension, the reciprocal-lattice rods can be labelled with two Miller indices  $h$  and  $k$ , and a general reciprocal lattice vector  $\vec{g}_{hk}$  lies in the plane of the surface and

is given by

$$\vec{g}_{hk} = h\vec{a}^* + k\vec{b}^* \text{-----} (2.6)$$

Because every point on the reciprocal-lattice rods is a reciprocal lattice point, diffraction occurs at the points where Ewald sphere cuts the reciprocal rods and the diffracted beam can be labelled with the Miller indices (hk) of the rod causing it. The wave vector of the diffracted beam can be characterized by

$$\vec{k}'_{hk} = \vec{k} + \vec{g}_{hk} \text{-----} (2.7)$$

Suppose the backscattered electrons are detected on a fluorescent screen. These points are visible on the screen as bright spots which constitute the electron diffraction pattern of the two-dimensional lattice. As shown in Fig. 2.4, the pattern provides us with a direct picture of the reciprocal lattice and an image of crystal periodicity. Hence, the diffraction pattern immediately reveals the unit mesh symmetry and dimension ratio.

As the energy of the incident electron changes, the magnitude of the radius of the Ewald sphere changes. So long as the radius is large enough to let the sphere intersect the reciprocal-lattice rods, the spots of the diffraction always exist with constant intensity.

In nature, the two-dimensional case does not exist because the incident electrons penetrate a distance of 8 to 12 Å<sup>0</sup> into the bulk of the crystal, they go sufficiently deep to be sensible of the periodicity along the direction of the surface normal. Constructed interference of scattered waves occurs in this direction. Further information about the deposition of contents of the cell, such as separation between planes of atoms or location of absorbers relative to the substrate, which cannot be provided by the diffraction pattern, is needed. This information is contained in intensities of the back-scattered beams measured as functions of incident energy or angle of incidence. Intensity/energy curves are the usual form for presenting data. The theoretical formulation of LEED intensity curves will be discussed in section 2.5.

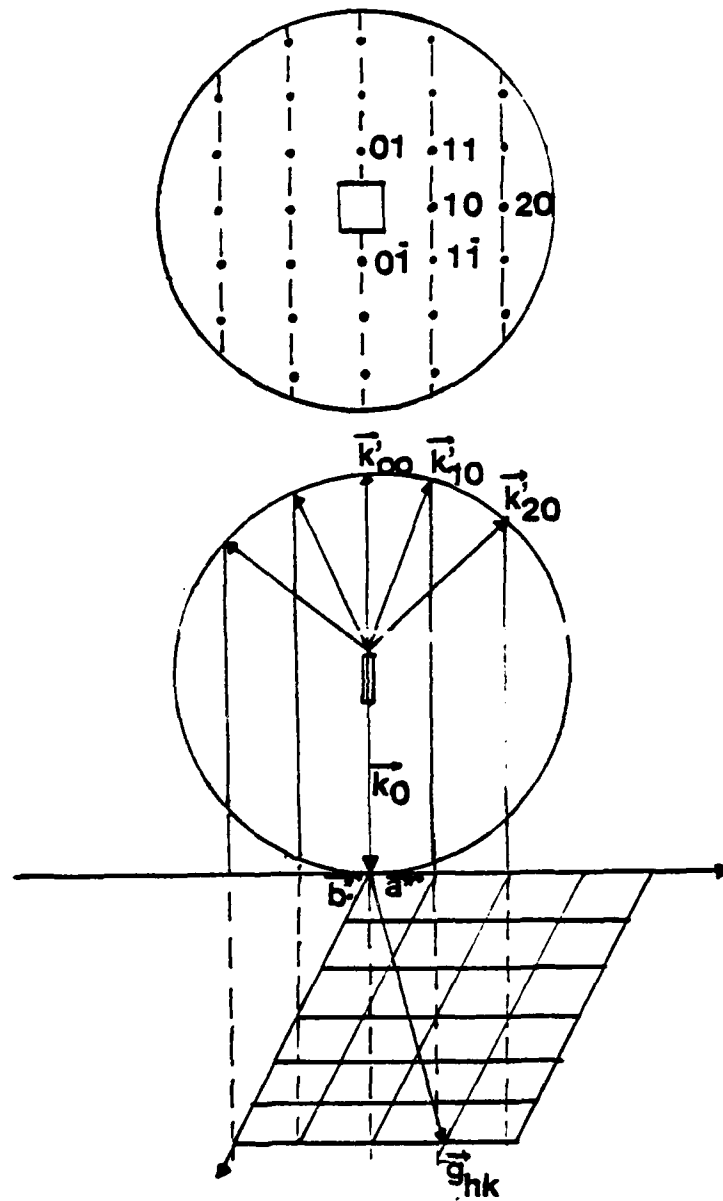


Fig. 2.4 Generation of LEED pattern from a two-dimension lattice, electron beam with wave vector  $\vec{k}_0$  is normally incident upon the crystal.

#### 2.1.4 Physical Model Used in LEED Intensity Calculation

The physical model of a crystal surface is assumed to be a defect-free, single crystal with an atomically flat, absorbent-free surface of at least several square millimeters in area. All theoretical formulations and analyses of surface structure in LEED are based on this assumption. Developments in LEED over the past several years have demonstrated that this highly idealized surface gives valuable guidance in the interpretation of experimental results.

The first step of LEED intensity calculation and analysis is to predict the peak positions in the intensity vs. energy curves of a certain spot in the diffraction pattern. Bragg Theory was combined with electron scattering theory to develop a formulation of LEED intensity some twenty years ago. This method is called the "kinematical model". The assumption of this formulation is that the incident electrons are scattered elastically once and only once from the atoms of the crystal. This kinematic computation of LEED intensity only gives some quantitative understanding of the crystal surface. It can only predict the positions of Bragg peaks. Actually, in an experimental intensity curve, there is much more structure than those predicted by the kinematic theory. "Secondary" peaks, "shoulders" and other peak shape anomalies in measured intensity curves can only be formulated by multiple scattering of the incident electrons from the crystal lattices. Multiple scattering events thus must be used in the formulation of LEED theory to obtain a good description of the intensity curve and to gain a quantitative

understanding of the crystal surface. The multiple scattering formulation is referred as the "dynamical model" of LEED theory.

There have already been abundant articles in the literature<sup>1,3,4</sup> reviewing the kinematic approach to the theory of LEED in detail, so it will not be discussed. The dynamical formulation constructed from a one-electron Schrodinger equation will be developed.

As the incident electrons approach the crystal, the most important interaction is the elastic scattering of the incident electron by ion-cores comprising the lattice. Let us consider a system consisting of a solid rigid lattice and a probing electron. We should be solving the complete Schrodinger equation that includes all electrons in the total wavefunction  $\phi$ .

$$\begin{aligned}
 H\phi = & \left( \sum_{j=0}^N (-\hbar^2/2m\nabla_j^2 - \sum_{\alpha} Z_{\alpha}/|\vec{R}_{\alpha}-\vec{r}_{\alpha}| + V_s(\vec{r}_j)) \right. \\
 & \left. + \sum_{j=0}^N \sum_{i=j+1}^N 1/|\vec{r}_i-\vec{r}_j| \right) \phi(\vec{r}_0, \vec{s}_0, \dots, \vec{r}_N, \vec{s}_N) = E_c \phi \quad (2.8)
 \end{aligned}$$

Here, the electrons, labelled by the index  $j$ , have positions  $\vec{r}_j$  and spin coordinates  $\vec{s}_j$ , the nuclei are labelled by  $\alpha$ , and have atomic number  $Z_{\alpha}$  and positions  $\vec{R}_{\alpha}$ , an incident electron has position  $\vec{r}_0$  and spin coordinate  $\vec{s}_0$ .  $E_c$  is the total energy which includes the core levels as well as that of the incident electron.  $V_s$  is the potential due to screening charge. By Pauli principle, the wavefunction  $\phi$  is antisymmetric under exchange of particles because electrons are Fermions. We can write down  $\phi$  as a product of core-state

wavefunctions.

$$\phi(\vec{r}_0, \vec{s}_0, \dots, \vec{r}_N, \vec{s}_N) = \sum_P (-1)^P \phi(\vec{r}_0, \vec{s}_0) \psi_1(\vec{r}_j, \vec{s}_j) \dots \psi_N(\vec{r}_k, \vec{s}_k) \quad (2.9)$$

$\phi$  is the wavefunction of incident electron. The sum is over permutations of electron coordinates. There are  $(N+1)!$  possible permutations. Since the core-state part of  $\phi$  is known already, it should be eliminated from Eq. (2.8) to simplify the problem.

Assume the individual wavefunctions are orthonormal

$$\left. \begin{aligned} \int_{\vec{s}} \int_{\vec{r}} \psi_j^*(\vec{r}, \vec{s}) \psi_j(\vec{r}, \vec{s}) d^3 \vec{r} &= \delta_{ij} \\ \int_{\vec{s}} \int_{\vec{r}} \psi_j^*(\vec{r}, \vec{s}) \phi(\vec{r}, \vec{s}) d^3 \vec{r} &= 0 \end{aligned} \right\} \quad (2.10)$$

and define a function

$$X(\vec{r}_1, \vec{s}_1, \dots, \vec{r}_N, \vec{s}_N) = \psi_1(\vec{r}_1, \vec{s}_1) \psi_2(\vec{r}_2, \vec{s}_2) \dots \psi_N(\vec{r}_N, \vec{s}_N) \quad (2.11)$$

Multiply Eq. (2.8) by  $X^*$ , and then integrate it over space and sum it over spin coordinates. The only term remaining on the right-hand side of the equation is that in which the coordinates have not been permuted, leaving just  $E_c \phi(\vec{r}_0, \vec{s}_0)$  after integration and summation. The left-hand side of the equation can be split into three parts

$$\begin{aligned}
& \sum_{S_{1..N}} d^3\vec{r}_1 \dots d^3\vec{r}_N X^* \left( \sum_{j=1}^N \left( -\hbar^2/2m\nabla_j^2 - \sum_{\alpha} Z_{\alpha}/|\vec{R}_{\alpha}-\vec{r}_j| + v_s(\vec{r}_j) \right) \right. \\
& + \sum_{j=1}^N \sum_{i=j+1}^N 1/|\vec{r}_j-\vec{r}_i| \left. \right) + \left( -\hbar^2/2m\nabla_0^2 - \sum_{\alpha} Z_{\alpha}/|\vec{R}_{\alpha}-\vec{r}_0| + v_s(\vec{r}_0) \right) \\
& + \left( \sum_{j=1}^N 1/|\vec{r}_0-\vec{r}_j| \right) \phi
\end{aligned}$$

The first term is zero unless the permutation in  $\phi$  are those leaving  $\phi = \phi(\vec{r}_0, \vec{s}_0)$ . From the first term of the above equation we obtain  $E_{ct} \phi(\vec{r}_0, \vec{s}_0)$ , where  $E_{ct}$  is the total energy associated with the core-states. The second term has non-zero value only if the coordinates of  $\phi$  have not been permuted, i.e.,

$$\left( -\hbar^2/2m \sum_{\alpha} Z_{\alpha}/|\vec{R}_{\alpha}-\vec{r}_0| + v_s(\vec{r}_0) \right) \phi(\vec{r}_0, \vec{s}_0)$$

Finally, the third term has non-zero contribution only from the first component of  $\phi$  and from those permutations that exchange coordinates of  $\phi(\vec{r}_0, \vec{s}_0)$

$$\begin{aligned}
& \sum_{j=1}^N \phi(\vec{r}_0, \vec{s}_0) \int \sum_{s_j} \Psi_j^*(\vec{r}_j, \vec{s}_j) \Psi_j(\vec{r}_j, \vec{s}_j) / |\vec{r}_0-\vec{r}_j| d^3\vec{r}_j - \\
& \sum_{j=1}^N \Psi_j(\vec{r}_0, \vec{s}_0) \int \sum_{s_j} \Psi_j^*(\vec{r}_j, \vec{s}_j) \phi(\vec{r}_j, \vec{s}_j) / |\vec{r}_0-\vec{r}_j| d^3\vec{r}_j
\end{aligned}$$

The complete equation is reduced to

$$\begin{aligned}
& (-\hbar^2/2m\nabla_0^2 - \sum_{\alpha} Z_{\alpha}/|\vec{R}_{\alpha} - \vec{r}_0| + V_s(\vec{r}_0) + \sum_{j=1}^N \int \sum_{s_j} |\Psi_j(\vec{r}_j, \vec{s}_j)|^2 / \\
& |\vec{r}_0 - \vec{r}_j| d^3\vec{r}_j) \phi(\vec{r}_0, \vec{s}_0) - \sum_{j=1}^N \int \sum_{s_j} \Psi_j^*(\vec{r}_j, \vec{s}_j) \phi(\vec{r}_0, \vec{s}_0) / |\vec{r}_0 - \vec{r}_j| d^3\vec{r}_j \\
\Psi_j(\vec{r}_j, \vec{s}_j) &= (E_t - E_{ct}) \phi(\vec{r}_0, \vec{s}_0) = E\phi(\vec{r}_0, \vec{s}_0) \text{-----} (2.12)
\end{aligned}$$

The strong resemblance of Eq. (2.12) to a simple one-particle Schrodinger equation enables us to connect the usual one-particle theories of diffraction with many-body problems. In essence, the usual theories of diffraction are based on this equation. The second term in Eq. (2.12) arises because of antisymmetry under exchanges of electrons, for no two electrons can appear at the same place at the same time.

Besides the electron ion-core interaction there are other contributions during the scattering of the electron from the crystal. They are from the conduction or valence electrons, and at finite temperatures from phonons as well. Electron and electron interactions are strong in the energy range of interest (10ev and 300ev). They excite surface and bulk plasmons and are responsible for energy losses during inelastic scattering. A complete detailed microscopic formulation and analysis of this interaction is beyond the existing capacity of physical theory. The modification is generally done by adding an empirical complex "optical" potential  $V_o$  in the Schrodinger equation (2.12) for inelastic scattering.

$$V_o = V_{or} + iV_{oi} \text{-----} (2.13)$$

The real part,  $V_{or}$ , of the optical potential (also known as the inner potential) is contributed by the exchange interaction of incident electron with the conduction or valence electrons of the crystal. The imaginary part,  $V_{oi}$ , of the optical potential is contributed by the inelastic collision. Both  $V_{or}$  and  $V_{oi}$  are treated as adjustable parameters whose values are selected during a calculation to achieve the best agreement with experimental intensity profiles. When the temperature of a crystal is raised, two changes become apparent in the diffraction pattern: firstly, intensities of individual diffraction spots decrease and secondly, the intensities of the background collected between spots grow stronger. It is the thermally induced vibration of atoms that are responsible for these phenomena. The theoretical treatment of the temperature effect in LEED formation will be discussed in the next section.

Several methods<sup>3-10</sup> have been proposed for solving Schrodinger equation of multiple scattering. One of the methods<sup>6-10</sup> mostly used in LEED, is to formulate the dynamic theory from the multiple scattering point of view. The basic viewpoint of multiple scattering theory is that the interaction between the incident electron beam and scattering centers is visualized in terms of a succession of scattering effects. Based on this viewpoint one can express the entire complex scattering problem in terms of the individual scatterers. A multiple scattered electron from the crystal ion-core potential can be viewed as composed of sum over paths of an electron undergoing individual scattering events from each separated ion-core potential. The whole crystal is assumed to be constructed of the largest non-overlapping spheres of each atom. The potential inside the sphere will be spherically symmetric, and the potential outside will be constant. This is called the "muffin tin model" of the crystal potential. The radius of the potential sphere is called the muffin-tin radius of the specific atomic species. The incident electrons are assumed to be scattered elastically by the individual potential sphere only and propagating freely in the spaces between the spheres. Under these assumptions, the individual scattering of electron from the sphere can be characterized by a phase shift of scattered wave relative to the incident wave. To implement this procedure the incoming plane wave is expanded in spherical harmonic partial wave components. The computation of  $l$ 'th partial wave's phase shift  $\delta_l$  ( $l=0,1,2,\dots$ ) can be found in standard text of quantum

mechanics<sup>11</sup>. Computer programs for calculation  $\delta_\lambda$  are available in the literature<sup>1</sup>. Thus, the details of  $\delta_\lambda$  computation will not be discussed. There are many equivalent mathematical formulism for solving the multiple scattering equations, and there are correspondingly many computer programs to implement these various schemes. The computer programs used in our dynamical LEED intensity calculation were supplied by Tong, et al. and the formulism they used for solving the multiple scattering is known as the layer method<sup>1</sup>, in which the bulk crystal and adsorbate system is replaced by a finite slab made by layers of atoms parallel to the surface of the crystal. Multiple scattering is calculated first among the atoms of a single layer, and subsequently among the stack of layers which form the complete crystal. The method will be described as follows:

Assume an electron beam is incident on the crystal. The surface model of the crystal is defined in terms of a right-hand coordinate axes, two of which (x,y) lie in the plane of the layer, parallel to the surface with the third (z) pointing into the crystal and defining the positive direction for wave propagation. Each layer of a stack consists of a periodic array of atoms represented for scattering purposes by spherically non-overlapping muffin-tin potentials. The scattering properties of each atomic potential are described by a set of phase shifts, and the constant potential outside the muffin-tin spheres is taken as the zero level for the calculation. In general, the position vector of an atom within a layer is written as

$$\vec{r}_p^\alpha = \vec{r}_p + \vec{s}_\alpha \text{ ----- (2.14)}$$

$\vec{r}_p^\alpha$  is the location of the  $\alpha$ 'th atom in  $p$ 'th unit cell.

$$\vec{r}_p = l\vec{a} + m\vec{b} \text{ -----(2.15)}$$

where  $l$  and  $m$  are integers, and  $\vec{a}$  and  $\vec{b}$  are the unit mesh vectors within the layer. Eq. (2.15) restricts the number of atoms in the unit cell to one ( $\alpha=A$ ) or two ( $\alpha=A,B$ ). The displacement vector  $\vec{s}_B$  from A-atom to B-atom, may have a non-zero perpendicular component, giving a non-coplanar or "ruffled" layer. The incident electron beam is given in terms of its energy  $E$  in the vacuum, and the two direction angles, e.g., the polar angle  $\theta$  measured with respect to the surface normal ( $+z$ ), and the azimuthal angle  $\phi$  measured with respect to the direction chosen as ( $+x$ ) in the plane of the surface. The components of momentum of the incident beam parallel to the surface are given by

$$k_x = k \sin \theta \cos \phi, \quad k_y = k \sin \theta \sin \phi \text{ -----(2.16)}$$

$$\text{with } k = |\vec{k}| = (2mE/\hbar^2)^{1/2} \text{ -----(2.17)}$$

If a plane wave

$$\phi^+ = A \exp(i\vec{k}^+ \cdot \vec{r}) \text{ -----(2.18)}$$

is incident on the crystal, the 2-d periodicity means that reflected waves must be comprised of a set of discrete beams

$$\phi^- = \sum_{\vec{g}} b_{\vec{g}}^- \exp(i \vec{k}_{\vec{g}} \cdot \vec{r}) \quad (2.19)$$

$$\vec{k}_{\vec{g}}^{\pm} = ((k_x + g_x), (k_y + g_y), -(2mE/h^2 - 2V_0 - (k_x + g_x)^2 - (k_y + g_y)^2)^{1/2}) \quad (2.20)$$

where  $\vec{g}$  is a reciprocal vector of 2-d mesh,  $V_0$  is the optical potential of the crystal, and  $E$  is the energy of the incident plane wave. We choose the  $+z$  direction to be pointing inward into the crystal surface.

Consider a set of plane waves

$$\phi^{\pm} = \sum_{\vec{g}} a_{\vec{g}}^{\pm} \exp(i \vec{k}_{\vec{g}}^{\pm} \cdot \vec{r}) \quad (2.21)$$

incident from the  $+z$  and  $-z$  directions on a layer. It is more convenient to re-express the plane waves as a sum of spherical partial waves. The spherical wave expansion of Eq. (2.21) about the  $\alpha$ 'th atom in the  $p$ 'th unit cell becomes

$$\begin{aligned} \phi^{\pm} &= \sum_{\vec{g}} a_{\vec{g}}^{\pm} \exp(i \vec{k}_{\vec{g}}^{\pm} \cdot (\vec{r} - \vec{r}_p^{\alpha})) \exp(i \vec{k}_{\vec{g}}^{\pm} \cdot \vec{r}_p^{\alpha}) \\ &= \sum_{\ell m} A_{\ell m \alpha}^{(\pm)} j_{\ell}(k |\vec{r} - \vec{r}_p^{\alpha}|) Y_{\ell m}(\Omega(\vec{r} - \vec{r}_p^{\alpha})) \exp(i \vec{k}_{\vec{g}}^{\pm} \cdot \vec{r}_p^{\alpha}) \quad (2.22) \end{aligned}$$

with

$$A_{\ell m \alpha}^{(\pm)} = \sum_{\vec{g}} a_{\vec{g}}^{\pm} 4\pi i^{\ell} (-1)^m Y_{\ell -m}(\Omega(\vec{k}_{\vec{g}}^{\pm})) \exp(i \vec{k}_{\vec{g}}^{\pm} \cdot \vec{s}_{\alpha}^{\pm}) \quad (2.23)$$

where  $A_{\ell m \alpha}^{(0)}$  is the amplitude of  $(\ell, m)$  angular momentum component of the incident wave at the  $\alpha$ 'th ion-core in the unit mesh, and

$$k = \left| \frac{\vec{k}}{g} \right| = (2mE/\hbar^2 - 2V_0)^{1/2} \text{-----} (2.24)$$

$\Omega(\vec{r}-\vec{r}_p^{\alpha})$  stands for the angular coordinates of  $\vec{r}-\vec{r}_p^{\alpha}$ .  $j_\ell$  is spherical Bessel function.  $Y_{\ell m}$  is the spherical harmonics function of angular variation of the wavefunction, and  $\ell$  and  $m$  are angular quantum numbers.

For multiple scattering, the total amplitude of the waves incident on the  $\alpha$ 'th ion-core in the unit cell,  $A_{\ell m \alpha}$ , will include a further contribution  $A_{\ell m \alpha}^{(s)}$ , representing the amplitude scattered from other ion-cores, which depends on  $A_{\ell m \alpha}$ . Therefore, these quantities must be determined by self consistent iteration<sup>1</sup>.

$$A_{\ell m \alpha} = A_{\ell m \alpha}^{(0)} + A_{\ell m \alpha}^{(s)} \text{-----} (2.25)$$

$$\text{with } A_{\ell m \alpha}^{(s)} = \sum_{\ell' m' \beta} A_{\ell' m' \beta} X_{\ell' m' \beta, \ell m \alpha} \text{-----} (2.26)$$

where  $X_{\ell' m' \beta, \ell m \alpha}$  is the multiple scattering matrix connecting the  $\alpha$ 'th and  $\beta$ 'th unit meshes, combining Eqs. (2.25) and (2.26) gives

$$A_{\ell m \alpha} = \sum_{\ell' m' \beta} A_{\ell' m' \beta} (I - X)^{-1} \ell' m' \beta, \ell m \alpha \text{---} (2.27)$$

which is the amplitude of the scattered beam.

$$\vec{b}_{\vec{g}}^{\pm} = \sum_{\vec{g}'} M_{\vec{g}\vec{g}'}^{\pm} \vec{a}_{\vec{g}'}^{\pm} \quad \text{-----} (2.28)$$

where  $M_{\vec{g}\vec{g}'}^{\pm}$  are the scattering matrices of the layer. The sign convention is such that  $M_{\vec{g}\vec{g}'}^{-}$  describes scattering of a beam  $\vec{g}$  incident in positive (+) direction, to beam  $\vec{g}'$  reflected back in the negative (-) direction.

$$M_{\vec{g}\vec{g}'}^{\pm} = \ell^{-\sum_{\beta, \ell m \alpha} \beta, \ell m \alpha} 8\pi^2 i/kA |\vec{k}_{\vec{g}}^{\pm}| \left( i^{\ell} (-1)^m Y_{\ell}^{-m}(\Omega(\vec{k}_{\vec{g}}^{\pm})) \right) \\ \exp(i\vec{k}_{\vec{g}}^{\pm} \cdot \vec{s}_{\beta}) \left( (I-X)^{-1} \right)_{\ell}^{-\beta, \ell m \alpha} \left( i^{-\ell} Y_{\ell m}(\Omega(\vec{k}_{\vec{g}}^{\pm})) \right) \\ \exp(-i\vec{k}_{\vec{g}'}^{\pm} \cdot \vec{s}_{\alpha}) \exp(i\delta_{\ell}^{\alpha}) \sin\delta_{\ell}^{\alpha} \quad \text{-----} (2.29)$$

where  $A$  is the area of the unit cell, and  $\delta_{\ell}^{\alpha}$  is the  $\ell$ th wave phase shift of the atom in subset  $\alpha$ .

This completed the formulation of multiple scattering within a single layer. The multiple scattering subsequently among the stack of layers will be examined in the next section.

The division of the crystal into layers is illustrated in Fig. 2.5, which shows a cross-section normal to the surface through the atom cores in successive layers. The layers are labelled  $i=0, 1, 2, \dots$  from the vacuum into the crystal,  $i=1$  denotes the surface layer and  $i=0$  denotes the position of the surface potential barrier, layer displacement  $d_i$  are measured into the crystal (+z-direction) and

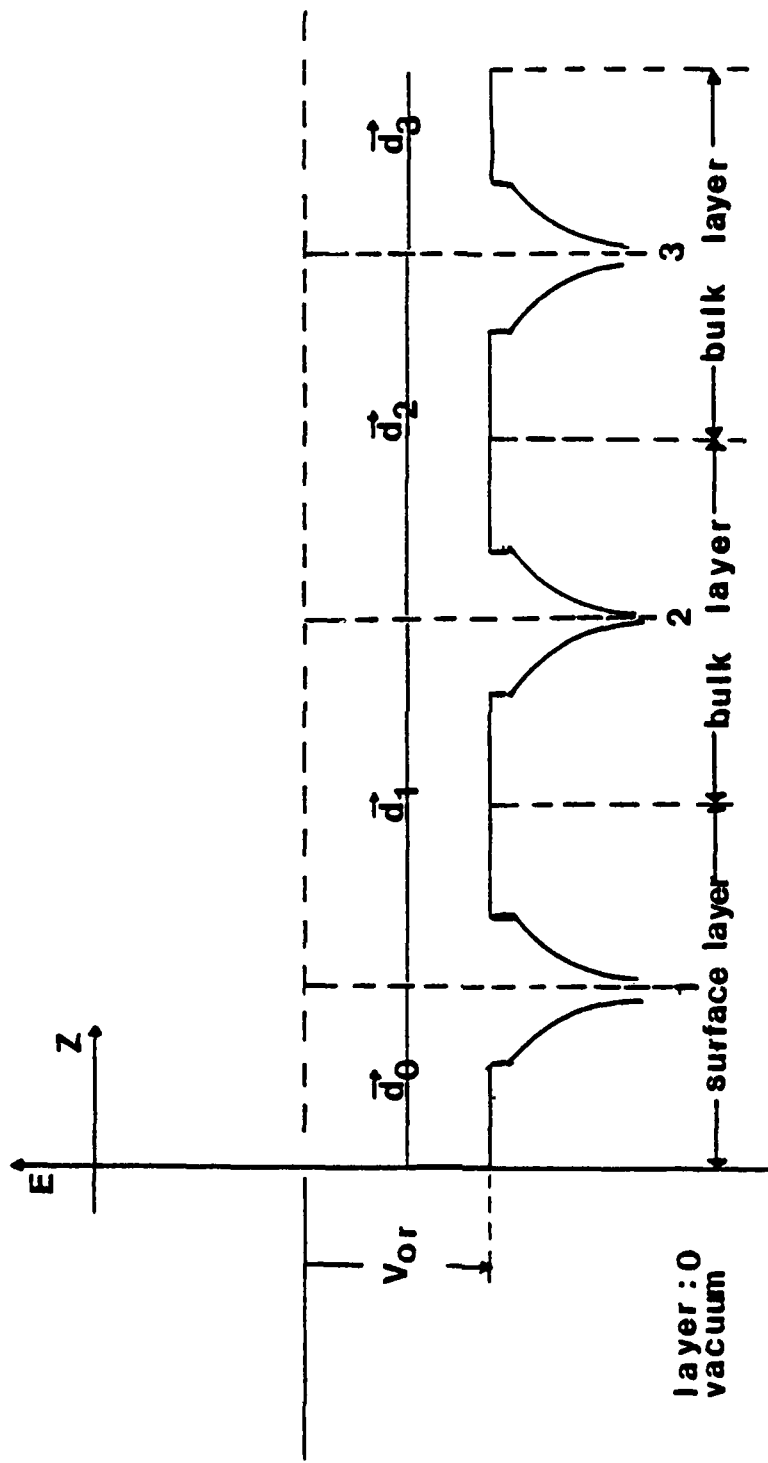


Fig. 2.5 Cross section normal to the surface, showing the potential inside the crystal and the arrangement of the layers.

measured from an A-atom site in the  $i$ 'th layer to an A-atom site in  $i+1$ 'th layer. The displacement of the surface potential barrier from the first layer of atom  $d_0$  defines the physical position of the surface. It is an adjustable parameter. The layers are separated by constant potential regions and in these regions the wavefield can be represented by a superposition of plane waves, e.g.,

$$\phi_i(\vec{r}) = \sum_{\vec{g}} a_{\vec{g}}^+ \exp(i\vec{k}_{\vec{g}}^+ \cdot \vec{r}) + a_{\vec{g}}^- \exp(i\vec{k}_{\vec{g}}^- \cdot \vec{r}) \quad \text{----(2.30)}$$

where  $\vec{r}$  is referred to a point halfway between layers. Scattering of such a wavefield through the  $i$ 'th layer is governed by the equation,

$$\begin{aligned} A_i^+ &= P_i^+ T_i^{++} P_{i-1}^+ A_{i-1}^+ + P_i^+ R_i^{+-} P_{i-1}^- A_{i-1}^- \\ A_{i-1}^- &= P_{i-1}^- R_i^{-+} P_i^+ A_i^+ + P_{i-1}^- T_i^{--} P_i^- A_i^- \end{aligned} \quad \text{-----(2.31)}$$

where a vector notation for the beam amplitudes has been used, e.g.,

$$A_i^\pm = (a_{\vec{g}}^\pm).$$

The matrices

$$\begin{aligned} T_i^{++} &= I + M_i^{++} & , & \quad T_i^{--} = I + M_i^{--} \\ R_i^{+-} &= M_i^{+-} & , & \quad R_i^{-+} = M_i^{-+} \end{aligned} \quad \text{-----(2.32)}$$

are the reflection and transmission matrices, respectively, for the  $i$ 'th layer referred to an origin in the layer, and the matrices

$$P_i^\pm = \exp(\pm i \vec{k}_i^\pm d_i/2) \delta_{\vec{g}, \vec{g}'} \quad \text{-----} (2.33)$$

represent the propagation factors which account for phase change and attenuation of  $\phi_i(\vec{r})$  between the interlayer origin.

Assume that scatterings are predominantly in the forward direction, and that the absorption process is strong enough to attenuate the wave amplitude significantly within a few layers from the surface, then the renormalized forward scattering (RFS) perturbation theory<sup>1</sup> can be used. The amplitude vectors  $A_i$  can be expressed in a series of perturbative terms of order  $n$ ,

$$A_i^+ = \sum_n A_i^{+(n)} \quad \text{and} \quad A_{i-1}^- = \sum_n A_{i-1}^{-(n)} \quad \text{-----} (2.34)$$

A set of recurrence relation for the wave amplitudes between layers can be obtained from Eq. (2.31)

$$A_i^{+(n)} = P_i^+ T_i^{++} P_{i-1}^+ A_{i-1}^{+(n)} + P_i^+ R_i^{+-} P_i^- A_i^{-(n-1)} \quad \text{----} (2.35)$$

$$A_{i-1}^{-(n)} = P_{i-1}^- R_{i-1}^{-+} P_{i-1}^+ A_{i-1}^{+(n)} + P_{i-1}^- T_{i-1}^{--} P_i^- A_i^{-(n)}$$

where  $A_i^{-(0)} = 0$  by definition, and  $A_0^{+(1)}$  represents the incident beam inside the surface barrier. If the series expansions of these equations are convergent at some layer  $j$  for each order  $(n)$ ,

$A_{j+1}^{-(n)}$  is 0 and then the exact solutions of the transfer equation (2.31) can be obtained. The final backscattered wave outside the surface layer is given by

$$A_0^- = \sum_n \bar{A}_0^{-(n)} \text{ ----- (2.36)}$$

The inner most layer of each pass,  $j$ , is chosen by the following criterion of attenuation of the wavefield

$$\left( \sum_g (a_{jg}^{+(n)})^2 \alpha_n \right) < 0.001 \text{ ----- (2.37)}$$

where  $\alpha_n$  is a normalization factor for successive passes

$$\alpha_n = \left( \sum_g (a_{jg}^{+(1)})^2 \right)^{n-1/2} \text{ ----- (2.38)}$$

Convergence over successive passes is governed by the same parameter, the process stops at  $N$  when

$$\sum_g (a_{og}^{-(n)})^2 / \sum_{n=1}^N \left( \sum_g (a_{og}^{-(n)})^2 \right) < 0.001 \text{ ----- (2.39)}$$

This scheme of calculation is fast and efficient, but may break down at low energies where absorption is small and back scattering of the wavefield is significant. The RFS method is generally successful for well-separated layers with energies greater than 10eV above the muffin-tin zero level.

Effect of thermal vibration was not considered in the above formulation. The thermal motion of the atom excites lattice waves and distorts the regular arrangement of the atoms, and consequently reduces the intensities of the beams. The intensities of the beams change in the variation with the energy and the angle of the incident beam. It is therefore an important ingredient in a diffraction calculation for crystals with Debye temperature considerably lower than room temperature. Including this effect in a dynamical theory as required in LEED is very difficult and is presently done by crude methods. Since the atoms of the crystal change their positions by an extremely small amount during the time in which an electron moves into the crystal and out again, it is convenient to use the approximation that the lattice motion is actually static during the interaction. We need only consider the scattering of an electron by a crystal in which each atom is displaced from its site by a small random vector determined by the equilibrium phonon distribution. We assume that the electrons are scattered in the interiors of the atoms rather than in relatively smooth potential towards the outside and between them. It is then possible to calculate the scattering matrix  $t$  of an atom on its lattice site and use the result to describe the scattering of the atom displaced off the site by using the same matrix  $t$  in a shift set of coordinates. A method introduced by Duke and Laramore<sup>11</sup>, presently used in most LEED calculations, is to replace each vibrating atom of the crystal by a "blurred atom". The "blurred atom" has a scattering matrix which consists of the scattering matrix of the atom averaged over the displacements it undergoes in the vibration motion of the lattice. The resulting lattice

of the blurred atoms has the full symmetry of the rigid lattice so that the multiple scattering can be applied immediately.

If the scattering matrix in momentum space of a typical atom is denoted by  $t_{\vec{k}'\vec{k}}$ , then the scattering of this atom displaced by the vector  $\Delta p$  is given by

$$\tilde{t}_{\vec{k}'\vec{k}} = t_{\vec{k}'\vec{k}} \exp(i(\vec{k}' - \vec{k}) \cdot \Delta p) \text{ ----- (2.40)}$$

and the scattering matrix of the corresponding blurred atom is given by the thermal average of the scattering matrix, e.g.,

$$\langle \tilde{t}_{\vec{k}'\vec{k}} \rangle_{av} = t_{\vec{k}'\vec{k}} \langle \exp(i(\vec{k}' - \vec{k}) \cdot \Delta p) \rangle_{av} \text{ ---- (2.41)}$$

The average occurring here is a typical Debye-Waller factor and can be evaluated to give

$$\langle \tilde{t}_{\vec{k}'\vec{k}} \rangle_{av} = t_{\vec{k}'\vec{k}} \exp \langle i(\vec{k}' - \vec{k}) \cdot \Delta p \rangle_{av} \text{ ---- (2.42)}$$

If the atom is spherically asymmetric and isotropic, these relations can be used to define a temperature dependent "phase shifts"  $\delta_\lambda(T)$  at temperature  $T$  for a blurred atom in terms of the phase shift of  $\delta_\lambda$  of the fixed atom by<sup>13</sup>

$$\exp(i\delta_\lambda(T) \sin(\delta_\lambda(T))) = \sum_{L, \lambda''} \frac{1}{\lambda''} \exp(-2\alpha k^2)^j (-2i\alpha k^2) \exp(i\delta_\lambda) x$$

$$\sin(\delta_\lambda) \frac{4\pi(2L+1)(2\lambda''+1)}{(2\lambda+1)} B^{\lambda''} (L_0, \lambda_0) \text{ ---- (2.43)}$$

with  $k^2 = 2mE/\hbar^2 - 2V_0$

The quantity  $\alpha$  is given by

$$\alpha = 3\hbar^2 T / 2mk_B \Theta_D \quad \text{-----} \quad (2.44)$$

where  $m$  is the mass of the atom,  $k_B$  is the Boltzmann constant, and  $\Theta_D$  is the Debye temperature.

The temperature corrections can be incorporated into the LEED calculation by substituting  $\delta_\ell$  by  $\delta_\ell(T)$  in Eq. (2.29). Complete theoretical treatment of temperature effect in LEED intensity calculation can be found in the literatures<sup>1,12,14,15</sup>.

The computer block programs used for our dynamical formulation of LEED intensity calculation are shown in Fig. 2.6. The details of the computer input and output will be discussed in Chapter Four.

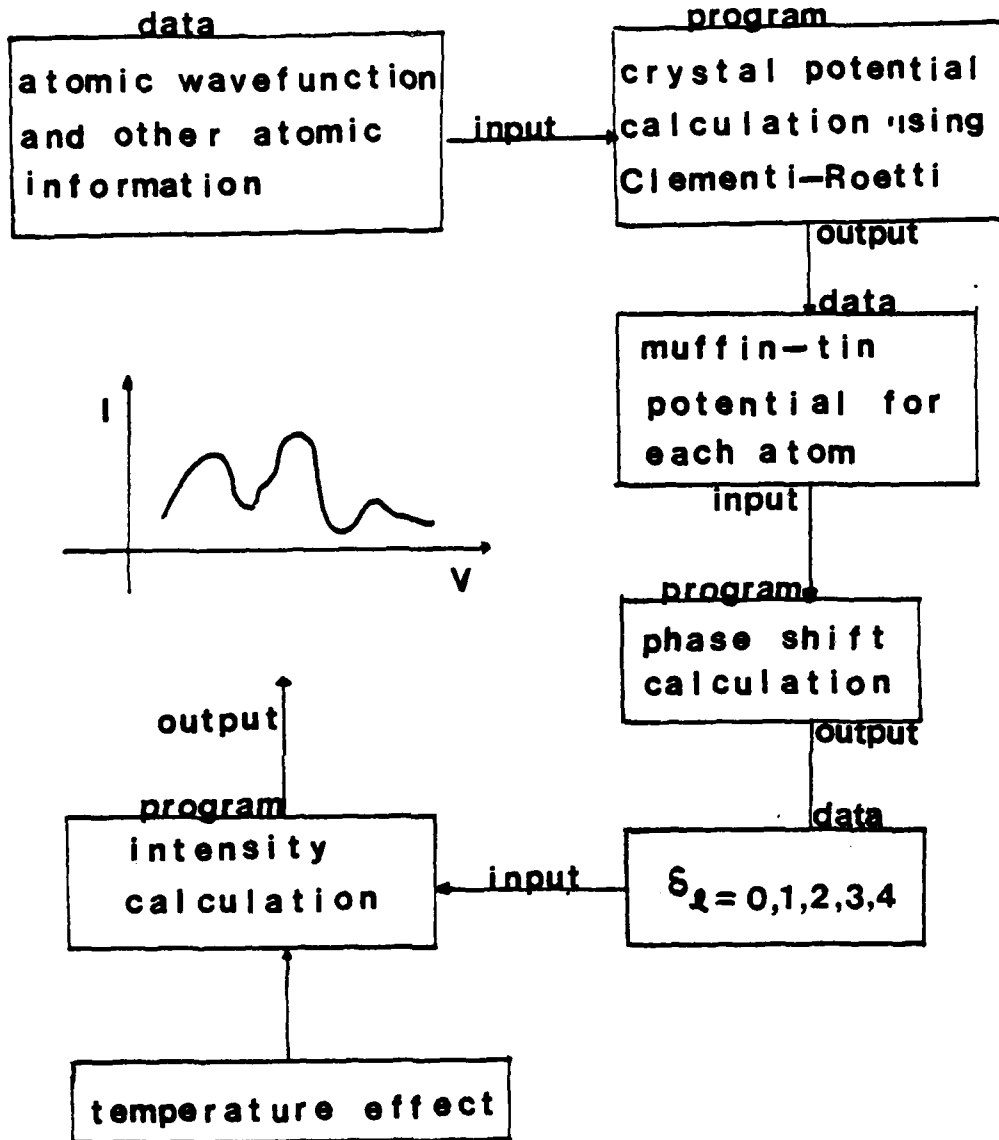


Fig. 2.6 Block diagram of a dynamic computer program.

## 2.2 Theoretical Calculation of Surface Scattering Theory

### 2.2.1 Introduction

When an electromagnetic wave is incident on a perfect plane interface between two media, the reflected wave is a function of its wavelength, the angle of incident and the electrical properties (permittivity, permeability and conductivity) of the two adjoining media.

The general and exact solution of a wave reflected from an irregular boundary, the random or periodic variation with respect to height measured from a certain mean plane is yet unknown. To find the approximate solutions of such a reflected wave have aroused to the interest of physicists and engineers for the past 70 years.

The foremost barrier in integrated optics is that the optical propagation losses of the III-V compound semiconductors cannot be reduced to an acceptable level. One of the most important sources of loss of a wave propagating along a thin-film waveguide is the surface scattering effect from the rough surface of the waveguide (or any other structure). In order to evaluate the performance of a realistic waveguide, it is necessary to study its behavior if departures from the perfect geometry occur.

### 2.2.2 Theoretical Calculation of Surface Scattering of a Symmetric Slab Waveguide

Theoretical calculation of the surface scattering of a symmetric slab waveguide has been reported by Marcuse<sup>16</sup> based on mode conversion to guided and radiation modes. The structure of a symmetric slab waveguide is simple, and could be used to study the radiation and conversion properties of dielectric waveguide.

Light propagation in waveguides occur in normal modes; the eigen-solutions of the wave equation are obtained by solving the boundary conditions of the waveguide. There are two types of normal modes: "waveguide" modes, in which the waves are bounded within the guiding material, and "radiation" modes, in which the waves are not bounded to a dielectric slab and persist undiminished through out all space. Together the "waveguide" and "radiation" modes form a complete set of eigensolutions and have nondegenerate eigenvalues, and are, therefore, mutually orthogonal. The eigenvalues of the "waveguide" modes are discrete, whereas those of the "radiation" modes are continuous.

The ideal slab waveguide is sketched in Fig. 2.7 (a). It resembles a longitudinal cross-section through the claded optical fiber. We simplify the discussion further by assuming there is no variation of either the waveguide geometry or the field distributions in  $y$  direction. We express this limitation on guide symmetry by the relation

$$\partial/\partial y = 0 \text{ -----(2.45)}$$

This restriction, Eq. (2.45), allows us to decompose the field of the slab waveguide into the transverse electric (TE) modes and transverse magnetic (TM) modes. We begin with the derivation of the properties of the TE modes. By definition, the electric field in the z direction,  $E_z$ , is equal to zero. Using Eq. (2.45) and Maxwell's equations we see that only the magnetic field in the x and z directions,  $H_x$  and  $H_z$ , respectively, and the electric field in the y direction  $E_y$  are non-zero. We can express  $H_x$  and  $H_z$  in terms of  $E_y$ ,

$$H_x = -(1/w\mu)(\partial E_y/\partial z) \text{ -----(2.46)}$$

$$\text{and } H_z = (1/w\mu)(\partial E_y/\partial x) \text{ -----(2.47)}$$

where  $w$  is the frequency and  $\mu$  is known as the magnetic permeability. The  $E_y$ -component is obtained as a solution of the reduced wave equation:

$$(\partial^2 E_y/\partial x^2) + (\partial^2 E_y/\partial y^2) + n^2 k_0^2 E_y = 0 \text{ ---(2.48)}$$

$$\text{with } n^2 = \epsilon/\epsilon_0 \text{ -----(2.49)}$$

$$\text{and } k = w\sqrt{\epsilon_0\mu_0} = 2\pi/\lambda_0 \text{ -----(2.50)}$$

where  $n$  is index of refraction,  $\epsilon$  is the dielectric permittivity,  $\epsilon_0$  and  $\mu_0$  are the permittivity and magnetic permeability in free space, respectively, and  $\lambda_0$  is the wavelength in vacuum. Including the time and z-axis dependent,

$$\exp(i(\omega t - \beta z)) \text{ ----- (2.51)}$$

and using Eqs. (2.48) and (2.51), we obtain the following equation,

$$(\partial^2 E_y / \partial x^2) + (n^2 k_0^2 - \beta^2) E_y = 0 \text{ ----- (2.52)}$$

The propagation constant  $\beta$  denotes the eigenvalue of the normal modes.

According to the orthogonality relation<sup>17</sup>, any arbitrary field distribution can be expressed in terms of the orthogonal modes of the slab waveguide. It is then possible to write

$$E_y = \sum C_U E_{Uy} + \int q(\rho) E_y(\rho) d\rho \text{ ----- (2.53)}$$

$$\text{with } C_U = (\beta / 2 \omega \mu_0 P) \int_{-\infty}^{\infty} E_y E_{Uy}^* dx$$

$$\text{and } q(\rho) = (\beta / 2 \omega \mu_0 P) \int_{-\infty}^{\infty} E_y E_y^*(\rho) dx \text{ ----- (2.54)}$$

The first term in Eq. (2.53) sums over all TE waveguide modes, while the second term is the combination of summation and integration which extends over all radiation modes. The power  $P$  was assumed to be the same for all the modes. The actual amount of power that each mode contributes to the field expansion is determined by the values of the expansion coefficients ( $C_U$  and  $q(\rho)$ ).

For the TE mode, the total power carried by the field is given by the expression.

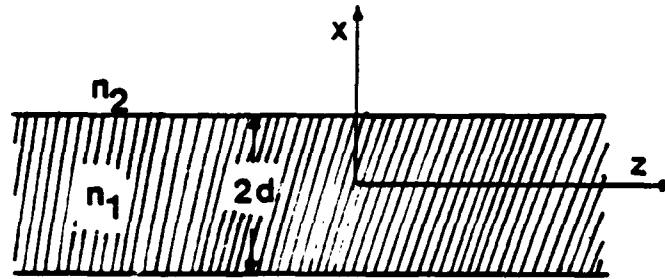
$$P_T = P(\sum |C_U|^2 + \sum \int_0^\infty |H(\rho)|^2 d\rho) \text{ -----(2.55)}$$

Our treatment of slab waveguide with imperfect walls is based upon finding solutions of the reduced wave equation (2.48) throughout all space by satisfying certain boundary conditions at infinity. It is also possible to express the field of an imperfect waveguide in terms of the modes of an ideal guide. We assume that the walls of the imperfect waveguide obey the restriction of Eq. (2.45). This limits the boundary imperfections to changes in slab thickness and does not allow variations in the y direction. The departures of the waveguide boundary have to be very small so that they can be treated by perturbation theory. A slab waveguide is shown in Fig. 2.7 (b). The distribution of the refractive index for waveguide with imperfect walls can be indicated as follows;

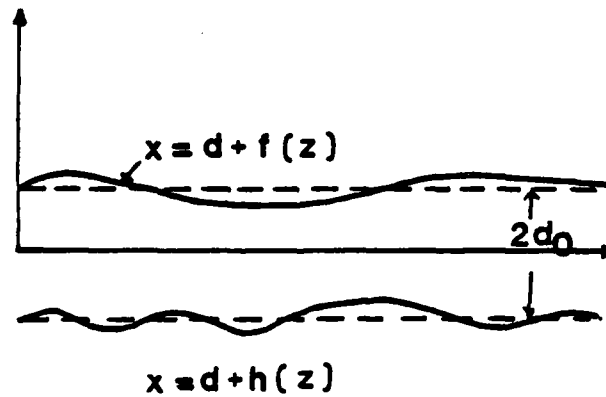
$$n^2(x,z) = n_0^2(x,z) + \eta(x,z) \text{ -----(2.56)}$$

where  $n_0$  describes the distribution of the refractive indices for the perfect slab waveguide.

$$n_0(x,z) = \begin{cases} n_2 & \text{for } x > d \\ n_1 & \text{for } x < d \end{cases} \text{ -----(2.57)}$$



(a)



(b)

Fig. 2.7 Cross section view of a slab waveguide (a) with perfect boundary, (b) with imperfect boundary.

The values of  $\eta$  are given by the following equation.

$$\eta = \begin{cases} 0 & \text{for } d+f(z) < x \\ n_1^2 & - n_2^2 & \text{for } d < x < d + f(z) \\ 0 & \text{for } -d + h(z) < x < d \\ n_2^2 & - n_1^2 & \text{for } -d < x < -d + h(z) \\ 0 & \text{for } x < -d \end{cases} \quad (2.58)$$

Where  $f(z)$  and  $h(z)$  are wall distortion functions. The difference  $n_1^2 - n_2^2$  may not necessarily be small for perturbation theory to be applicable. It is sufficient that the region over which  $\eta$  is non-zero is narrow.

We substitute Eqs. (2.53) and (2.56) into Eq. (2.48) and obtain

$$\sum_y \left( \frac{\partial^2 C_y}{\partial z^2} - 2i\beta_y \frac{\partial C_y}{\partial z} + C_y k_0^2 \eta \right) E_{uy} + \sum_y \int \left( \frac{\partial^2 q(\rho)}{\partial z^2} - 2i\beta \frac{\partial q(\rho)}{\partial z} + q(\rho) k_0^2 \eta \right) E_y(\rho) d\rho = 0 \quad (2.59)$$

by using the fact that the modes  $E_{uy}$  and  $E_y(\rho)$  satisfy the wave equation for the ideal slab waveguide.

We multiply Eq. (2.59) by  $\beta_u E_{uy} / 2w_{u0}$  ( $u$  is an integer) and integrate over the entire cross-section of the guide. Using the orthogonality relation, we obtain

$$\left( \frac{\partial^2 C_u}{\partial z^2} - 2i\beta_u \frac{\partial C_u}{\partial z} + \sum_y C_y F_{uy}(z) \right)$$

$$+\sum_0^{\infty} q(\rho) G_u(\rho, z) d\rho = 0 \text{ -----(2.60)}$$

$$\text{where } F_{Uu}(z) = (\beta_u k_0^2 / 2w_{u0} P) \int_{-\infty}^{\infty} E_{uy}^* \eta(x, z) dx \text{ ---(2.61)}$$

$$\text{and } G_u(\rho) = (\beta_u k_0^2 / 2w_{u0} P) \int_{-\infty}^{\infty} E_{uy}^* \eta(x, z) E_y(\rho) dx \text{ --(2.62)}$$

Similarly, we obtain

$$(\partial^2 q(\rho') / \partial z^2) - 2i\beta' (\partial q(\rho') / \partial z) + \sum_u C_u F_u(\rho', z)$$

$$+\sum_0^{\infty} q(\rho) G(\rho, \rho') d\rho = 0 \text{ -----(2.63)}$$

$$\text{where } F_u(\rho', z) = (\beta' k_0^2 / 2w_{u0} P) \int_{-\infty}^{\infty} E_y^*(\rho') \eta(x, z) E_y dx \text{ -----(2.64)}$$

$$\text{and } G(\rho, \rho') = (\beta' k_0^2 / 2w_{u0} P) \int_{-\infty}^{\infty} E_y^*(\rho') \eta(x, z) E_y(\rho) dx \text{ ----(2.65)}$$

The propagation constant of the radiation modes on  $\rho'$  (a distance in the x direction) is indicated by  $\beta'$ . It is apparent that the perturbation,  $\eta$ , couples the expansion coefficients  $C_u$  and  $q(\rho)$  to each other.

Eq. (2.60) has the solution of

$$C_u(z) = A_u + B_u \exp(2i\beta_u z) + (1/2i\beta_u) (-\int_0^z \phi_u(\xi) d\xi \\ + \exp(2i\beta_u z) \int_0^z \exp(-2i\beta_u \xi) \phi_u(\xi) d\xi) \text{ -----(2.66)}$$

$$\text{with } \phi_u(\xi) = -\sum_u C_u F_{Uu}(z) - \sum_0^{\infty} q(\rho) G_u(\rho, z) d\rho \text{ -----(2.67)}$$

It is advantageous to separate the coefficient  $C_u$  into two parts.

The first part

$$C_u^+ = A_u - (1/2i\beta_u) \int_0^\infty \phi_u(\xi) d\xi \quad (2.68)$$

contributes to waves traveling in the positive  $z$  direction. The

second part

$$C_u^- = (B_u + (1/2i\beta_u) \int_0^z \exp(-2i\beta_u \xi) \phi_u(\xi) d\xi) \exp(2i\beta_u z) \quad (2.69)$$

contributes to waves traveling in the negative  $z$  direction.

The coefficients  $A_u$  and  $B_u$  must be determined from the initial conditions. We assume that the lowest order TE mode is entering longitudinally from a perfect slab waveguide into a waveguide section, of length  $L$ , which contains wall imperfections. The imperfect piece of waveguide is again followed by a perfect waveguide of infinite length. This mode allows us to calculate the loss contribution of an imperfect waveguide section of length  $L$ . We assume that at  $z=0$  only lowest order TE mode travels in the pos- $z$  direction. This implies

$$C_0^+(0) = 1 \quad (2.70)$$

$$\text{and } C_u^-(0) = 0 \quad \text{for } u \neq 0 \quad (2.71)$$

We postulate that at  $Z=L$  no modes travel in neg- $z$  direction

$$C_u^-(L) = 0 \quad \text{for all } u \quad (2.72)$$

The initial conditions of Eqs. (2.71) and (2.72) lead to

$$A_u = \delta_{ou} \text{-----}(2.73)$$

$\delta_{ou}$  is the Kronecker delta symbol, which is zero for  $u \neq 0$  and unity for  $u=0$ . The condition of Eq. (2.72) leads to

$$B_u = (-1/2\beta_u) \int_0^L \exp(-2i\beta_u \xi) \phi_u(\xi) d\xi \text{-----(2.74)}$$

The total power loss can be expressed by the following equation

$$\Delta P = P_T(L) - P_T(0) = P \sum_{u=0}^{\infty} ((1 - \delta_{ou}) |c_u^+(L)|^2 + |c_u^-(0)|^2) + \sum_I^2 \int_0^{\infty} (|q^+(\rho, L)|^2 + |q^-(\rho, 0)|^2) d\rho \text{-----(2.75)}$$

The summation from one to two in Eq. (2.75) reminds us to add the losses contributed by the even and odd radiation modes.

Using this method, we obtain general formulas for the power loss in a symmetric slab waveguide although further approximation is needed for practical application.

In the next section, we introduce a simple theory<sup>18</sup> for an asymmetric slab waveguide.

### 2.2.3 Simple Theory of Surface Scattering for an Asymmetric Slab Waveguide

For an asymmetric slab waveguide, the two surfaces of guiding film scatter light differently. Since it is virtually impossible to measure the scattering losses of the two surfaces separately, all the surface properties of the guiding film are lumped into a single parameter. We use this parameter to calculate the scattering losses of different waveguide modes.

A dielectric asymmetric slab waveguide is shown in Fig. 2.8. Let us consider a space of unit length in the  $y$  direction and assume  $(\partial/\partial y=0)$  (i.e., it is infinitely long in the  $y$  direction). If a light wave is incident upon the upper surface of the guiding region covering a unit length of the film in the  $y$  direction, the plane wave has a width of  $\cos\theta$  in the direction parallel to the wavefront. Considering a TE wave, the incident power  $P$  carried by the plane wave is given by<sup>18</sup>

$$P = (1/2)n_1 E_y^2 \sqrt{\epsilon_0/\mu_0} \cos\theta \text{ -----(2.76)}$$

where  $\mu_0$  and  $\epsilon_0$  are the permeability and permittivity of free space respectively,  $\theta$  is the incident angle,  $n_1$  is the refractive index of the film and  $E_y$  is the field amplitude. According to the Rayleigh criterion<sup>19</sup>, the specularly reflected beam from the upper film surface has a power  $P'$ ,<sup>18</sup>

$$P' = (1/2)n_1 E_y^2 \sqrt{\epsilon_0/\mu_0} \cos\theta \exp(-4\pi\delta_{12} \cos\theta/\lambda_1) \text{ ----(2.77)}$$

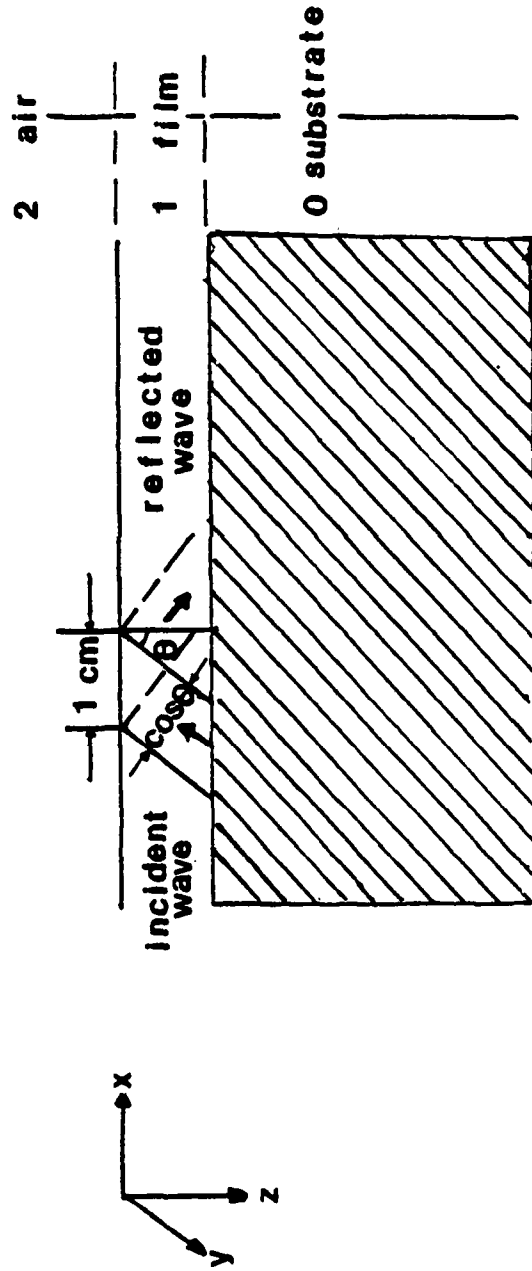


Fig. 2.8 A asymmetric waveguide which a thin-film of thickness  $W$  is grown on top of a substrate. The waveguide is assumed to be infinitely long in the  $y$  direction. The substrate, film and air are denoted by 0, 1, and 2, respectively.

where  $\lambda_1$  is the wavelength in the guiding region, and  $\delta_{12}$  is the standard deviation of the upper film surface roughness (i.e., the root-mean-square deviation from its mean value). The power loss due to the upper film surface scattering is  $P-P'$ . Similarly, the power loss due to the lower film surface scattering can be obtained by replacing  $\delta_{12}$  by  $\delta_{10}$  in equation 2.77. The total power losses,  $\Delta P$ , at two surfaces of the guiding film is therefore

$$\begin{aligned} \Delta P &= (1/2)n_1 E_y^2 \sqrt{\epsilon_0/\mu_0} \cos\theta (1 - \exp - K^2 \cos\theta) \\ &\approx (1/2)n_1 E_y^2 K^2 \cos^3\theta \sqrt{\epsilon_0/\mu_0} \quad \text{-----(2.78)} \end{aligned}$$

$$\text{with } K = 4\pi/\lambda_1 (\delta_{12}^2 + \delta_{10}^2)^{1/2} \quad \text{-----(2.79)}$$

We have obtained a simple parameter  $K$  which contains the surface properties of the guiding dielectric. It is a dimensionless parameter and quantitatively compares surface roughness with the optical wavelength.

The dielectric slab waveguide is a useful model for more complicated waveguide structures. Its simplicity allows us to study the properties of wave propagation in dielectric waveguide without encumbrance of tedious mathematical expressions. However, in most practical applications more complicated waveguides are used: integrated optics use rectangular strips of dielectric material that are embedded in other dielectrics.

#### 2.2.4 The Surface-Scattering Losses of a Rectangular Dielectric Waveguide

A wave propagating along the z-direction in a rectangular dielectric waveguide with dimensions a and b (Fig. 2.9) is formulated and solved in this section. An exact analytical treatment of this problem is impossible, and therefore, Marcatili's<sup>20</sup> approximate, analytical approach is followed. This approach works only for modes much greater than cutoff. For modes of this type, its field is confined to the region of the core. Very little field energy is carried in the surrounding media. Let us simplify the analysis by ignoring the field energy carried in the shaded regions of Fig. 2.9.

##### Maxwell's equations

$$\nabla_{\mathbf{x}} \vec{\mathbf{H}} = \epsilon_0 n^2 (\partial \vec{\mathbf{E}} / \partial t) \quad \text{and} \quad \nabla_{\mathbf{x}} \vec{\mathbf{E}} = \mu_0 (\partial \vec{\mathbf{H}} / \partial t)$$

can be solved to express the transverse field in terms of longitudinal components  $E_z$  and  $H_z$ , if a traveling wave propagating in the Z-direction with incident angle  $\theta$  is assumed (Fig. 2.4).

$$E_x = (-1/K^2)(\beta(\partial E_z / \partial x) + \mu_0 \omega(\partial H_z / \partial y)) \quad \text{-----} (2.80)$$

$$H_y = (-1/K^2)(\beta(\partial H_z / \partial y) + \omega \epsilon_0 n^2 (\partial E_z / \partial x)) \quad \text{-----} (2.81)$$

$$E_y = (-1/K^2)(\beta(\partial E_z / \partial y) - \omega \mu_0 (\partial H_z / \partial x)) \quad \text{-----} (2.82)$$

$$H_x = (-i/K^2)(\beta(\partial H_z/\partial x) - w\epsilon_0 n^2(\partial E_z/\partial y)) \text{ -----(2.83)}$$

$$\text{with } K = \sqrt{(n^2 k^2 - \beta^2)} \text{ -----(2.84)}$$

where  $n$  is refractive index of the dielectric,  $k$  is the wave vector in free space,  $w$  is the angular frequency of the wave and  $\beta$  is the propagation constant in  $z$ -direction. The longitudinal components  $E_z$  and  $H_z$  must satisfy the reduced wave equation

$$(\partial^2 \psi / \partial x^2) + (\partial^2 \psi / \partial y^2) + K^2 \psi = 0 \text{ -----(2.85)}$$

Two different types of modes can be supported in the waveguide<sup>16,17</sup>, e.g.,

$E_{pq}^x$  : polarized in  $x$  direction, and

$E_{pq}^y$  : polarized in  $y$  direction

where  $p$  and  $q$  are positive integers indicating the number of extrema of the electric or magnetic field in the  $x$  and  $y$  direction. In the  $E_{pq}^x$  modes, the main transverse field components are  $E_x$  and  $H_y$ . Within the waveguide each component varies sinusoidally both along the  $x$  and  $y$  directions. In region 1, with refractive index  $n$ , as shown in Fig. 2.9, the wave equation can be solved to give

$$E_z(x,y) = A \cos k_x(x+\xi) \cos k_y(y+\eta) \text{ -----(2.86)}$$

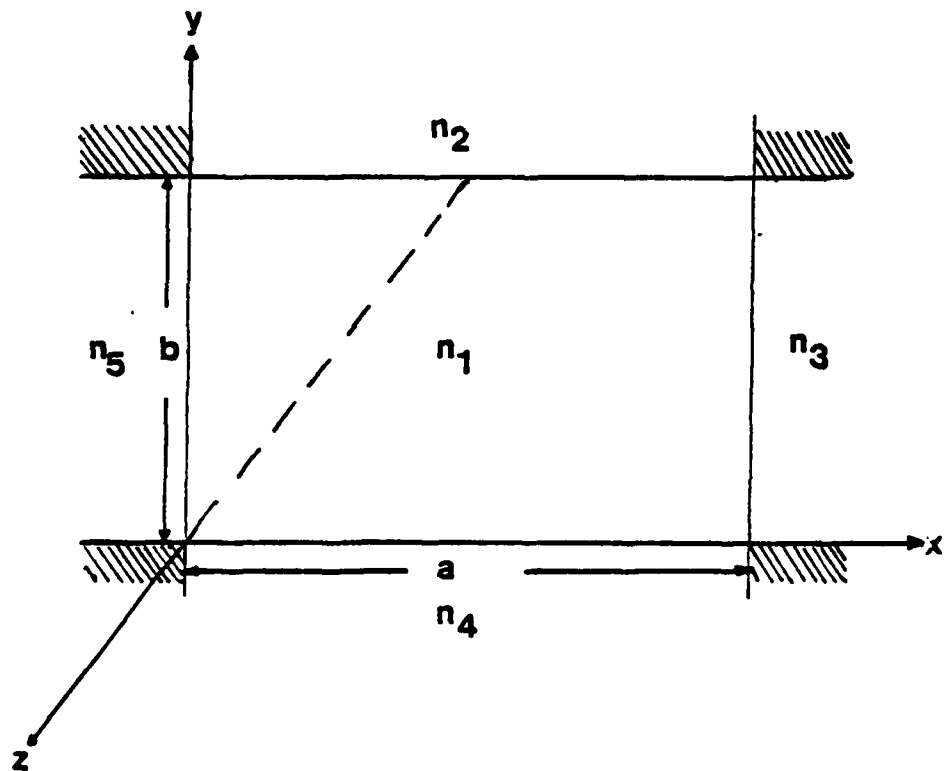


Fig. 2.9 Cross section of a rectangular dielectric waveguide with dimensions  $a$  and  $b$ .  $n_1$ ,  $n_2$ ,  $n_3$ ,  $n_4$  and  $n_5$  are the indices of refraction in regions 1 to 5, respectively.

where  $\xi$  and  $\eta'$  are the phase factors of  $E_z$  with  $H_x=0$ , we can obtain the expression for  $H_z$  from Eq. (2.83)

$$H_z = -A(n_1^2/\beta) \sqrt{(\epsilon_0/\mu_0)} (k_y/k_x) \text{sinc}_x(x+\xi) \text{sinc}_y(y+\eta') \quad (2.87)$$

Other components of the wavefunction can be obtained by substituting Eqs. (2.86) and (2.87) into Eqs. (2.80), (2.81) and (2.82).

$$E_x = (i A/k_x \beta) (n_1^2 k^2 - k_x^2) \text{sinc}_x(x+\xi) \text{cosk}_y(y+\eta') \quad (2.88)$$

$$E_y = -iA(k_y/\beta) \text{cosk}_x(x+\xi) \text{sinc}_y(y+\eta') \quad (2.89)$$

$$H_x = iA(\epsilon_0/\mu_0)n_1^2(k/k_x) \text{sinc}_x(x+\xi) \text{cosk}_y(y+\eta) \quad (2.90)$$

$$\text{with } k^2 = \omega^2 \epsilon_0 \mu_0 \text{ and } n_1^2 k^2 - \beta^2 = k_x^2 + k_y^2 \quad (2.91)$$

For well-guided modes  $\beta \approx n_1 k$ . This relation together with Eq. (2.91) result the inequalities

$$k_x \ll \beta \text{ and } k_y \ll \beta \quad (2.92)$$

Owing to the inequalities in Eq. (2.92), it is clear that  $E_y \ll E_z$ , and  $E_y$  can be neglected. Thus, there are only four nonvanishing components.

Similarly, the wavefunctions in the surrounding regions 2,3,4, and 5 with their respective refractive indices  $n_2$ ,  $n_3$ ,  $n_4$ , and  $n_5$  can be obtained. When boundary conditions are matched between region 1 and neighboring regions (i.e., regions 2,3,4 and 5) four transcendental equations are obtained:

$$\tan k_x a = n_1^2 k_x (n_3^2 s_5 + n_5^2 s_3) / (n_3^2 n_5^2 k_x^2 - n_1^4 s_3 s_5) \quad (2.93)$$

$$\tan k_x \xi = (n_5/n_1)^2 (k_x/s_5) \quad (2.94)$$

$$\tan k_y b = k_y (s_2 + s_4) / (k_y^2 - s_2 s_4) \quad (2.95)$$

$$\tan k_y \eta = -s_4/k_y \quad (2.96)$$

$$\text{with } s_i = ((n_1^2 - n_i^2)k^2 - k_y^2) \text{ for } i=2,3,4, \text{ and } 5 \quad (2.97)$$

The computer program in appendix, was developed to solve  $k_x$  and  $k_y$  by means of Newton's method. Once  $k_x$  and  $k_y$  are determined, the propagation constant can be obtained from Eq. (2.91). The total power  $P$  carried by  $E_{pq}^x$  mode in the  $z$  direction given by

$$P = n_1 \sin \theta / (2\sqrt{\mu_0/\epsilon_0}) (\iint E_y dx dy) = n_1 \sin \theta A^2 / (4\sqrt{\mu_0/\epsilon_0})$$

$$(b + 1/s_2 + 1/s_4) (a + (n_1^2 n_3^2 / s_3) (k^2 + s_3^2) / (n_3^4 k^2 + n_1^4 s_3^2))$$

$$+ (n_1^2 n_5^2 / s_5) (k^2 + s_5^2) / (n_5^4 k^2 + n_1^4 s_5^2) \quad (2.98)$$

If a plane wave is incident on the interface between region 1 and region 2, with an incident angle of  $\theta$  covering the complete length of core in the  $y$  direction, the plane wave has a width of  $\cos \theta$  in the

direction parallel to the wavefront. The incident power  $P$  carried by the plane wave is given by

$$P = (1/2)n_1 A^2 b \sqrt{\epsilon_0/\mu_0} \cos\theta \text{ -----(2.99)}$$

where  $A$  is the field amplitude. The power loss  $\Delta P$  at the two interfaces is given by

$$\begin{aligned} \Delta P &= (1/2) n_1 A^2 \sqrt{\epsilon_0/\mu_0} \cos\theta (1 - \exp(-K^2 \cos^2\theta)) b \\ &\approx (1/2) n_1 A^2 K^2 \cos^3\theta b \sqrt{\epsilon_0/\mu_0} \text{ -----(2.100)} \end{aligned}$$

$$\text{with } K = 4\pi / (\delta_{12}^2 + \delta_{13}^2)^{1/2}$$

where  $\delta_{12}$  and  $\delta_{13}$  are the standard deviation of the interfaces between media 1 and 2, and between media 1 and 3, respectively. Dividing Eq. (2.100) by Eq. (2.98), yields the power attenuation per unit length of the waveguide

$$\begin{aligned} \alpha &= K^2 (\cos^3\theta / \sin\theta) (a + (n_1^2 n_3^2 / s_3) ((k^2 + s_3^2) / (n_3^4 k^2 + n_1^4 s_3^2)) \\ &+ (n_1^2 n_5^2 / s_5) (k^2 + s_5^2) / (n_5^4 k^2 + n_1^4 s_5^2))^{-1} + (b + l/s_2 + l/s_4)^{-1} \text{ ---(2.101)} \end{aligned}$$

This is the loss caused by surface scattering. This loss is expressed as a product of four independent factors. The first factor  $K$ , depends solely on the surface properties of interfaces and is dimensionless. The second factor involving  $\theta$  depends on the waveguide mode. The third and fourth factors are the effective waveguide thickness and width, respectively.

## CHAPTER 3

## EXPERIMENTAL METHODS

## 3.1 Auger Electron Spectroscopy (AES)

Auger electron spectroscopy is a nondestructive method of surface chemical analysis. It explores the electronic energy levels in atoms and solids by analyzing the energies of the electrons ejected from a specimen bombarded with an electron beam. Some of the ejected electrons result from the "Auger process". The "Auger process" involves any electron de-excitation in which this de-excitation energy is transferred to and causes the ejection of a second electron, the "Auger electron". Because of the discrete nature of most electronic energy levels, the energy of the Auger electron is characteristic of the atom from which it was ejected. If the Auger electron is created within a few atomic layers of the specimen surface, it can migrate to the surface and escape into the vacuum without loss of energy. Thus, the Auger electrons produce peaks in the secondary electron energy distribution and the measurement of these energies indicate the type of atoms present.

Auger electrons were first discovered in 1925 by Pierre Auger<sup>21</sup>. These electrons are produced by the "Auger process" as shown in Fig. 3.1<sup>22</sup> for a silicon atom. The electronic energy levels of the single ionized atoms are listed on the left, taking the Fermi level  $E_F$  as zero energy. The x-ray levels, K, L, M..., are also labeled

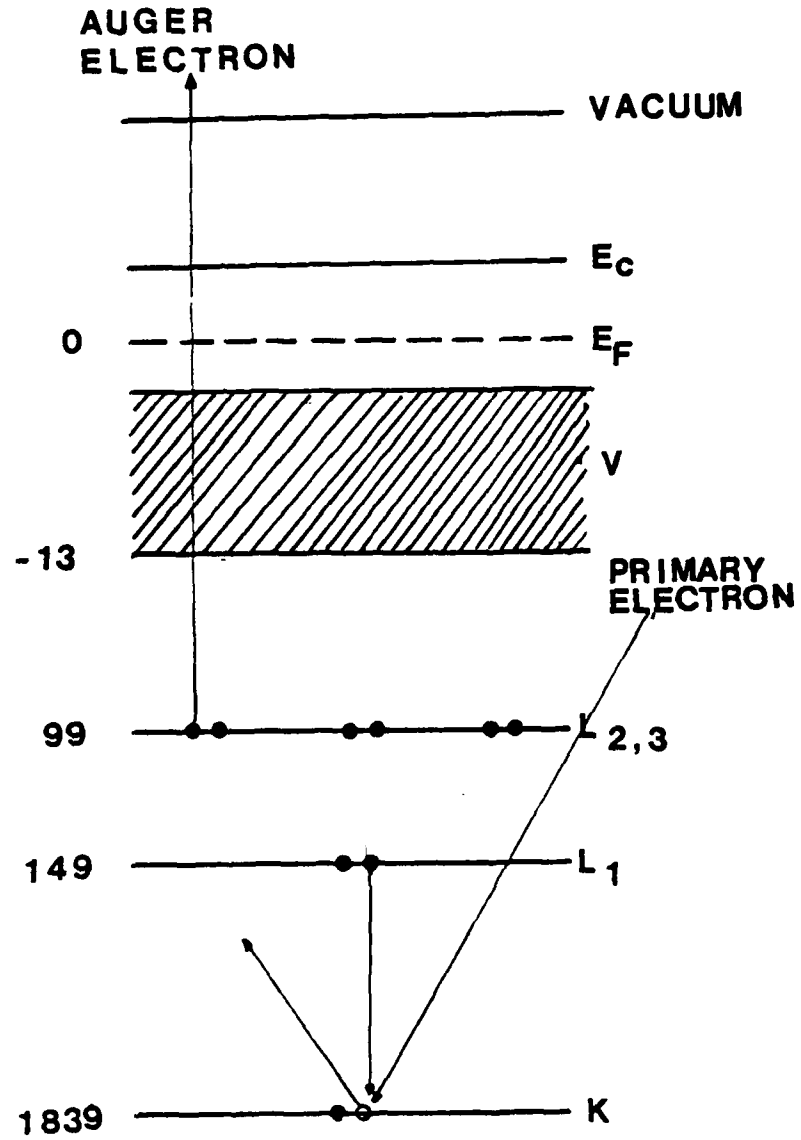


Fig. 3.1 The x-ray energy level diagram of silicon.  
A  $KL_1L_{2,3}$  Auger process is depicted.

on the right. Fig. 3.1 shows the atom immediately after a K-shell ionization by a primary electron. The Auger process initiates when an outer electron fills this "hole", as shown for an  $L_1$  electron, and the energy released by this transition is either emitted as a photon or given to another electron. If this energy is sufficient, an electron can be ejected from the atom, as illustrated for another electron at  $L_{2,3}$ . The process just described is called the  $KL_1L_{2,3}$  Auger transition. The energy  $E$  of the ejected electron can be approximated by the diagram of Fig. 3.1. The energy released is  $E_K - E_{L1}$ ; however, the ejected electron must expend the energy  $(E'_{L2,3} + \phi)$  to escape the atom.  $\phi$  is the work function of the material and  $E'_{L2,3} \neq E_{L2,3}$  is due to the extra positive charge of the atom. Because of this positive charge,  $E'_{L2,3}$  should be approximately equal to the  $L_{2,3}$  ionization energy of the next heavier element, or  $E'_{L2,3} = E_{L2,3}(Z+\Delta)$ , where  $Z$  is the atomic number and  $\Delta=1$  accounts for the extra charge. We then have<sup>22</sup>

$$E(Z) = E_K(Z) - E_{L1}(Z) - E_{L2,3}(Z+\Delta) - \phi \quad \text{-----} (3.1)$$

Eq. (3.1) can be generalized to any Auger event involving the levels  $WXY$ . The actual measured energy will have an additional term  $(-\phi_A + \phi)$  which is the difference between the work functions of the energy analyzer  $\phi_A$  and the material under investigation. This gives

$$E_{WXY}(Z) = E_W(Z) - E_X(Z) - E_Y(Z+\Delta) - \phi_A \quad \text{-----} (3.2)$$

In practical applications, Auger peaks can be greatly enhanced by recording the derivative of the secondary electron energy distribution. This technique improves the sensitivity and resolution of the measurement and removes the large slowly changing background upon which the Auger signal is superimposed. Thus, the conventional Auger spectrum is the function  $dN(E)/dE$ . The locations of the Auger peaks are specified by the energies of the negative excursions of the peaks in the Auger spectrum. The peak-to-peak magnitude of an Auger peak in a differential spectrum generally is directly related to the surface concentration of the element which produces the Auger electrons. Quantitative analysis may be accomplished by comparing the peak heights obtained from an unknown specimen with those from pure elemental standards or from compounds of known composition.

Since the escape depth without energy loss for Auger electrons in the practical energy range is typically less than a few atomic layers, Auger electron spectroscopy (AES) is primarily a surface analytical technique. The sensitivity of the Auger technique is determined by the transition probability of the Auger transitions involved, and the incident beam current and energy. The limit of detection is around 1% of a monolayer, and the sensitivity varies less than a factor of 10 over all elements except hydrogen and helium which cannot be detected.

Our experimental arrangement for obtaining the Auger spectra is shown in Fig. 3.2. Several specimens were mounted on the manipulator and sequentially rotated into the analysis position. The analysis

was carried out with the excitation beam normal to the specimen surface. The basic function of each of the electronic units is indicated in Fig. 3.2. The Electron Gun Control operates the electron gun, the Auger System Control supplies the modulated scan voltage for the cylindrical analyzer, and the lock-in Amplifier provides phase sensitive detection of the electron multiplier output. The gain of the electron multiplier can be adjusted for optimum performance using the Electron Multiplier Supply. Readout of the Auger spectrum is provided by an oscilloscope or X-Y recorder. Auger data was taken in the  $dN(E)/dE$  mode. Electronic differentiation was accomplished with a velocity analyzer by superimposing a small a.c. voltage on the energy selecting voltage and synchronously detecting the output of the electron multiplier. The operating conditions were 2V peak-to-peak a.c. modulation, an incident electron current of 10-15 $\mu$ A, and an incident electron energy of 5KeV, unless otherwise specified. The system is capable of continuously maintaining pressures less than  $1 \times 10^{-9}$  torr.

Ion-sputtering was accomplished by using an ion gun as shown in Fig. 3.2 which produced an Ar ion beam in a static Ar pressure of  $5 \times 10^{-5}$  torr. The ion and electron beams were mutually perpendicular and were approximately aligned to focus on the same area of the testing surface. Ion-sputtering can be used along for cleaning purposes or, when combined with AES, for analyzing the surface to obtain the chemical depth profiles.

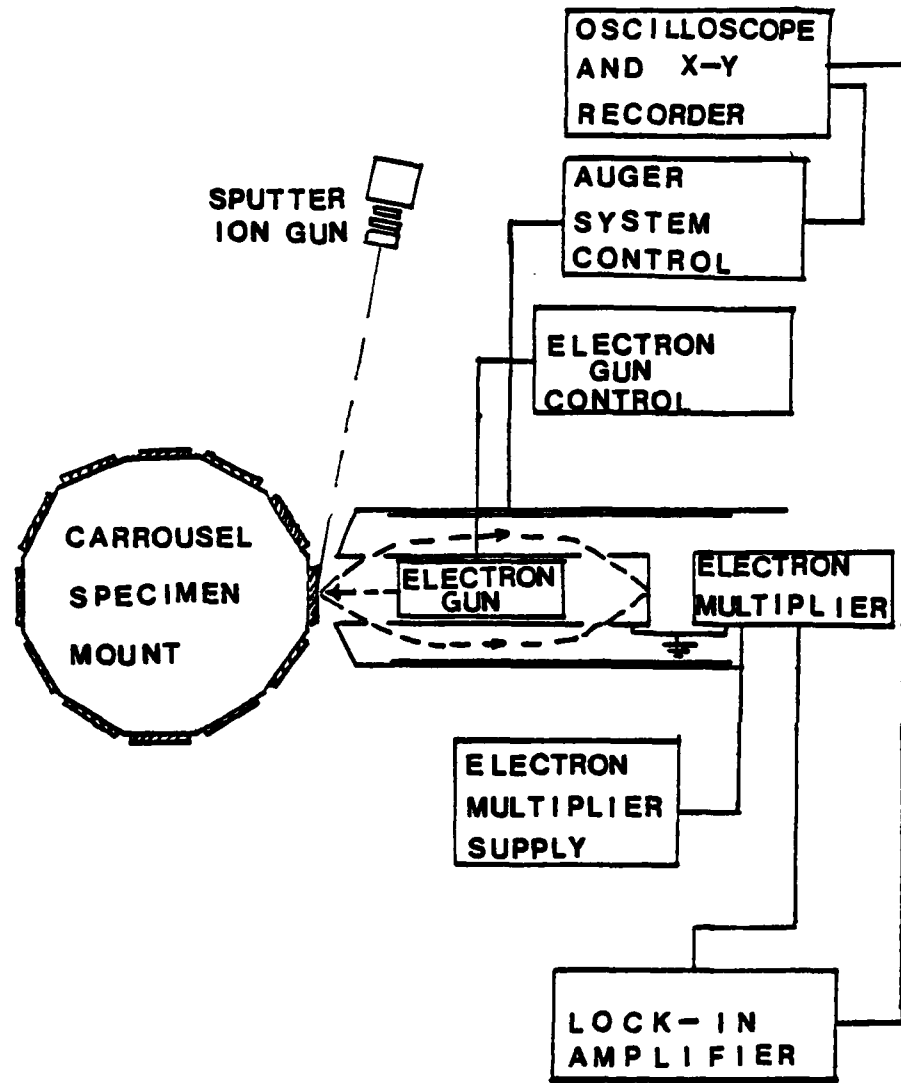


Fig. 3.2 Schematic of the experimental arrangement used for obtained Auger spectra.

### 3.2 Laser Scattering

The laser scattering technique<sup>23</sup>, shown in Fig. 3.3, was performed to characterize the surface geometry (i.e., degree of "smoothness") of GaAs substrates. An average "Bidirectional Reflectance Function" (BRDF) number was used to describe the degree of surface smoothness of the tested sample. The BRDF number<sup>24</sup> is defined as

$$\text{BRDF} = (P_r/P_i) (\cos\theta_i \sin\phi_i) (A \cos\theta_r \sin\phi_r / R^2) \text{-----} (3.3)$$

where  $P_r$  is the scattered power collected by a photometer with aperture area  $A$ ,  $P_i$  is the power incident on the sample, and  $\phi_i$  is the incident beam angle measured from vertical axis  $Z$  (as shown in Fig. 3.3).  $\phi_r$  denotes the scattered beam angle measured from  $Z$  axis,  $\theta_i$  denotes the incident beam angle measured from horizontal axis  $Y$  and  $\theta_r$  is the angle of the reflected beam. The diameter of the incident laser beam was  $0.5\text{mm}^2$ , as shown in Fig. 3.4. The sample holder is automatically controlled to have translation and rotation movements in the  $X$ - $Z$  plane which allows the incident beam to scan over an area of  $9\text{mm}^2$  around the center of each sample. Five locations of each sample, depicted in Fig. 3.4, were first rotationally scanned by the incident beam. The BRDF values vs. rotational angle were plotted, and from these curves the directions at which the maximum and minimum scatter occurred was determined. Each sample was then scanned translationally along the maximum and minimum directions separately, and then the average BRDF value was obtained. The average BRDF value quantitatively characterizes the degree of surface roughness.

The parameter  $K$  discussed in section 2.2.4 can be characterized by the average BRDF value.

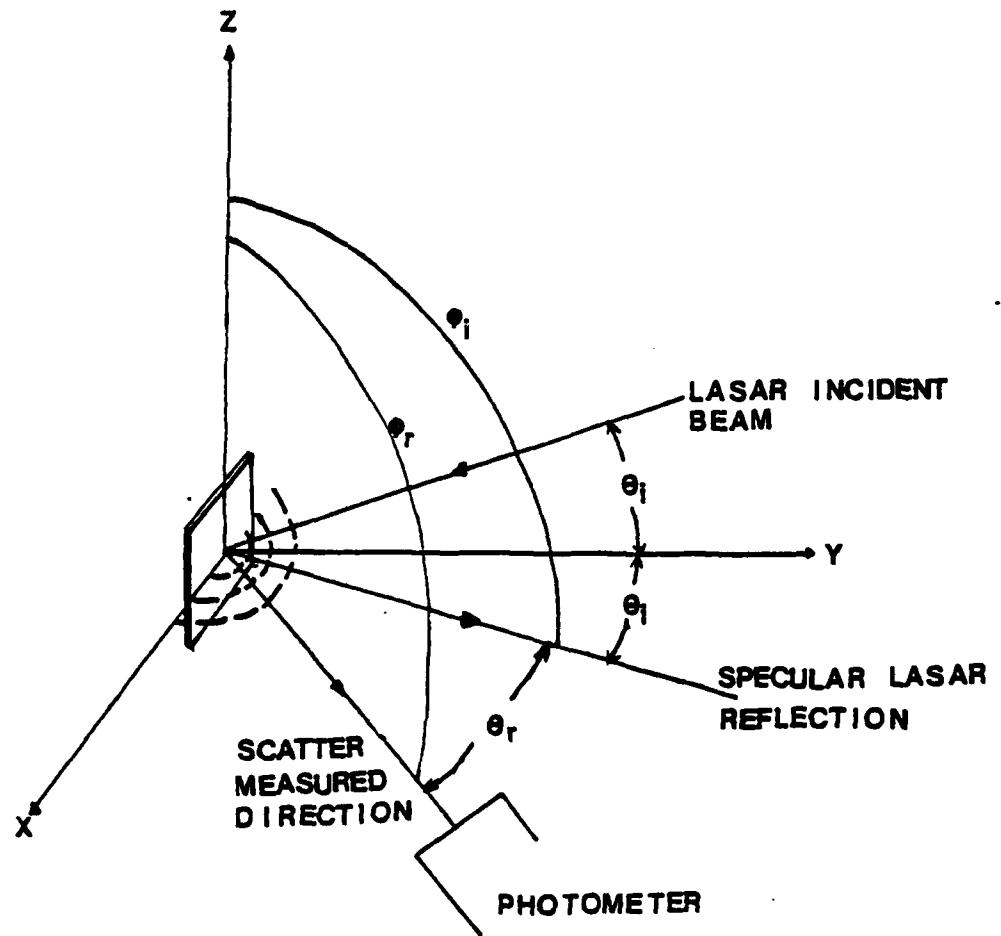


Fig. 3.3 A schematic diagram of laser scattering measurement.

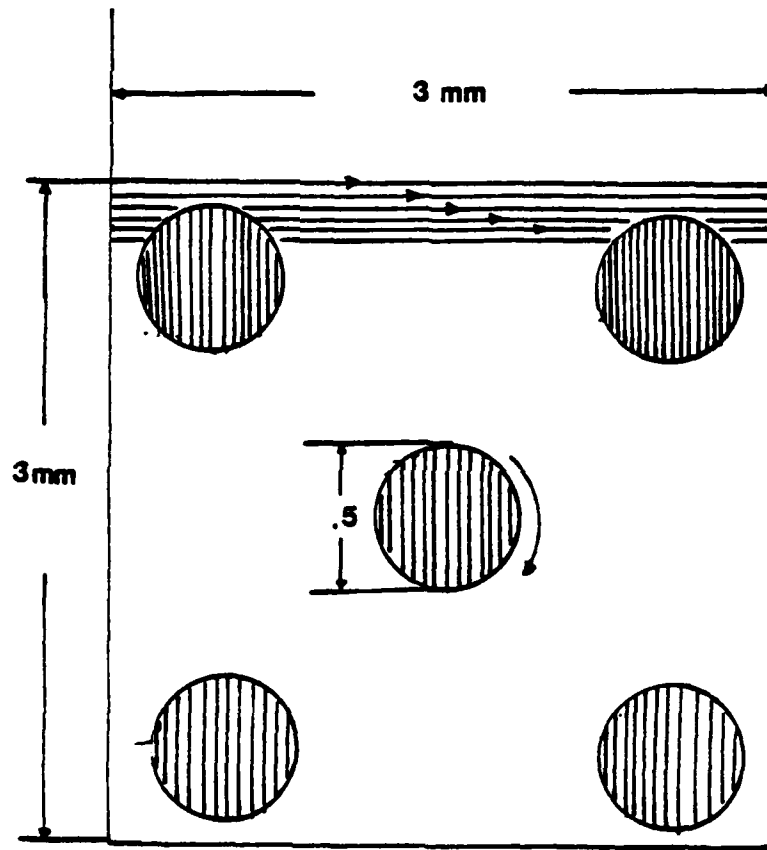


Fig. 3.4 The area scanned by incident laser beam.

### 3.3 Anodic Oxidation

An Anodic oxidation scheme<sup>25</sup> is suggested for use in forming a rib waveguide. The waveguide, which consists of a lightly-doped ( $10^{15} \text{ cm}^{-3}$ ) GaAs substrate with a rib etched into the lightly-doped GaAs layer, can be used to investigate the surface-scattering losses of III-V semiconductor waveguides.

The experimental setup employed for anodic oxidation is shown in Fig. 3.5. A quartz or pyrex beaker with a platinum cathode was used to contain an electrolyte of D.I.-water with PH adjusted to 2.5 by the addition of phosphoric acid. The GaAs samples are either partly or fully immersed in the electrolyte while held by an aluminum clamp. Either a constant current or a constant voltage supply can be selected as the power source.

The growth of a surface oxide on GaAs is carried out by polarizing the GaAs sample positively with respect to the platinum electrode. Both the oxide thickness and GaAs consumed in the oxide growth are proportional to the anodization voltage (20 and 12 A/V, respectively)<sup>26</sup>. The sample can then be etched in KOH as the surface oxide is cracked away to give the desired rib shape.

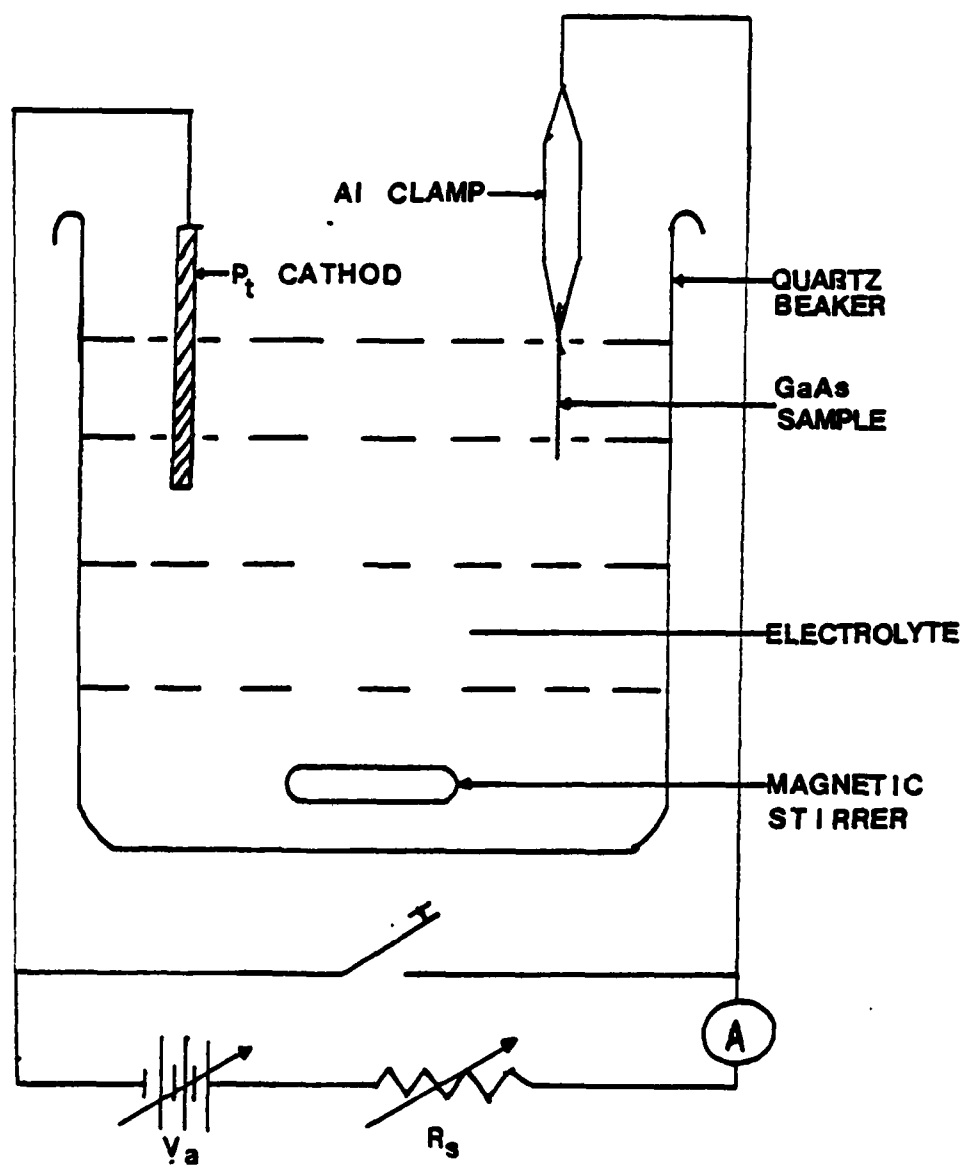


Fig. 3.5 Experimental setup for anodic oxidation.

### 3.4 Electrical Measurements

#### 3.4.1 Resistivity Measurement

Resistivity measurements carried out by the four-point probe<sup>27,28</sup> and Van-der Pauw<sup>29</sup> methods were used to determine the doping concentrations of the GaAs substrates as stated in the previous section. The results obtained by both methods showed good agreement.

The four-point probe method, as shown in Fig. 3.6, is the most common method for measuring resistivity. A small current (I) (1 to 100 mA in our case) supplied from a constant current source is passed through the outer two probes and the voltage (V) between the inner two probes is measured. The spacing S between the probe is one millimeter. For a thin sample with thickness W (in the present case the thickness is  $5 \times 10^{-2}$  cm), the resistivity is given by<sup>10</sup>

$$\rho = (V/I) \cdot CF \cdot W \text{ ohm-cm} \text{ -----} (3.4)$$

where CF is the correction factor shown in Fig. 3.5. The doping concentration (N) for an n-type substrate is obtained by

$$N = 1 / (\mu_n q \rho) \text{ cm} \text{ -----} (3.5)$$

where  $\mu_n$  is the electron mobility, and q is the electron charge.

The Van-der Pauw method was carried out by making four small contacts along the circumference of the substrate as shown in Fig. 3.7 and by measuring the two resistance  $R_{AB,CD}$  and  $R_{BC,DA}$  and the thickness  $W$  of the sample. The resistance  $R_{AB,CD}$  is defined as the voltage  $V$  across the contacts  $D$  and  $C$  per unit current through the contacts  $A$  and  $B$ . The resistivity is given by

$$\rho = 2.72 (R_{AB,CD} + R_{BC,DA}) f(R_{AB,CD}/R_{BC,DA}) \text{-----} (3.6)$$

where the function  $f(R_{AB,CD}/R_{BC,DA})$  is shown in Fig. 3.7.

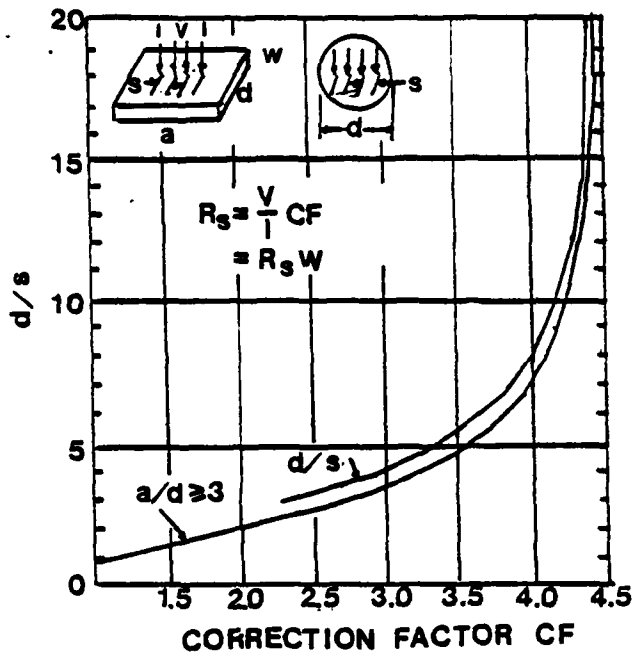


Fig. 3.6 Correction factor for resistivity measurement using a four-point probe.

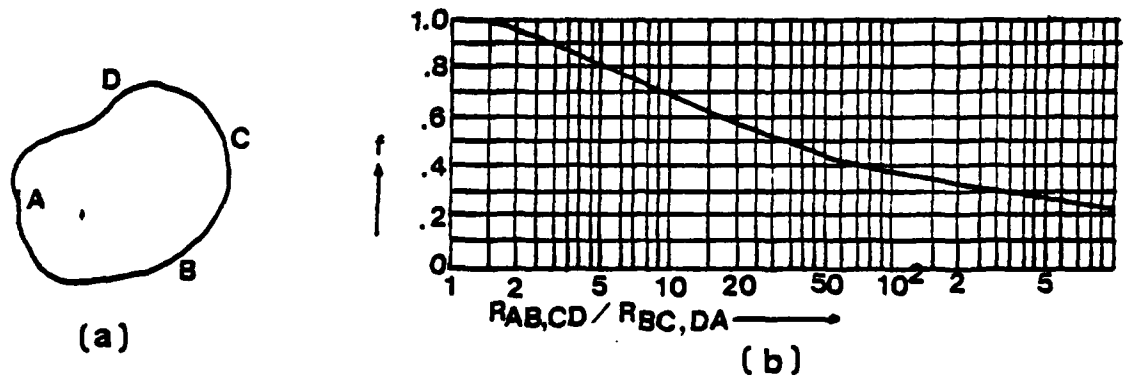


Fig. 3.7 Resistivity measurements using Van-Der Pauw method, (a) a sample of arbitrary shape with four contacts at vary place (b) the function  $f$  used for determining the resistivity.

### 3.4.2 Current-Voltage (I-V) Characteristics

The circuit diagram, shown in Fig. 3.8, was used to measure the I-V characteristic under forward bias for GaP Schottky diodes. The sample was mounted in a shielded box with a spring loaded copper wire making contact to the top electrode. The current through the diode was measured using an electrometer (PAR 135). The current ranged from fractions of a nanoampere to microamperes for GaP with aluminum or gold Schottky contacts. The I-V curves were then plotted, and the slope and Y-axis intercept of this curve was used to determine the barrier height ( $\phi_{bn}$ ) and the diode factor (n).

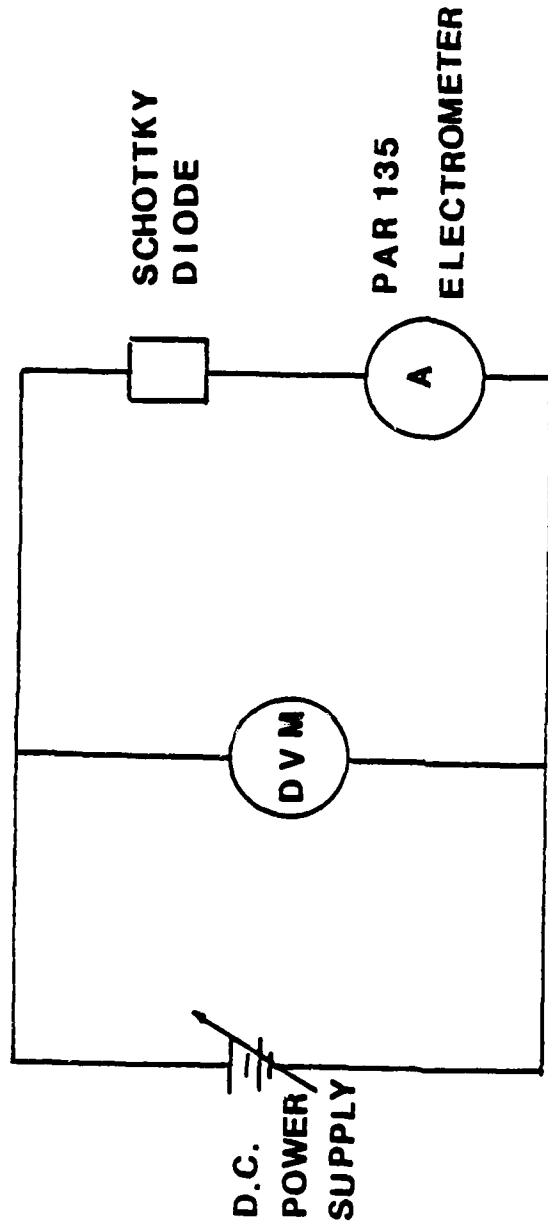


Fig. 3.8 I-V measurement using electrometer.

### 3.4.3 Capacitance-Voltage (C-V) Measurement

The C-V characteristics under reverse bias for GaP Schottky diodes were measured using a Boonton capacitance meter operating at 1 MHz as shown in Fig. 3.9. The d.c. bias was applied using a regulated power supply connected to the back of the instrument. The a.c. signal superimposed on d.c. bias was applied to the GaP Schottky diode.

For a Schottky barrier<sup>30</sup>, at reverse bias and high frequency, the capacitance per unit area C is given by

$$C = (q\epsilon_S N_D / 2(V - \phi_{bn}))^{1/2} \quad (3.7)$$

where q is the electron charge,  $\epsilon_S$  is dielectric constant of GaP,  $N_D$  is the carrier concentration in the GaP substrate and  $\phi_{bn}$  is the barrier height. The plot of  $1/C^2$  vs. voltage V should be a straight line with slope of  $2/qN_D\epsilon_S$ , and having an intercept on the X-axis equal to  $\phi_{bn}$ .

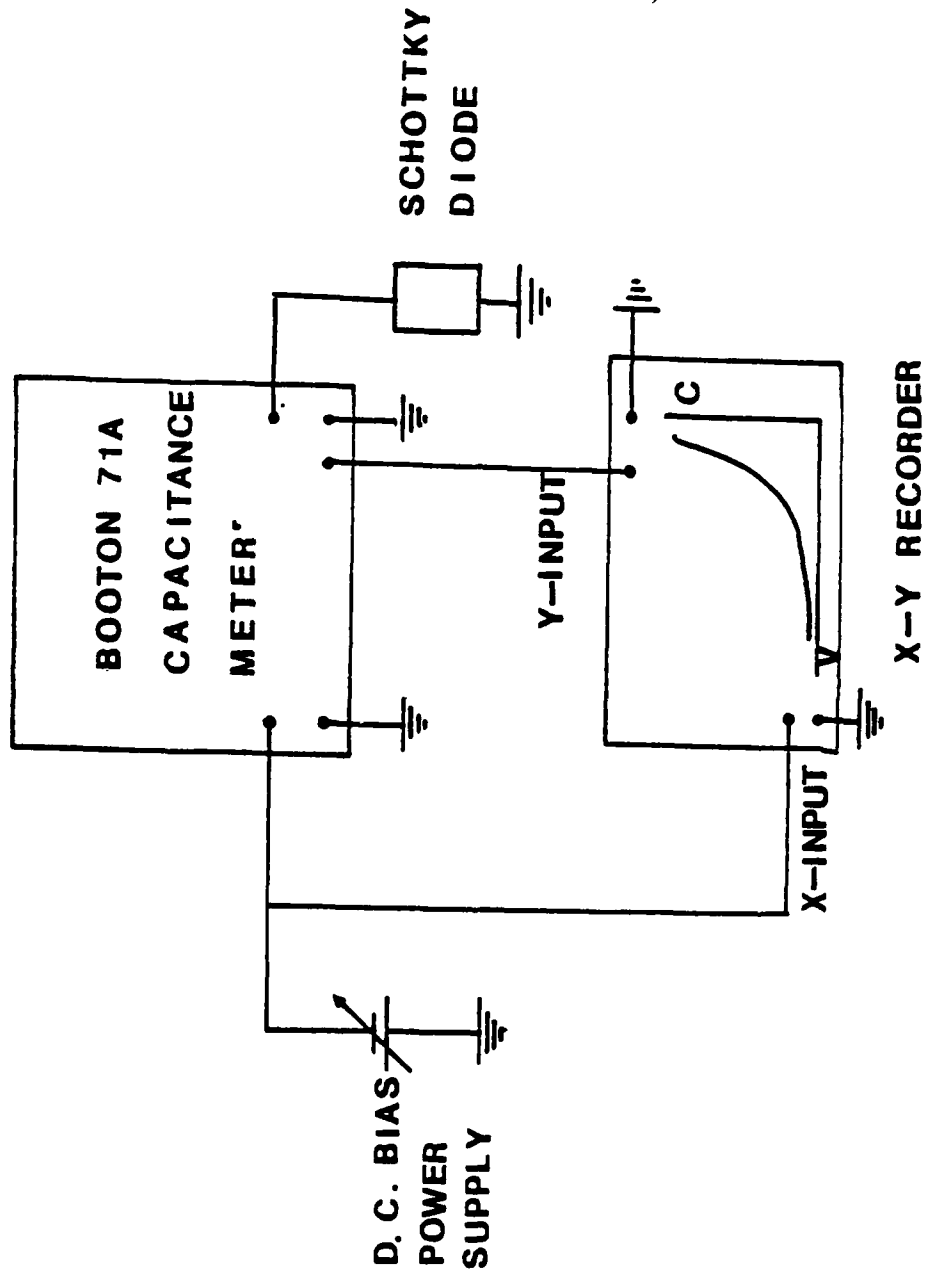


Fig. 3.9 C-V measurement using Boonton Capacitance Meter.

#### 3.4.4 Capacitance-Frequency (C-f) and Conductance-Frequency (G-f) Measurements

C-f and G-f measurements for GaP Schottky diodes at zero bias were performed using a lock-in amplifier (ITHACO model 339) along with a photometric preamplifier (Par model 184) as shown in Fig. 3.10. In the experimental setup, a capacitor C was used to prevent the bias voltage supply from interfering with the reference signal of the lock-in amplifier. The resistance R provides a high impedance path to the lock-in amplifier's reference signal and acts as a current limiting resistor in case the sample short circuited, thus preventing overloading the lock-in amplifier. The RC network acting as a high pass filter does not reduce the useable range of frequencies (1.5Hz-150KHz). The lock-in amplifier was calibrated using a suitable standard capacitor read at full scale deflection. The magnitude of the reference signal was 20 millivolts. The sample current is resolved into in-phase and quadrature components, and a d.c. voltage proportional to the current provided at the output of the lock-in amplifier. The voltage corresponding to the in-phase and quadrature components represented the conductance G and the Capacitance C, respectively.

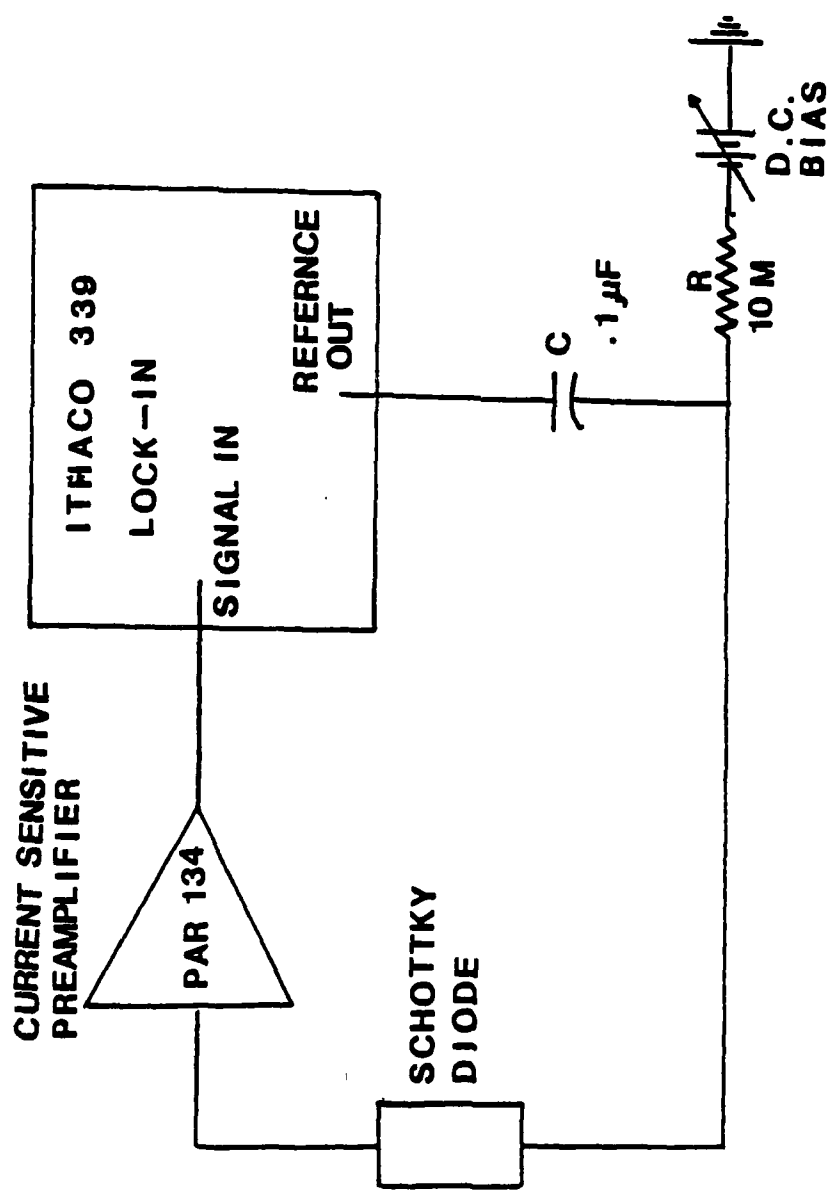


Fig. 3.10 C-f and G-f measurements using lock-in amplifier.

## CHAPTER 4

## ATOMIC STRUCTURE OF GaP (110) FACE

## 4.1 Introduction

III-V compound semiconductors are used widely in solid state electronic devices and in chemical processes which include adsorption and catalysis. Typical examples of III-V semiconductor devices which cannot be realized using elemental semiconductors include light emitting diodes (LED's), Gunn effect oscillators, and high frequency field effect transistors. Recognizing these applications, it becomes necessary to obtain a quantitative understanding of the free surface properties of compound materials so that we may develop a fabrication technology of the same quality as that which exists for silicon-based devices.

It is common knowledge that low energy electron diffraction (LEED) is a tool of great potential in the study of surface structures, and can be used quantitatively to determine the atomic structure of single crystal surfaces. The surface atomic structure of GaAs (110)<sup>31-34</sup> and InP (110)<sup>35</sup> has been successfully characterized by LEED. The atomic geometry of the GaAs (110) face was used as the starting point to study its surface chemisorption, oxidation and passivation<sup>36-38</sup>, since an accurate knowledge of surface atomic geometry is essential to most studies of surface related properties.

GaP, with an energy gap of 2.3 eV, is one of the III-V compounds used for light emitting diodes (LED's)<sup>39</sup>, and for highly efficient negative electron affinity (NEA) electron emitters<sup>40-43</sup>. It has been found that the atomic structures and surface conditions of GaP are important to the adsorption of Cs on the GaP (100)<sup>41</sup>, GaP (110)<sup>42</sup>, and GaP (111)<sup>43</sup> crystal faces. In this chapter, the results of an atomic surface structure determination for the (110) face of GaP is reported<sup>44</sup>. A quantitative determination of the structure for the GaP (110) face is obtained by comparing a dynamic computer aided simulation of LEED intensities with those measured experimentally. The LEED patterns and experimental results for the GaP (111) face are analyzed and reported, and the surface structure of the GaP (110) face is compared with that of the GaAs (110) face.

## 4.2 Experimental Considerations

All experimental measurements of the LEED intensities were performed in a standard ultrahigh vacuum LEED/AES system. The schematic diagram of the system is shown in Fig. 4.1. It consists of a four-grid hemispherical LEED optics with fluorescent screen display, a 5-KV cylindrical mirror analyzer and a rotatable, temperature-controlled, manipulator. Three sets of Helmholtz coils were used to align the incident electron beam. LEED intensities, recorded from the screen with a telescopic spot photometer and plotted out on an X-Y recorder, were subsequently corrected for variation in primary beam current and background intensity. The background intensity of the screen was recorded and subtracted from the beam intensities. The beam intensities were then normalized to the LEED-gun electron emission current. The diffraction patterns were recorded photographically. Intensity-voltage profiles were taken at normal incidence, which was assured by determining that symmetrically equivalent beams provided the same intensity profiles to within a few percent. Since this procedure is only accurate to within a few degrees, sample alignment is a major source of uncertainty in the intensity data.

The GaP sample was mounted on the sample holder of the manipulator. After insertion into the ultrahigh vacuum (UHV) chamber, the surface was cleaned by 1 Kev sputtering using argon ions for 20 min and was thermally annealed at 550°C for 1 hour. A sharp 1x1 LEED pattern was obtained for the GaP (110) face as shown in Fig.4.2(d).

An Auger profile showed that both oxygen and carbon (the principle contaminants) peaks were reduced to the limit of the analyzer resolution indicating that the surface was clean and well ordered.

LEED intensities were recorded at both room temperature and low temperatures. The sample was kept at 90K during data recording by flowing liquid nitrogen through the sample holder, and both room temperature and low temperature data were used to analyze the surface structure.

Only one set of GaP (110) LEED experimental intensity-voltage (I-V) curves<sup>45</sup> were available at the time of our data acquisition. In our work a much larger experimental data base was obtained, and was in general agreement with that recorded previously. LEED profiles for a total of 16 inequivalent nonspecular beams were recorded and analyzed. The reproducibility of the I-V curves was satisfactory. Fig. 4.2 (a), (b) and (c) show the notation for the LEED beams. The arrangement of the surface atoms of GaP (110) face viewed from the side and top positions are shown in 4.2 (a) and (b), respectively, and the notation used in labelling the (h,k) beam is shown in (c). The LEED pattern taken at 164eV with liquid nitrogen cooling the sample (95K) is shown (d).

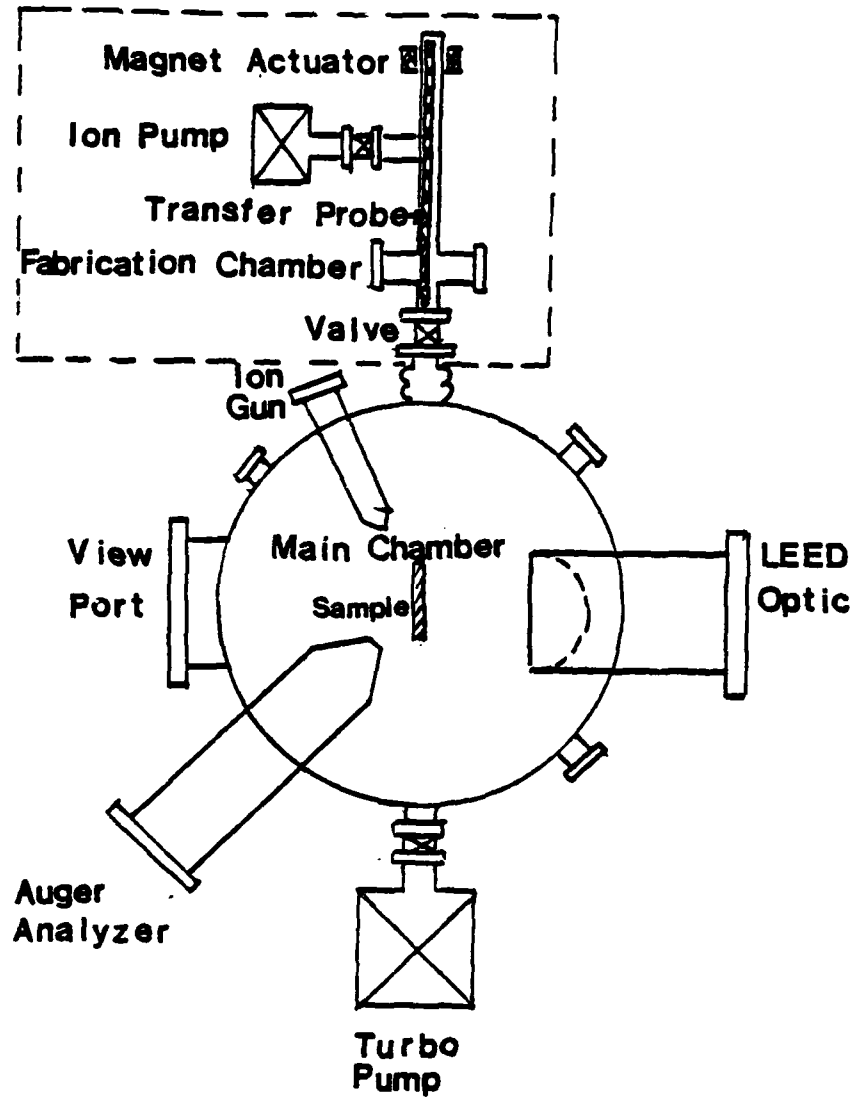


Fig. 4.1 Schematic diagram of the ultra high vacuum (UHV) system equipped with LEED, AES and ion-sputtering gun for surface analysis.

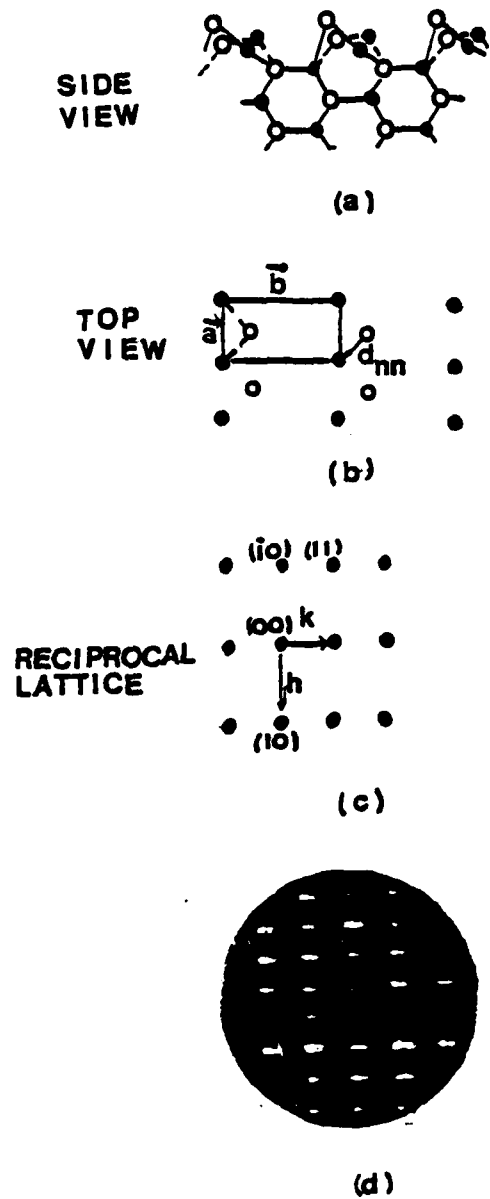


Fig. 4.2

(a) Side view of the GaP (110) face. (b) Top view of surface atoms for the undistorted GaP (110) face. ( $\bullet$ ) Ga, ( $\circ$ ) P,  $d_{nn}$  is the nearest neighbor distance. (c) The notation used in labeling the  $(h,k)$  beam. (d) LEED pattern of GaP (110) face taken at low temperature.

### 4.3 Model and Theoretical Considerations

An approximate multiple-scattering model of the diffraction process, described in section 2.5, was used to construct the computer program for calculating the theoretical I-V curves. In the intensity program, the intralayer multiple scattering was treated exactly using the direct summation method<sup>46</sup>, while for the interlayer multiple scattering, an approximate fast scheme called renormalized-forward-scattering (RFS)<sup>47,48</sup> perturbation theory, was used. In the atomic potential program, the electron-ion core interaction is described by a one-electron muffin-tin potential. To calculate the muffin-tin potential for atoms in a crystal lattice, according to the description of Matheiss<sup>49,50</sup>, we started with the atomic wavefunctions<sup>51</sup> and then included a correction for ionic materials (i.e.,  $\text{Ga}^+\text{P}^-$ ) by a madelung type summation in real and reciprocal space. Slater exchange<sup>52</sup> was used for the contribution of exchange interaction. The muffin-tin radii of  $\text{Ga}^+$  and  $\text{P}^-$  were chosen to be  $1.182\text{\AA}$ . This is the half of the nearest-neighbor distance of GaP. The phase shifts are then obtained by radial integration<sup>50</sup> of the Schrodinger equation for the separated atomic potential. The first five phase shifts ( $l=0,1-4$ ) were used in the dynamical LEED intensity calculations through Eq. (2.1-36). The electron-electron interaction was incorporated via a complex "optical potential". The inner potential (Vor) was taken to be 8 eV. The inelastic damping factor (imaginary potential) was set equal to 5 eV.

The consequence of the thermal lattice vibrations (electron-phonon interaction) was included in the LEED intensity calculations by correlating the input phase shifts with the temperature dependent phase shifts through Eq. (2.1-57). A Debye temperature of 319K was used for GaP. Experimental LEED intensities were very insensitive to the temperature factor. Both room temperature and low temperature (95K) LEED intensity curves of the GaP (110) face were recorded and essentially identical. This indicates that the approximate Debye model will not attribute any error to the determination of the GaP (110) surface structure.

#### 4.4 Surface Structure of GaP (110) Face

The arrangement of the surface atoms on the ideal GaP (110) surface in the direct lattice is the same as that of GaAs except that the As atoms are replaced by P atoms. The dimensions of the surface unit mesh,  $a=3.864\text{\AA}$  and  $b=5.4505\text{\AA}$ <sup>54</sup> as shown in Fig. 4.2 (b), are very close to those of GaAs. Since the GaP crystal is quantitatively similar to GaAs with respect to its crystal structure and chemical properties, it is reasonable to assume that the GaP (110) face has the same surface reconstruction as that of the GaAs (110) face. No fractional order spots were observed as shown in Fig. 4.2 (d) and the ratio of the dimensions of the surface unit mesh is 1.41. Agreement with the ideal bulk value of 1.414 is within 1% which suggests that the surface unit mesh is undistorted with respect to that in the bulk unit cell. The twofold symmetry along the b axis (Fig.4.1(b)) in the direct lattice of the (110) face is directly observed through the symmetry of the intensity profiles of the  $(\pm h, k)$  beams. This suggests that a relative horizontal displacement of the group III and the group V atoms in the surface layer is unlikely. The intensities of the (1,0) and  $(\bar{1}, 0)$  beams are expected to be extremely weak when they are diffracted from a bulk structure because the  $(\pm 1, 0)$  beams are "quasi-forbidden beams"<sup>32</sup>. This can be explained by the formula for the scattering amplitude:<sup>55</sup>

$$F_{hk} = \sum_{j\alpha} f_j^\alpha(\lambda, \theta) \exp(2\pi i(hx_{ij}^\alpha + ky_{ij}^\alpha + (1+\cos\theta_{hk})z_j/\lambda)) \quad (4.1)$$

AD-A126 445

THE SURFACE STRUCTURE SCATTERING LOSSES AND SCHOTTKY  
BARRIER MODEL OF III. (U) RUTGERS - THE STATE UNIV  
PISCATAWAY NJ DEPT OF ELECTRICAL ENG. B W LEE  
21 DEC 82 AFOSR-TR-83-0032 AFOSR-79-0136 F/G 20/5

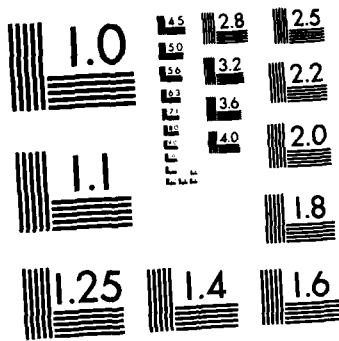
2/2

UNCLASSIFIED

NL

END

FILED  
11 11  
0707



MICROCOPY RESOLUTION TEST CHART  
NATIONAL BUREAU OF STANDARDS-1963-A

where  $f_j^\alpha$  is the atomic form factor of the atom in the  $j$ 'th layer,  $x_{ij}^\alpha$  and  $y_{ij}^\alpha$  are the coordinates of the  $i$ 'th atom in the  $j$ 'th layer,  $z_j$  is the distance from the surface to the  $j$ 'th layer,  $\theta_{hk}$  denotes the scattered angle of  $(h,k)$  beam and  $\lambda$  is the incident electron wave length. For the  $(1,0)$  and  $(\bar{1},0)$  beams of GaP (110),  $h=\pm 1$ ,  $k=0$  and  $z=id$ . The summation in Eq. (4.1) then gives:<sup>45</sup>

$$F_{\pm 1,0} = (f^{\text{Ga}} - f^{\text{P}}) / (1 - \exp(i + \cos \theta_{hk}) 2\pi id / \lambda) \quad \text{-----} (4.2)$$

Equation (4.2) shows that scattering from rows of Ga and rows of P atoms is out of phase and should cancel. Since the form factor of Ga and P ( $f^{\text{Ga}}$  and  $f^{\text{P}}$ ) should be similar, Eq. (4.2) predicts that the intensities of the  $(1,0)$  and  $(\bar{1},0)$  beams should be weak if there is no displacement in the position of the atoms on the (110) face. The observed intensities of  $(\pm 1,0)$  beams are very strong as shown in the experimental LEED patterns (Fig. 4.2(d)), and in the intensity profiles (Fig. 4.3). The discrepancy between theoretical and experimental results suggests that there is a rearrangement in the positions of the atoms on the (110) surface. The observed unreconstructed LEED patterns and the excellent symmetry of the  $(\pm h,k)$  beams rules out the possibility of surface unit mesh reconstruction and the horizontal displacement of Ga and P atoms with respect to each other. A vertical contraction of the top surface layer or a vertical displacement of Ga and P atoms with respect to each other, which will leave the surface unit mesh unchanged, is the only remaining possibility for surface rearrangement. All of the experimental results obtained from the GaP (110) face are similar to those obtained from the GaAs

(110) face<sup>31-34,45</sup>.

Based on the information of GaAs (110) face<sup>31,32,45</sup>, we assumed the bond-rotation model<sup>31</sup> with  $w=27^\circ$  (Fig. 4.1(a)) was the best candidate for surface atomic geometry of the GaP (110) face. This assumption turned out to be incorrect, as will be shown later. In the study, other possible surface structures analyzed in detail include (a) pure bond-rotation with  $w=20^\circ, 27^\circ$ , and  $34.8^\circ$ , (b) pure top layer spacing contraction,  $\Delta d$ , and (c) a bond-rotation,  $w$ , with a top layer spacing contraction,  $\Delta d$ . A total number of 17 conceivable surface structures were analyzed in detail. These structures are summarized in Table 4.1.

I-V curves obtained for the first 16 inequivalent nonspecular beams emerging from the sample were compared with the theoretical curves calculated from the 17 different structures as listed in Table 4.1. Most of the 17 proposed structures yielded very poor results when we compared the theoretical curves with the experimental curves. Therefore, these proposed structures could not be considered as the real surface structure. Only 3 out of 17 structures provided relatively good agreement with the experimental curves, and these structure models were (a) a bond-rotation angle,  $w=27^\circ$ , with a 5% top surface layer spacing contraction,  $d=-0.097\text{\AA}$ , (b) a pure bond-rotation angle,  $w=27^\circ$ , plus  $\Delta d=0$ , and (c) a pure  $0.097\text{\AA}$  contraction of top layer spacing with  $w=0$ . These theoretical curves and experimental curves are compared as shown in Figs. 4.3 to 4.6 for the (0,1),  $(\bar{1},0)$ ,  $(0,\bar{1})$  and (1,1) beams respectively for the first-order beams. The comparison between the recorded and calculated curves for the

high-order beams such as (0,2), (1,2) and (2,1) beams are similar to the first-order beams. Obviously, the curves (c) in Figs. 4.3 to 4.6 are not in good agreement with the experimental curves. Thus, the model of a pure 5% top layer spacing contraction could not be considered for real surface structure. Both curves (a) and (b) are only in fair agreement with the experimental curves. From the peak positions and the line shape of the  $(\bar{1},0)$  beam in Fig. 4.4, the  $(0,\bar{1})$  beam in Fig. 4.5, and the (1,1) beam in Fig. 4.6, model (a) is favored rather than model (b) as the real surface atomic structure of GaP (110) face.

The generally satisfactory agreement of most of the 16 beams in magnitude, peak positions, and line shape between the recorded and calculated curves of model (a) led to the conclusion that P atoms are rotated outward from the GaP (110) plane and Ga atoms are rotated inward from this plane by an angle of  $27^\circ$ . Furthermore, the surface layer is compressed by 5% such that the top layer spacing is reduced by approximately  $0.1\text{\AA}$ .

No quantitative analysis of the GaP (111) surface atomic structure has been reported. A  $1\times 1$  LEED pattern was observed by Miyao, et al,<sup>42</sup> and then a  $2\times 2$  reconstruction pattern was reported by Van Bommel and Crombeen<sup>43</sup>. In our study, a clear  $1\times 1$  threefold LEED pattern of GaP (111) was first observed in a UHV chamber with background pressure of  $1\times 10^{-9}$  torr as shown in Fig. 4.7, and a  $2\times 2$  reconstruction pattern was then obtained in a better background pressure of  $4\times 10^{-10}$  torr. The extra ( $2\times 2$ ) reconstructed beams were

weak and disappeared within hours after the sputtering and annealing. Further study of this phenomenon is needed. The dynamical calculation and analysis is in progress, but complete results will not be reported here.

One interesting experimental result is worth mentioning. A LEED pattern indicating diffraction from facets was observed on the GaP (111) face after annealing the crystal to 600°C. The facet structure has been reported previously and it was concluded that the facet pattern is due to reflections from three equivalent (110) planes<sup>56</sup>. The facet spots faded away after heating to 650°C and spots of the fundamental  $1 \times 1$  pattern brightened. The same results were reported by Miyao, et al.<sup>41</sup>. No explanation of these results was offered by them. We attempt to explain this phenomenon as follows. A large amount of P atoms start to evaporate from the (111) face and leave an almost pure Ga layer on the surface when the sample is heated to 650°C. At this temperature, the Ga layer is a melted metallic layer and crystallizes along the GaP (111) structure during the crystal cooling period. An epitaxial Ga layer is thus grown on GaP (111) surface. The ratio of the Ga/P Auger peak increase from 0.9 to 5.05 after heating to 650°C which gives the support to our explanation. This interesting result indicates that it should be relatively easy to obtain a good Schottky contact on the GaP (111) face.

Table 4.1 Surface structure for GaP (110) face.

$\Delta d$  is the percentage of the top layer spacing contraction and  $w$  is the bond rotation angle with the Ga species rotated inward and P species outward.

$\Delta d(\%) =$ with $w = 0$	2.5	5	6	7.5	10
$w =$ with $\Delta d=0$	20°		27°		34.8°
$\Delta d(\%) =$ with $w =$	2.5	5	7.5		
	20° , 27° , 34.8°	20° , 27° , 34.8°	20° , 27° , 34.8°		

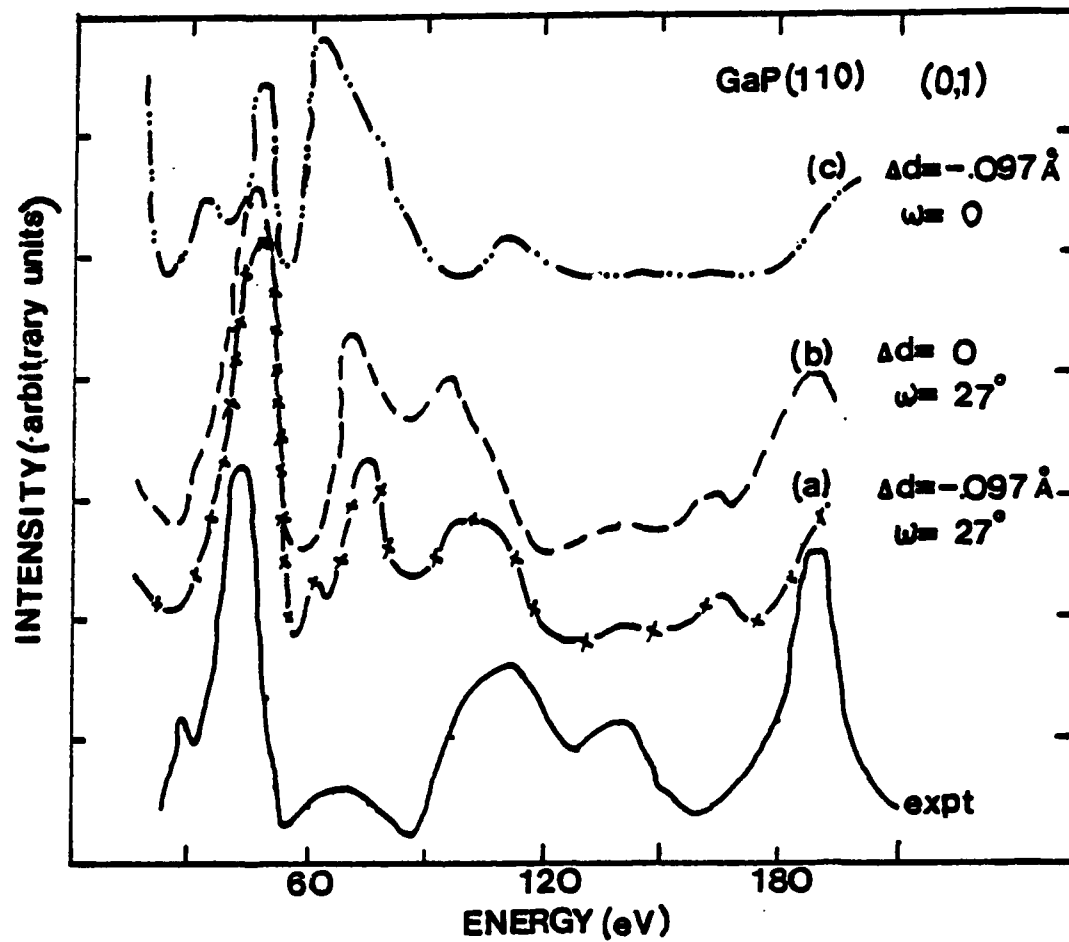


Fig. 4.3

(0,1) beam LEED intensity profile of GaP (110). Solid trace is the experimental curve. Curves (a), (b), (c) are the theoretical calculation with different  $\Delta d$  and  $w$ .

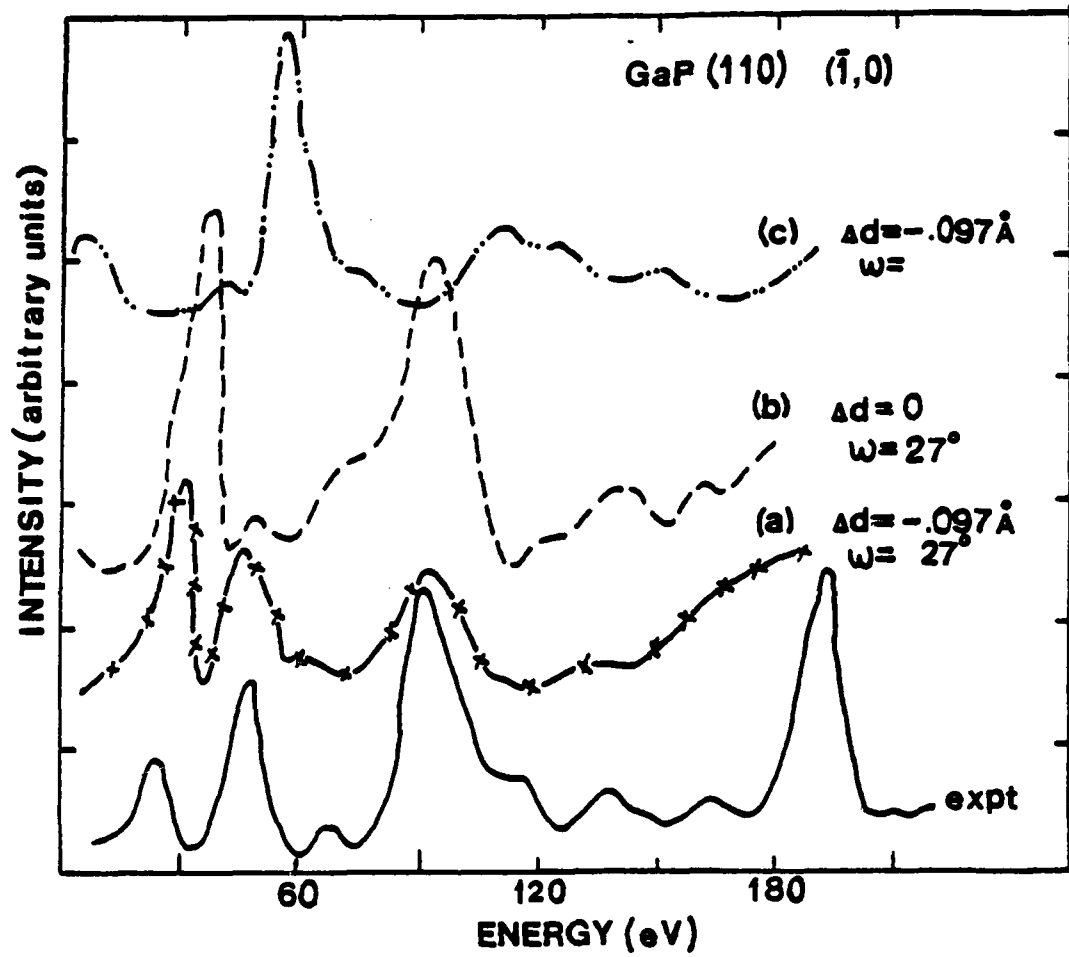


Fig. 4.4

$(\bar{1},0)$  beam LEED intensity profile of GaP (110). Solid trace is the experimental curve. Curves (a), (b), (c) are the theoretical calculations with different  $\Delta d$  and  $w$ .

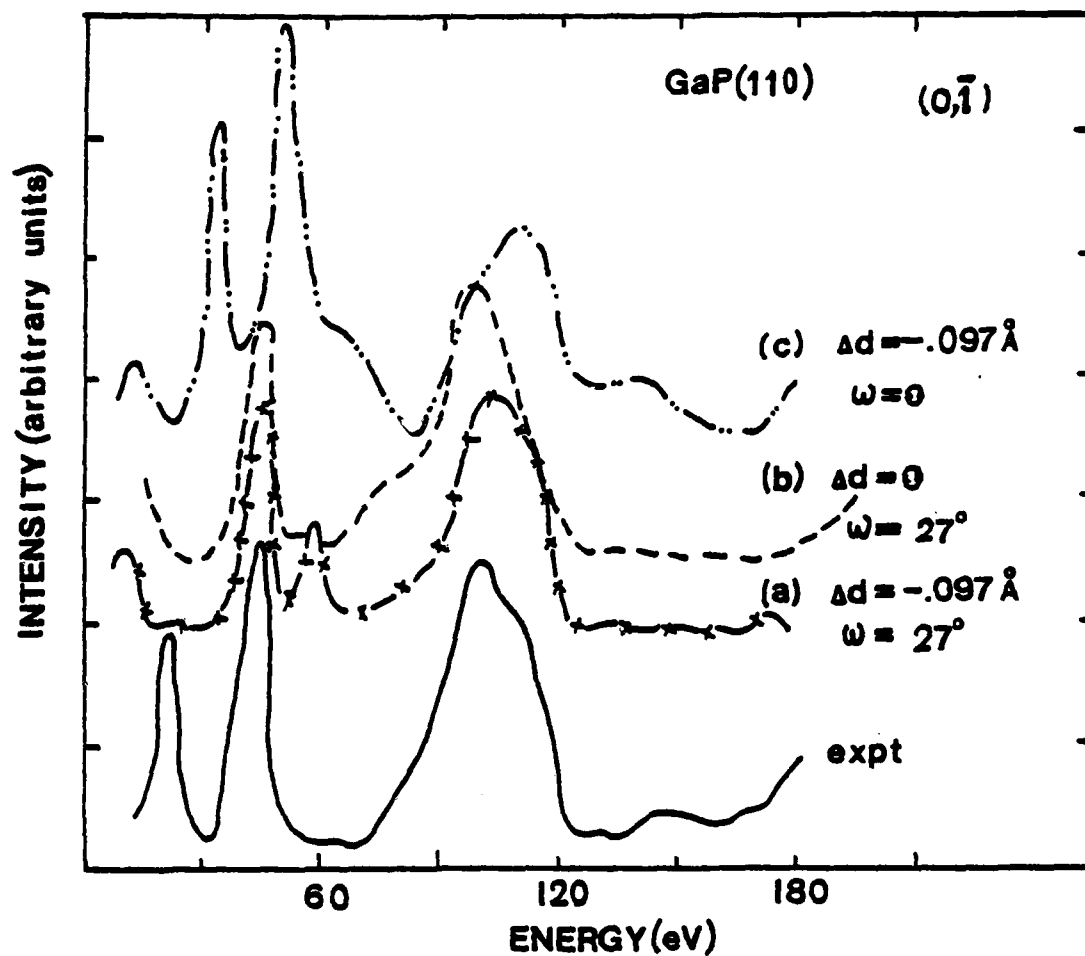


Fig. 4.5

$(0, \bar{1})$  beam LEED intensity profile of GaP (110). Solid trace is the experimental curve. Curves (a), (b), (c) are the theoretical calculations with different  $\Delta d$  and  $\omega$ .

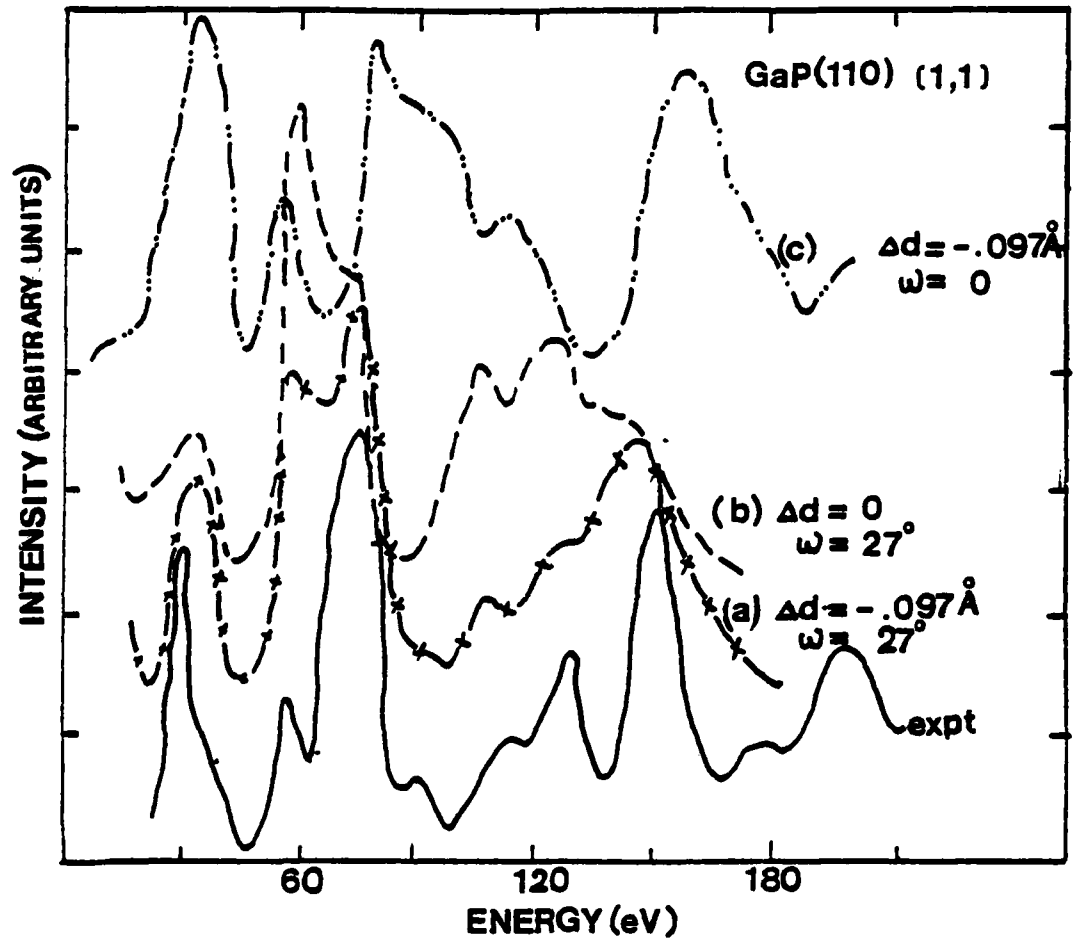


Fig. 4.6

(1,1) beam LEED intensity profile of GaP (110). Solid trace is the experimental curve. Curves (a), (b), (c) are the theoretical calculations with different  $\Delta d$  and  $w$ .

#### 4.5 Discussion and Conclusion

The LEED pattern of the GaP (110) face starts to fade away after very few hours in a  $1 \times 10^{-9}$  torr UHV chamber while the GaAs (110) LEED pattern can stay sharp for days in the same vacuum environment. In both cases, no reconstruction LEED spots were observed during the period that they remained in the chamber. This implies that the chemisorption of the residual gas molecules on both the GaP (110) and the GaAs (110) faces is a random process. An oxygen Auger peak was detected on the former after the sample remained in the chamber for hours, while it took days for the latter to pick up any detectable amount of oxygen in the same vacuum environment. These indicate that the GaP (110) face is more reactive and less stable than the GaAs (110) face.

No attempt has been made to investigate the efficiency of the Zanazzi and Jona r factors<sup>57</sup> as a quantitative guide to the trend in the theoretical intensities. It is very useful to use r factors in refining and quantifying an already good theory-experiment comparison. It is less useful to use these r factors for the first qualitative model selection. More extensive data and analysis including r factors could lead to further refinements of the structure model. In a recent report by C. B. Duke, et al.<sup>58</sup>, they utilized r factors to assess the analysis. The resulting best-fit structures consist of single layer reconstruction characterized by a bond-rotation angle of  $w=25^{\circ} \pm 3^{\circ}$  and a  $0.1 \pm 0.05$  Å<sup>0</sup> contraction of the topmost layer spacing which is similar to our proposed model. Our result turns out to be a good

first approximation.

In conclusion, our LEED study has indicated that the atomic structure of the GaP (110) face is quite similar to that of GaAs (110) regarding the rippled geometry. On both the GaP (110) and GaAs (110) surfaces, the group V atoms are rotated outward from the surface plane and Ga atoms are rotated inward from this plane by an angle of  $27^\circ$  in order to preserve the bond lengths between the nearest-neighbor. The topmost layer spacing of the GaP (110) face is reduced by  $0.1\text{\AA}$ . The stability study of LEED patterns concludes that the GaP (110) face is less stable than the GaAs (110) face. The complete surface structure analysis of the GaP (111) face is premature and needs further study. It is suggested that a good Schottky contact should be relatively easy to grow on the GaP (111) face.

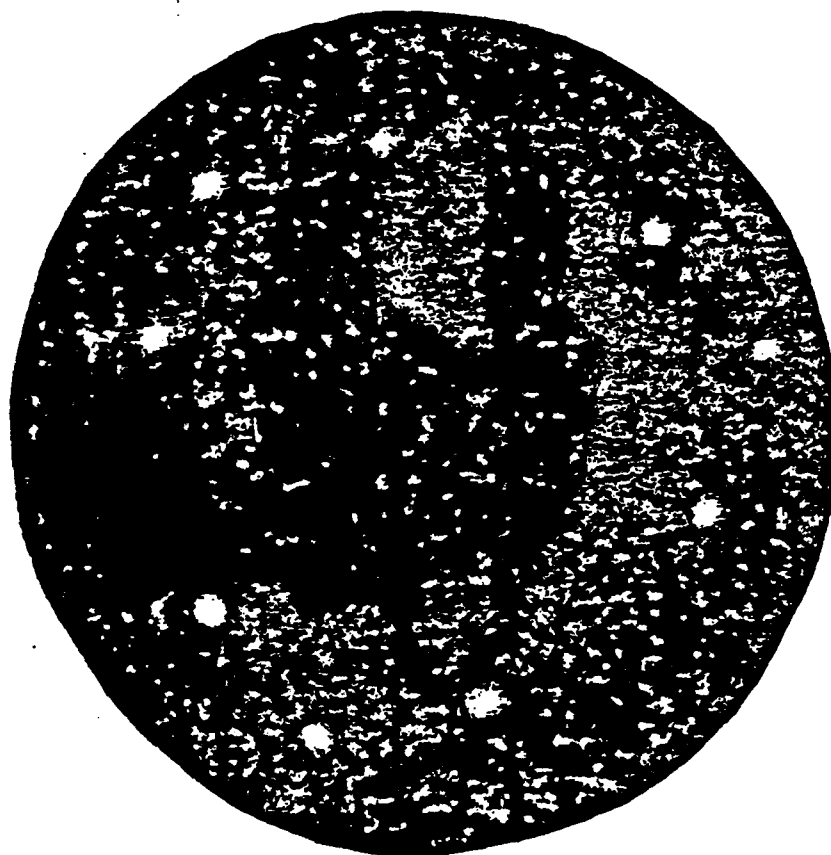


Fig. 4.7 Room temperature LEED pattern of GaP (111) face taken at 146 V.

## CHAPTER 5

## STRUCTURE MODEL OF III-V COMPOUND SEMICONDUCTOR SCHOTTKY BARRIERS

## 5.1 Introduction

Many investigations have been done on metal-semiconductor interfaces, and numerous theoretical approaches have been used to explain the basic physical mechanism for the metal-semiconductor interaction and formation of the Schottky barriers<sup>59-71</sup>. Modern surface analytical techniques have been applied to characterize the metal-semiconductor interfaces and the results<sup>66-69</sup> strongly suggest that the physical structure of a real Schottky barrier is more complicated than that of a perfect planar junction between the metal and semiconductor. Defects at or near the surface of the semiconductor are the important mechanism in determining the barrier height and metal-semiconductor interaction. In many cases, this can dominate the electrical properties of Schottky barrier. Interface compound formation and the metal-induced surface states are observed<sup>66</sup> at the representative metal-semiconductor interfaces and it is concluded that local charge redistribution rather than any intrinsic surface states of the semiconductor determine Schottky barrier formation at these interfaces. The "defect" model<sup>68,69</sup> and the "unified" model<sup>70,71</sup> of all Schottky barriers have been proposed to explain the Fermi-level pinning and other phenomena of a real Schottky barrier. Although the Schottky diode has important applications in practical devices, and the formation of Schottky barriers has been studied for the past

several decades, both the physical and electrical properties of this device are not completely understood.

In this chapter, a macroscopic structural model<sup>72</sup> of the real Schottky barrier is suggested. Based on the structural model, an electrical equivalent model is derived to describe the fundamental behaviors of a real Schottky diode, including the origin of the Fermi-level pinning, the barrier heights, and the deviation of the diode factor from its ideal value.

As suggested at the conclusion of Chapter 4, the GaP (111) face was chosen to be the semiconductor surface for Schottky barrier studies. Schottky barriers were fabricated by evaporating metal on a GaP (111) face to demonstrate the structural model. Capacitance-voltage (C-V), capacitance-frequency (C-f), current-voltage (I-V) and conductance-frequency (G-f) measurements were then performed to analyze the electrical properties of the diodes. Auger electron spectroscopy (AES) studies were used to correlate the chemical composition of the metal-semiconductor interface to the structure.

## 5.2 Structural Model

Metal-induced surface states and interface compound formation at metal-semiconductor interfaces were observed<sup>66</sup>. These phenomena were associated with microscopic dipoles at the intimate contacts which accounted for the macroscopic Schottky barrier heights. Modern surface analytical techniques have been applied to study the metal-semiconductor interfaces and the results<sup>66-69,73</sup> showed a strong diffusion and inter-atomic diffusion between the metal and semiconductor. It was suggested<sup>73</sup> that the driving force for dissolution of the III-V compound and its movement into the metal is the heat of condensation of the metal on the surface of semiconductor. The energy transferred from the metal atoms during the condensation must be dissipated by the semiconductor. If this energy is comparable to or considerably larger than the heat of formation of the semiconductor, the momentarily excited atoms at the semiconductor surface will gain enough energy to break their bonds and move into the metal. This atomic interdiffusion process could create a thin amorphous layer which is comprised of the metal and semiconductor atoms between the metal and semiconductor. A detailed discussion of the condensation mechanism can be found in the literature<sup>69</sup>.

Strong interdiffusion of the metal and semiconductor atoms was observed in the AES studies of Au-GaP and Al-GaP Schottky barriers. Based on the experimental results, a metal-amorphous film-semiconductor (MAS) structure as shown in Fig. 5.1 (a) is suggested to be the physical structural model of a real Schottky barrier. The thick-

ness of the amorphous film,  $W$ , is in the range of  $50\text{\AA}$  to  $500\text{\AA}$  depending upon fabrication details, and the amorphous film is a random mixture of metal and semiconductor atoms. The a.c. equivalent circuit of the physical structural model under reverse bias is shown in Fig. 5.1 (b).  $C_A$  and  $R_A$  are the capacitance and the resistance of the amorphous layer, respectively,  $C_D$  is the depletion capacitance of the semiconductor, and  $R_S$  is the series resistance of Schottky diode. The d.c. equivalent circuit of the model under forward bias is shown in Fig. 5.1 (c). At low current injection, the I-V characteristics of an amorphous semiconductor is a hyperbolic sine function. At high current injection, the hyperbolic function can be approximated as;

$$I = I_{0A} \exp(V_A / n_A V_T) \quad (5.1)$$

where  $V_T = kT/q$

where  $I_{0A}$  is a constant,  $V_A$  is the applied voltage across the amorphous film,  $k$  is Boltzmann's constant,  $T$  is the temperature in degrees Kelvin,  $q$  is the magnitude of electron charge, and  $n_A$  is a parameter characterizing the properties of the film, including its thickness.

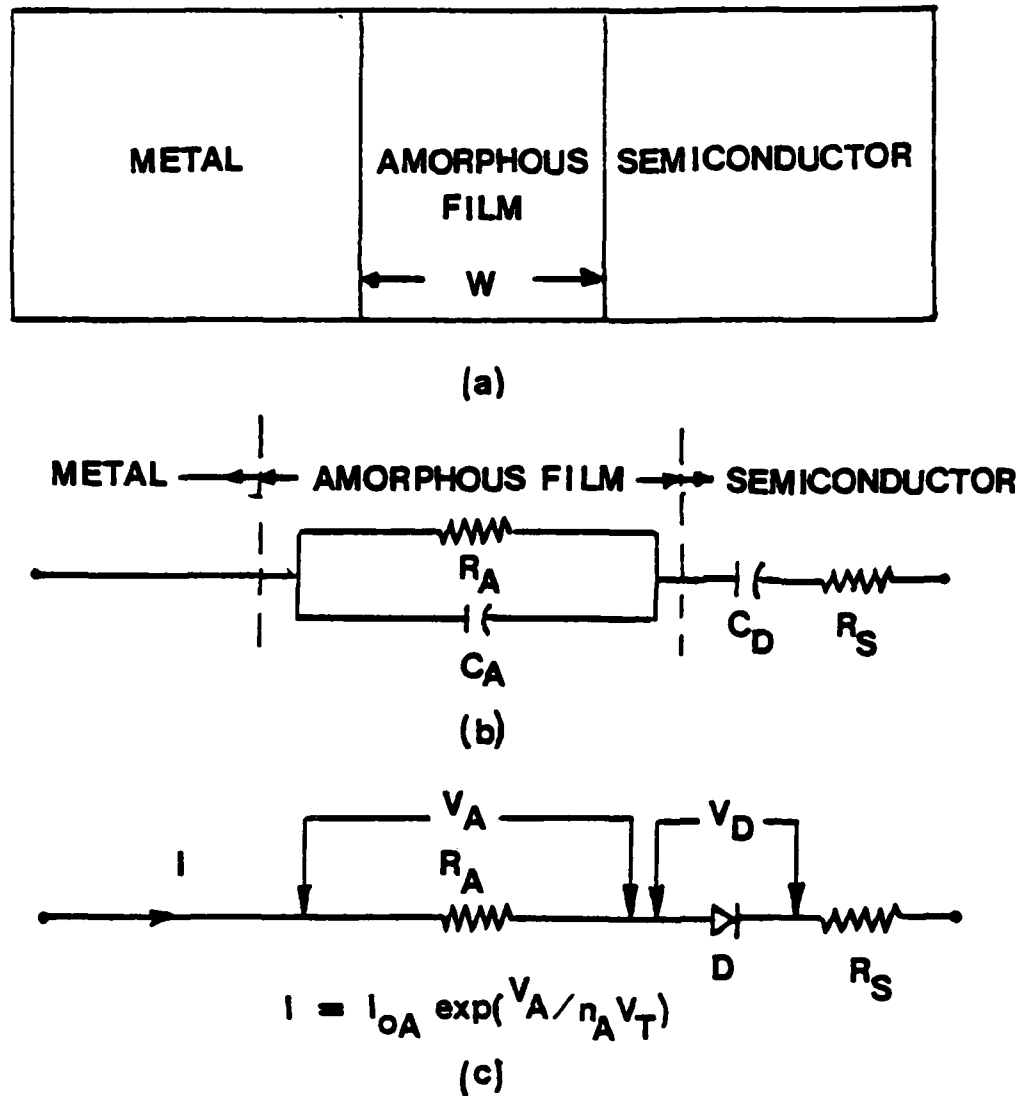


Fig. 5.1

- (a) is the structural model of a real Schottky diode.  
 (b) is the a.c. equivalent circuit of the real Schottky diode under reverse bias.  
 (c) is the d.c. equivalent circuit of (a) under forward bias.

### 5.3 Outline of Experiments

Schottky diodes described in this chapter were prepared on single-crystal n-type GaP (111) faces doped with Te ( $N_D = 3 \times 10^{17}$ ). The GaP crystals were 1 in.-diameter by 0.03 in.-thick wafers, and polished on both (111) and ( $\bar{1}\bar{1}\bar{1}$ ) faces. Eight samples were cut from the same wafer. Low energy electron diffraction (LEED) studies were conducted on the samples before device fabrication to ensure that ohmic contacts were deposited on ( $\bar{1}\bar{1}\bar{1}$ ) face. Ohmic contacts were attached first by alloying  $Au_{.98}Si_{.02}$  to the ( $\bar{1}\bar{1}\bar{1}$ ) face of the crystal. The alloying was done at  $600^\circ\text{C}$  in a nitrogen gas atmosphere for three minutes. Low contact resistances, ( $<1\Omega$ ), were obtained in most of the diodes.

Prior to the evaporation of rectifying contacts, the surface of each sample was etched in a solution of  $H_2SO_4:H_2O_2:D.I.-water$  (3:1:1). The ohmic contacts were protected with Apiezon wax during this process. After removing the Apiezon wax with trichloroethylene and rinsing in acetone, methanol and then D.I.-water, the substrates were blown dry with nitrogen, and then placed in the vac-ion vacuum system immediately.

Rectifying contacts were deposited on the GaP (111) face by a vacuum evaporation of Al or Au from resistance sources with a background pressure in the low  $10^{-8}$  torr range. The temperature of the samples was retained at  $250^\circ\text{C}$  throughout the evaporation. This elevated substrate temperature reduced the possibility of interlayer formation between the metal and semiconductor due to surface contam-

ination. The evaporation sources were covered by a shutter during the cleaning preheating period, and the shutter was opened to allow for a metal deposition. A deposition period of 10 seconds was used for all the samples except for sample No. 3, which had a considerably longer evaporation time. A much thicker amorphous interlayer was obtained in sample No. 3 due to the prolonged evaporation cycle, as will be noted later in the AES profile.

The geometries of the rectifying contacts were controlled by 0.05 inch thick molybdenum masks, and circular contacts, 0.03 inch in diameter, were used for C-V, I-V, and AES measurements.

A series of C-V, C-f, G-f and I-V measurements as described in section 3.4 were carried out for at least three diodes on each sample, after the sample had been removed from the evaporation station. All the measurements were performed in a shielded box. For the reverse biased C-V, C-f and G-f measurements, a lock-in amplifier was used. C-f and G-f measurements were carried out at zero bias for different frequencies. For the forward bias I-V measurement, an electrometer and a digital multimeter were used. The chemical depth profiles were obtained by using AES and ion milling in an UHV chamber after the electrical measurements.

#### 5.4 Results and Discussion

The I-V characteristics curves for samples No. 3 through No. 6 and sample No. 8 were plotted in Fig. 5.2. The diode factors  $n$  were derived from the extrapolation of the linear region of these curves and are listed in Table 5.1. Significant deviation of the diode factor  $n$  from its ideal value of unity is observed on all samples, which indicates that the current transport between Schottky barriers is not purely thermionic. This deviation can be attributed to the existence of the amorphous film in the diode, which behaves as a nonlinear resistor at high current injection as modeled in Fig. 5.1 (c). A more detailed characterization of this film at forward bias will be discussed later. The series resistance of the diodes were obtained from the I-V curves at large forward bias. The diode capacitance per unit area,  $C$ , was obtained from measurements of the capacitance, conductance and diode series resistance.  $1/C^2$  vs.  $V$  curves remained linear for a large region of bias voltages as shown in Fig. 5.3 for five different samples. The values of carrier concentration were calculated from the slope of  $1/C^2$  vs.  $V$  in the reverse bias region. The Schottky barrier heights,  $\phi_{bn}$ , of all samples were obtained from both C-V and I-V measurements. These values of  $\phi_{bn}$  are listed in Table 5.1.

From Table 5.1, we noted that the barrier heights  $\phi_{bn}$  obtained by I-V measurements are generally consistent and agree with data obtained by others<sup>74</sup>. The barrier heights obtained by C-V measurements, however, are always much larger than those deduced from I-V methods,

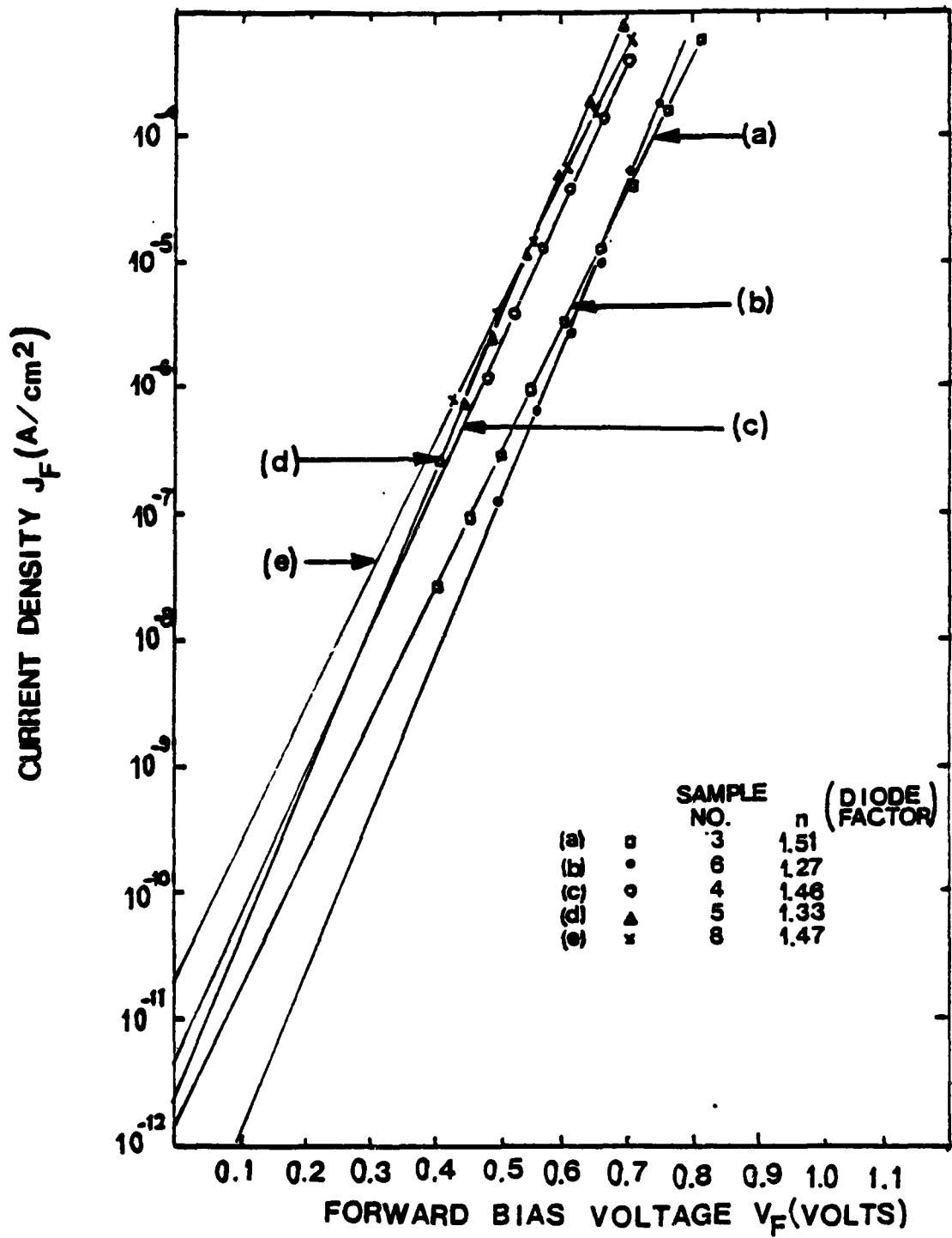


Fig. 5.2

I-V curves of GaP (111) Schottky diodes with various metal films.

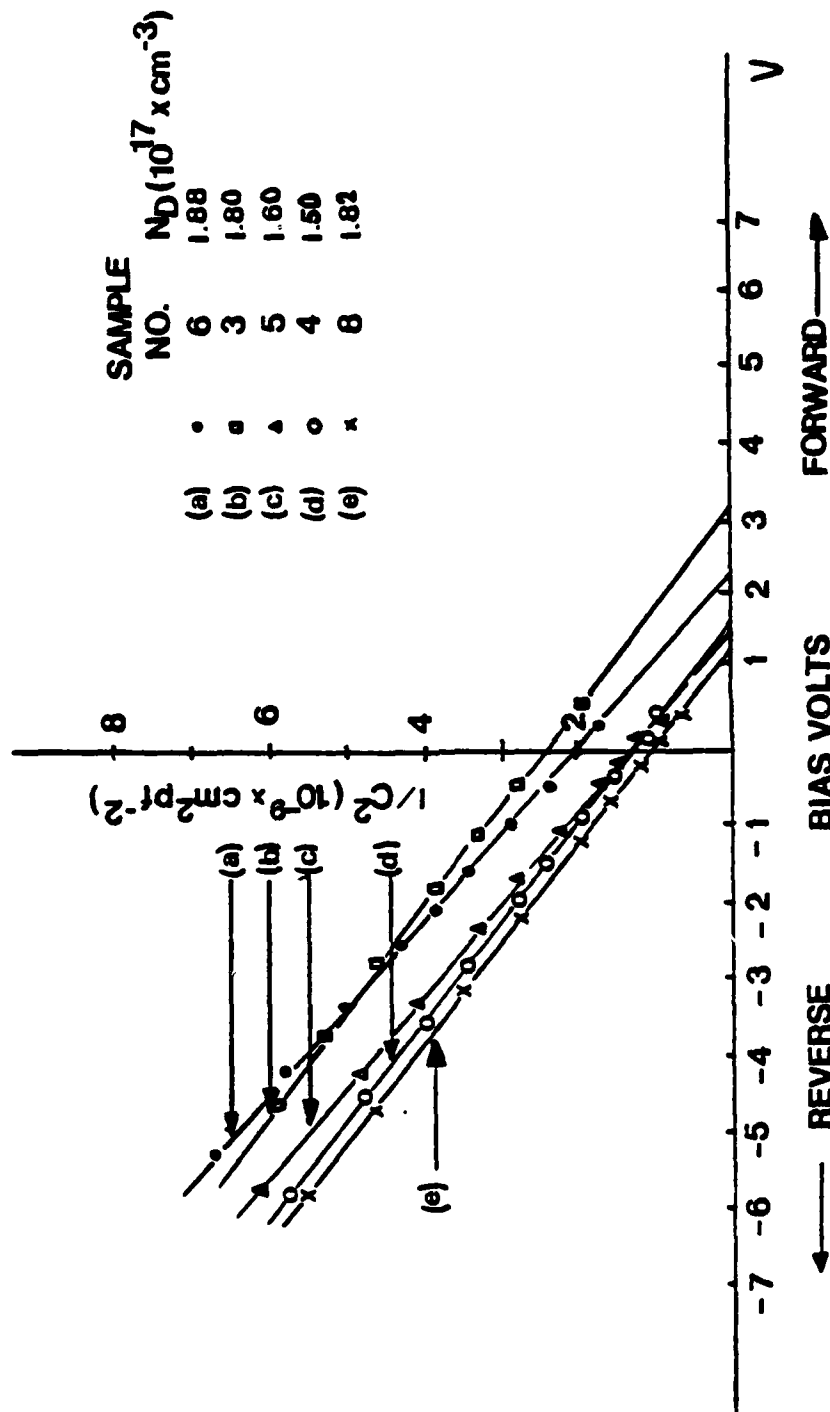


Fig. 5.3  $1/C^2$ -V curves of GaP (111) Schottky diodes with various metal films. Barrier heights and doping concentration of the diodes obtained from the curves are listed in Table 5.1.

Table 5.1 Results of C-V and I-V measurements.

$\phi_{bn}$  - the barrier height,  $N_D$  - the donor concentration,  $n$  - the diode factor.  $N_D$  was obtained by C-V measurement and  $n$  by I-V measurement.  $\phi_{bn}$  was measured by C-V and I-V methods and are listed accordingly.

Sample Number	Metal	C-V		I-V	
		$\phi_{bn}$ (eV)	$N_D$ (cm <sup>-3</sup> )	$\phi_{bn}$ (eV)	$n$
2	Al(Si)	1.26		1.04	
3	Al(Ni)	3.10	$1.88 \times 10^{17}$	1.13	1.51
4	Al	1.52	$1.80 \times 10^{17}$	1.10	1.46
5	Al(Au)	1.36	$1.6 \times 10^{17}$	1.11	1.33
6	Au	2.35	$1.5 \times 10^{17}$	1.24	1.27
8	Al(Cu)	1.26	$1.82 \times 10^{17}$	1.10	1.47

and this is consistent with the results generally reported<sup>67,74,75</sup>. In some cases, the barrier heights measured by the C-V method were larger than the energy bandgap of GaP, (see Table 5.1), where the barrier heights of sample Nos. 3 and 6 are 3.1eV and 2.35eV, respectively. This behavior was also observed and reported by Amith, et al<sup>67</sup>. It was proposed that a thin native oxide or a contaminate interfacial layer existed between the metal and the semiconductor to explain this behavior. It did not, however, explain the behavior observed<sup>60</sup> in diodes fabricated on newly cleaved surfaces in an UHV chamber, where the contamination or oxidation of the semiconductor was eliminated. Brillson,<sup>66,76</sup> reported observing chemical reactions and charge redistribution at metal-semiconductor junctions, and the formation of reacted interlayers with frequency-dependent dielectric constants significantly different from their semiconductor counterparts, on Al-CdS and Al-CdSe diodes. Our studies indicated that the reacted interlayer revealed many characteristics of an amorphous semiconductor, and therefore, a metal-amorphous film-semiconductor structural model is suggested. Our experimental results obtained from real Schottky diodes tend to support this model completely, as will be described.

The AES depth-composition profiles of sample Nos. 3, 5, 6 and 8 are shown in Fig. 5.4 through 5.7, respectively. In all cases, no detectable amount of contaminants were shown at the metal-semiconductor interfaces. This result, however, cannot rule out the possibility of the existence of contamination one percent or less than one percent of a monolayer, which is below the limit of Auger

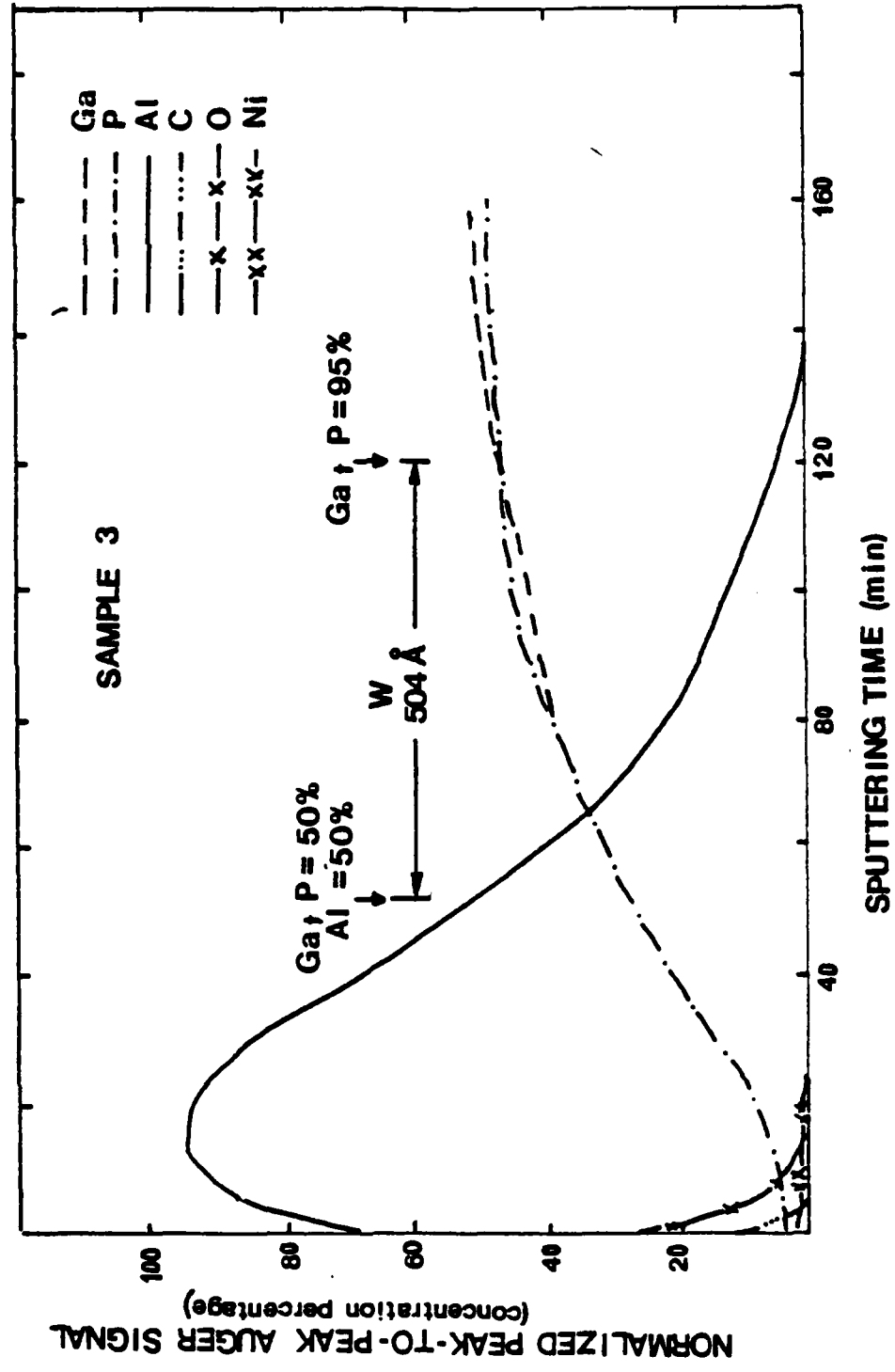


Fig. 5.4 AES depth - composition profile of sample No.3. Interdiffusion region was defined as the amorphous film (W).

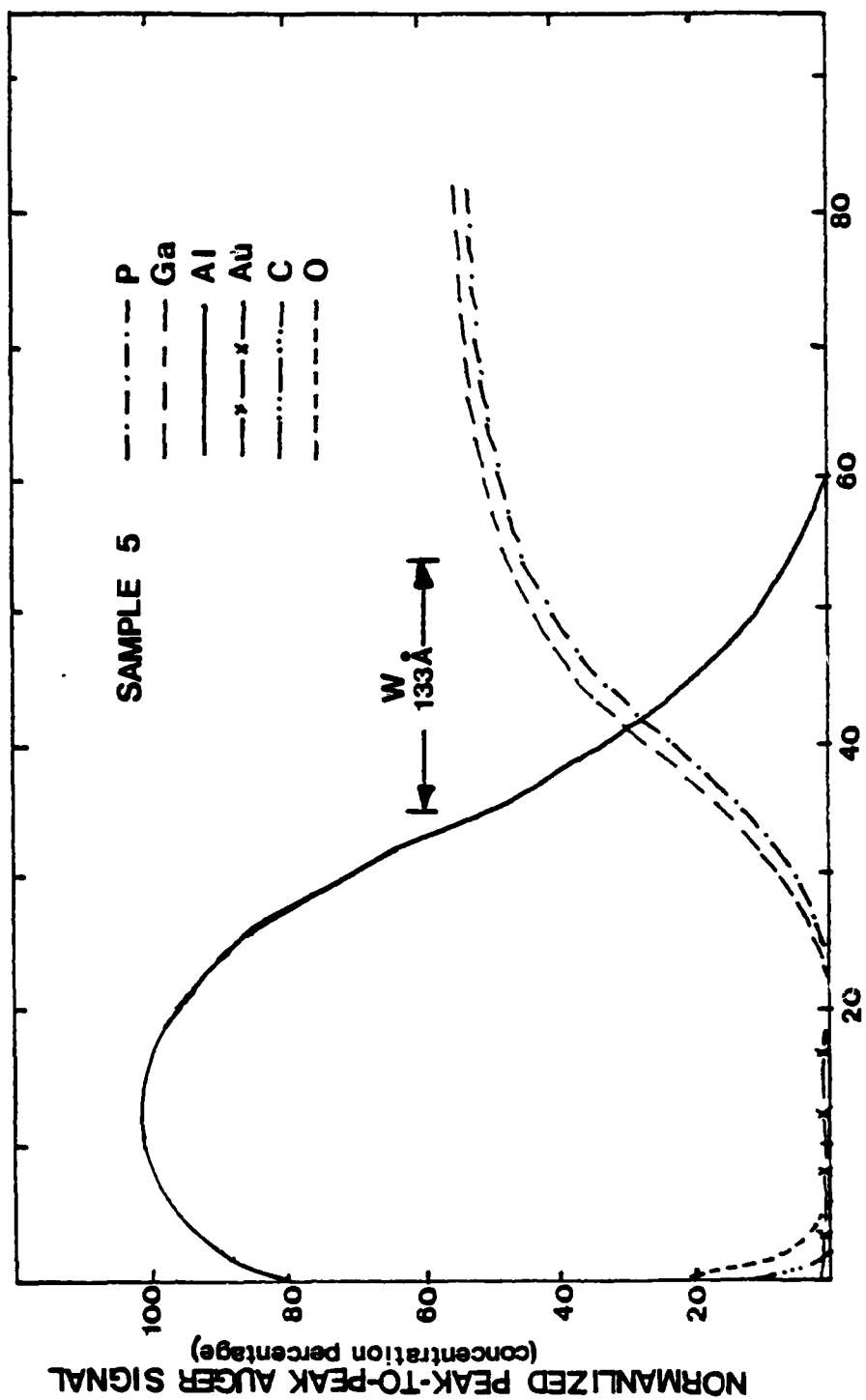


Fig. 5.5 AES depth - composition profile of sample No. 5. Interdiffusion region (W) was defined as the amorphous film.

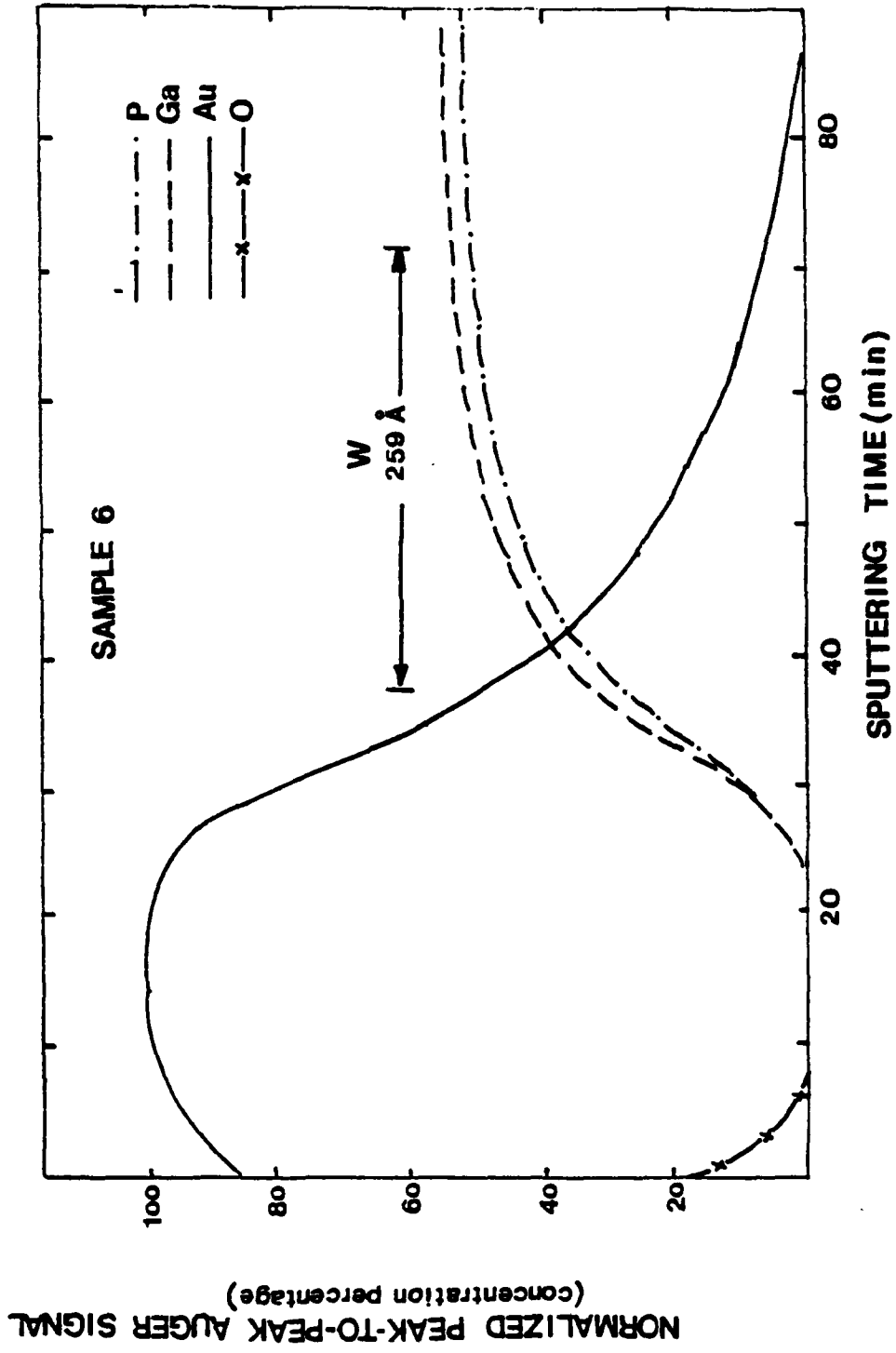


Fig. 5.6 AES depth - composition profile of sample No. 6.

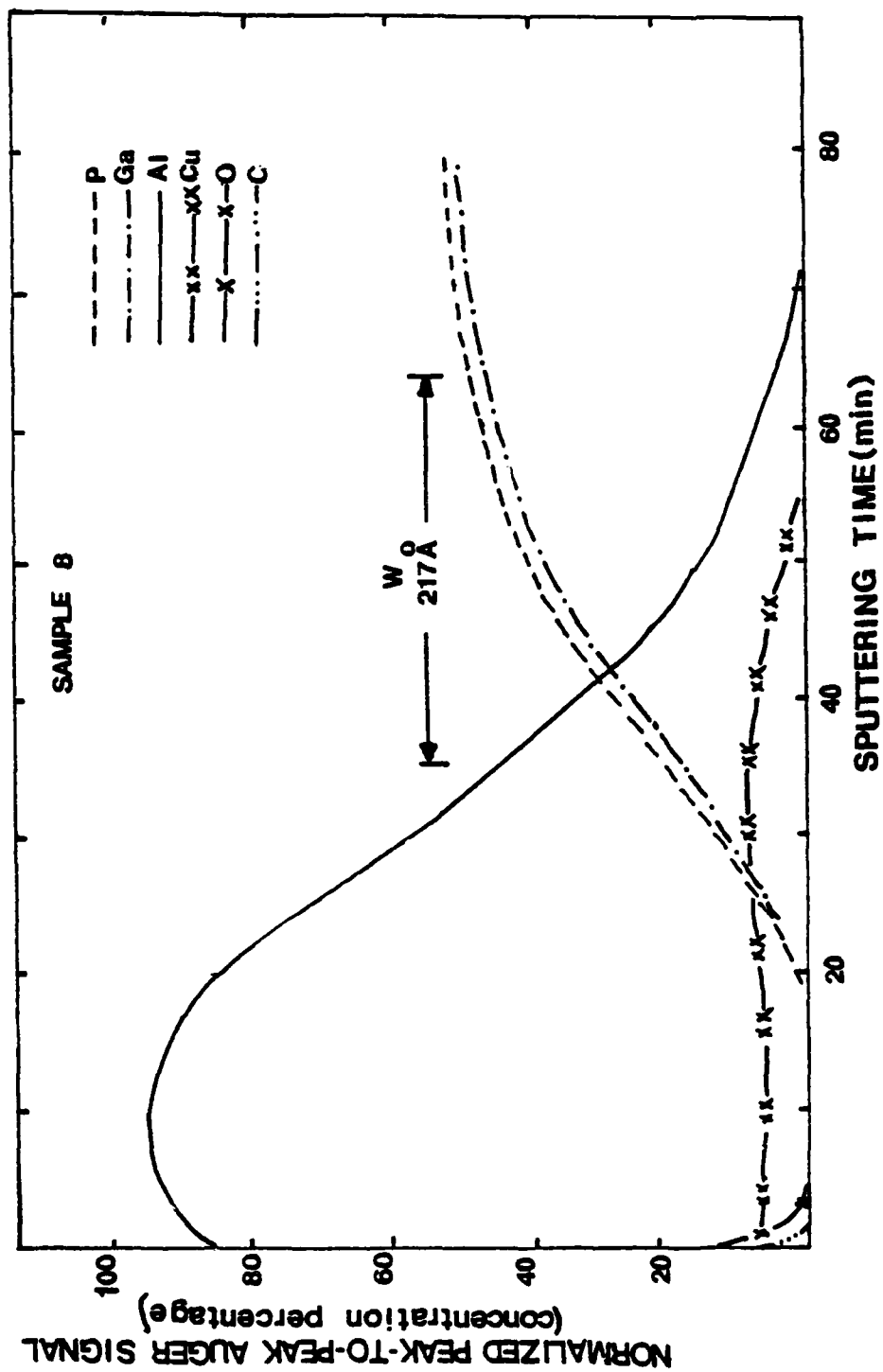


Fig. 5.7 AES depth - composition profile of sample No. 8.

signal detectability. Fermi-level pinning caused by such contamination is possible. An interlock system, which has the capability of fabricating Schottky diodes in an UHV chamber on a newly cleaved or ion-sputtering cleaned semiconductor surfaces to avoid such contamination, is currently underdeveloped. A small amount of oxygen and carbon contamination was detected at the surface region of the metal layer, but this should play no role in the diode performance. Strong atomic interdiffusion was observed for all samples. The interdiffusion region,  $W$ , the width of the amorphous film between the metal and semiconductor layers, is defined to start at the point where the concentrations of metal and semiconductor are both 50%, and to end at the point adjacent to the semiconductor where the concentration of semiconductor is 95%, as indicated in the AES profiles. It will be noted that  $W$  is not well defined, but since the amorphous film is a mixture of metal and semiconductor atoms, if the concentration of metal atoms is greater than 50%, metallic properties would be expected to dominate the characteristics of the mixture. The end point of the amorphous film is defined on the basis that a few atoms of metal condensed on the semiconductor could randomize the surface structure of the semiconductor and generate enough defect<sup>69</sup> states to pin the Fermi-level.

The ion sputtering rate,  $8\text{A}/\text{min}$ , was carefully calibrated on a known thickness. The sputtering rate and the interdiffusion width  $W$  were combined to experimentally estimate the thickness of the amorphous film in all the samples, and the resulting values of  $W$  are listed in Table 5.2.

The barrier heights,  $(\phi_{bn})$  obtained using the I-V method and the carrier concentrations  $(N_D)$  obtained by the C-V method, were used to calculate the depletion capacitance  $(C_D)$  of the semiconductor at zero bias. The total capacitance  $C_0$  and the total resistance  $R_0$  of the diode were obtained from C-f and G-f measurements, respectively. The  $C_D$  values were used together with  $C_0$  and  $R_0$  to calculate the capacitance  $C_A$  and the resistance  $R_A$  of the amorphous film utilizing the equivalent circuit of the diode under reverse bias shown in Fig. 5.1 (b). Values of  $C_A$  and  $R_A$  for all of the samples at 1 KHz are listed in Table 5.2. The dielectric constants  $\epsilon_r$  of the film for all the samples, listed in Table 5.2, were estimated by values of the capacitance  $C_A$  and the width  $W$ . The average value of the dielectric constant is  $7.23 \pm 0.31$ . It is clear that the dielectric constant of sample 5 as listed in Table 5.2 is much smaller than that of the other samples. This is probably due to the error introduced in estimating the film thickness of sample 5, and because of this uncertainty, the value of dielectric constant of sample 5 was not included in the calculation of the average dielectric constant for the amorphous film.

We found that both  $R_A$  and  $\epsilon_r$  are frequency-dependent. Figs. 5.8 and 5.9 show the  $R_A(f)$  and  $C_A(f)$  curves of various samples. The relation between the amorphous resistor  $R_A$  and frequency is given by  $f^{-m}$ . The values of  $m$  were calculated and indicated in Fig. 5.8. The frequency-dependent nature of  $R_A$  and  $\epsilon_r$  reveal the amorphous characteristics<sup>77</sup> of the interlayer. The exponent  $m$  has been derived<sup>77,78</sup> theoretically as

Table 5.2 Characteristics of the amorphous film found in the GaP (111) Schottky diodes.

$C_A$  = Low-frequency (1 KHz) capacitance of amorphous film at zero bias

$R_A$  = Low-frequency (1 KHz) resistance of amorphous film at zero bias

$W$  = Thickness of amorphous film

$\epsilon_r$  = Dielectric constant of amorphous film

Sample Number	Metal	$C_A$ (pf)	$R_A$ ( $\Omega$ )	$W$ (Å)	$\epsilon_r$
3	Al(Ni)	657	$8.38 \times 10^5$	504	7.5
5	Al(Au)	1113	$5.54 \times 10^5$	133	3.3
8	Al(Cu)	1489	$4.32 \times 10^5$	217	7.3
6	Au	1183	$1.02 \times 10^6$	259	6.9

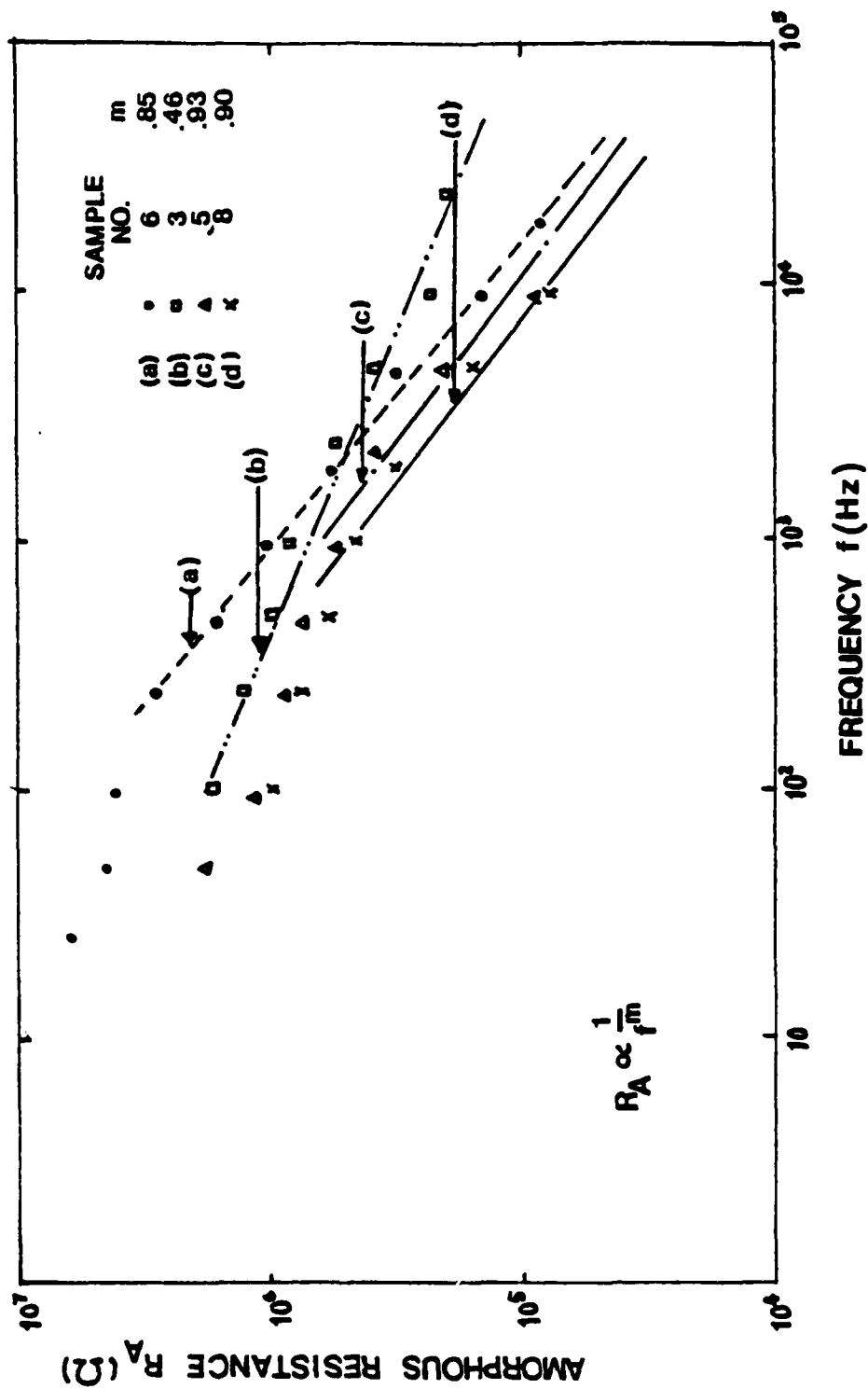


Fig. 5.8 The amorphous resistance verse frequency at zero bias.

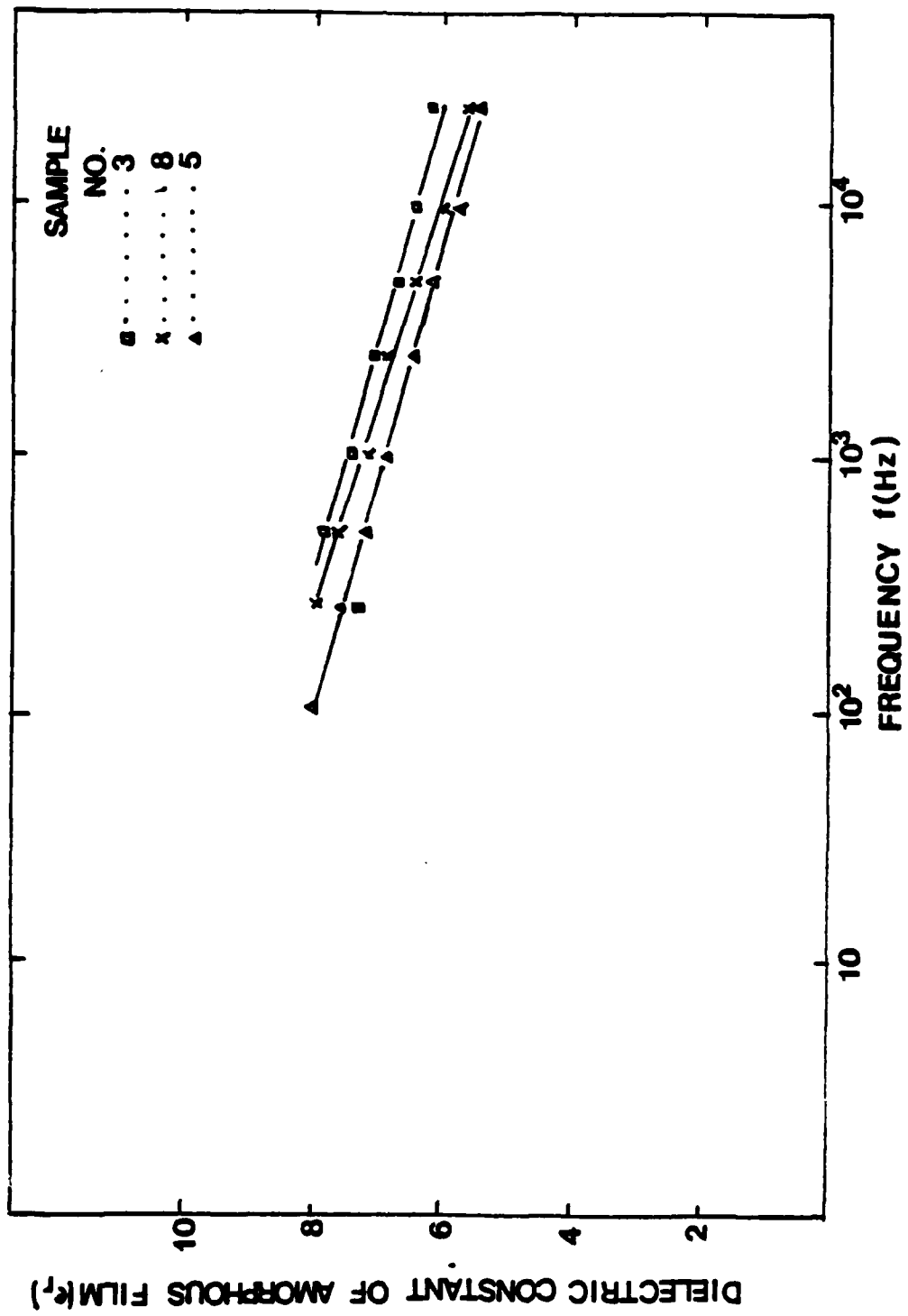


Fig. 5.9 Frequency dependence of the dielectric constant for the film.

$$m = d(\ln \sigma) / d(\omega) = 1 - 4 / \ln(v_{ph} / \omega) \text{-----} (5.2)$$

where  $\sigma$  is the conductivity of the amorphous semiconductor,  $\omega = 2\pi f$  is the frequency of the measuring signal, and  $v_{ph}$  is a phonon frequency (typically on the order of  $10^{13} \text{S}^{-1}$ ). Theoretically,  $m$  is calculated to be 0.8 at approximately 10KHz. The experimental value of  $m$  was measured to be  $0.79 \pm 0.22$  at a frequency of 10KHz. This result supports the hypothesis regarding the amorphous nature of the interlayer.

The dielectric constant of amorphous GaP was calculated by using the amorphous film width, and the capacitance  $C_A$  obtained by C-f measurement. This information was not available in the literature. The frequency dependent curves of the dielectric constant are plotted in Fig, 5.9 for various samples.

The experimental values of diode factors reported<sup>66,67</sup> for real Schottky diodes are generally much larger than the ideal value of unity. Our study reinforced these results and the average value of diode factors was found to be  $1.41 \pm 0.10$ . We attribute the higher value of the diode factor to the existence of the amorphous film in the diode. At forward-bias, the d.c. equivalent circuit of a real Schottky diode is shown in Fig. 5.1 (c). The total voltage drop across the real diode,  $V$ , consists of two components,  $V_D$ , and  $V_A$ .  $V_A$  is the voltage drop on the amorphous region and  $V_D$  is the voltage drop on the ideal diode D. We neglect the voltage drop on the contact resistor because it is very small when compared with  $V_D$  and  $V_A$ .

The total current  $I$  in the diode  $D$  can be given by

$$I = I_{OD} \exp(V_D / n_D V_T) \text{-----} (5.3)$$

where  $I_{OD}$  is the reverse saturation current of an ideal diode and  $n_D$  is the ideal diode factor which is unity. Referring back to section 5.2, the  $I$ - $V$  characteristics of the amorphous film can be approximated by an exponential form at high current injection as given by Eq. (5.1). Combining Eqs. (5.1) and (5.3) and with the fact that  $V = V_D + V_A$  yields;

$$I = I_0 \exp(V / (n_D + n_A) V_T) = I_0 \exp(V / n V_T) \text{-----} (5.4)$$

$$\text{where } I_0 = I_{OD} (I_{OA} / I_{OD})^{(n_A / n)}$$

where  $n = n_D + n_A = 1 + n_A$  is the diode factor generally measured experimentally. Eq. (5.4) demonstrates that a higher value of diode factor usually measured can be attributed to the existence of an amorphous film.

The  $I$ - $V$  curves of sample Nos. 3 and 8, as shown in Fig. 5.10 indicate that sample No. 3 needed an additional voltage ( $\Delta V$ ) in order to obtain the same current level as that of sample 8. As listed in Table 5.1, it is clear that the barrier heights of sample Nos. 3 and 8 obtained from  $I$ - $V$  measurements are almost identical. It is reasonable to assume that the voltage drop on the ideal diode  $V$  is the same for both samples. The only difference between them is that the amorphous film in sample No. 8, ( $W=217 \text{ \AA}$ ) is much thinner than that of

sample No. 3, ( $W=504 \text{ \AA}$ ). Sample No. 8 must have a smaller amorphous resistance than that of sample No. 3, and the additional voltage drop, ( $\Delta V$ ) on the latter is actually dropped across the amorphous resistor  $R_A$ . Therefore, a plot of  $\Delta V$  against the current density  $J$  obtained from Fig. 5.10, shown in Fig. 5.11 is actually the indirect plot of I-V characteristics of the excessive amorphous resistor in sample No. 3, as compared with that of sample No. 8. An exponential function is shown in Fig. 5.11, and this experimentally verifies the I-V characteristics of the interlayer modeled by Eq. (5.1). The above argument is proof that the film which exists between the metal and semiconductor of a real Schottky diode has characteristics of an amorphous nature.

Based on the MAS structural model, extrinsic surface states on the semiconductor surface would be created before an amorphous film is formed. Our model strongly supports the defect model which explains the origin of Fermi-level pinning of real Schottky barriers, and can be combined with the defect model to explain the transition in interface behavior<sup>66</sup> between covalent and ionic semiconductors. Fig. 5.12 illustrates the significant of chemical reactivity in Schottky barrier formation.  $S$ , indicated in Fig. 5.12, is the index of interface behavior as defined by Kurtin, et al<sup>79</sup>.  $\Delta H$ , in Fig. 5.12, is the chemical heat of semiconductor formation which can emphasize the role of interface reactivity. From Fig. 5.12, it can be noted that covalent semiconductors have a heat of formation smaller than 40Kcal/mole, whereas the heat of formation for a metal on a semiconductor is generally larger than 60Kcal/mole<sup>80</sup>. When metallic atoms

are deposited on the semiconductor, the energy ( $>60\text{Kcal/mole}$ ) transferred from the atoms to the semiconductor during the condensation is larger than the heat of semiconductor formation ( $<40\text{Kcal/mole}$ ). This energy must be dissipated, and thus, the bonds of the semiconductor surface atoms would break. The result would be a random interdiffusion of metal and semiconductor at the interface and the formation of amorphous interlayer, as well as creating surface defects on the semiconductor. The Fermi-level is then pinned by these surface defects. On the other hand, semiconductors with a heat of formation larger than  $60\text{Kcal/mole}$  are much more stable, because the condensation heat of a metal is generally not large enough to break the atomic bonds of these semiconductors during the Schottky barrier formation. The formation of an amorphous layer and creation of surface defects are not likely to happen in these semiconductors. The magnitude of the barrier heights formed on these semiconductors is highly dependent upon the difference between the work function of the formation between  $40\text{Kcal/mole}$  and  $60\text{Kcal/mole}$  are within the transition region.

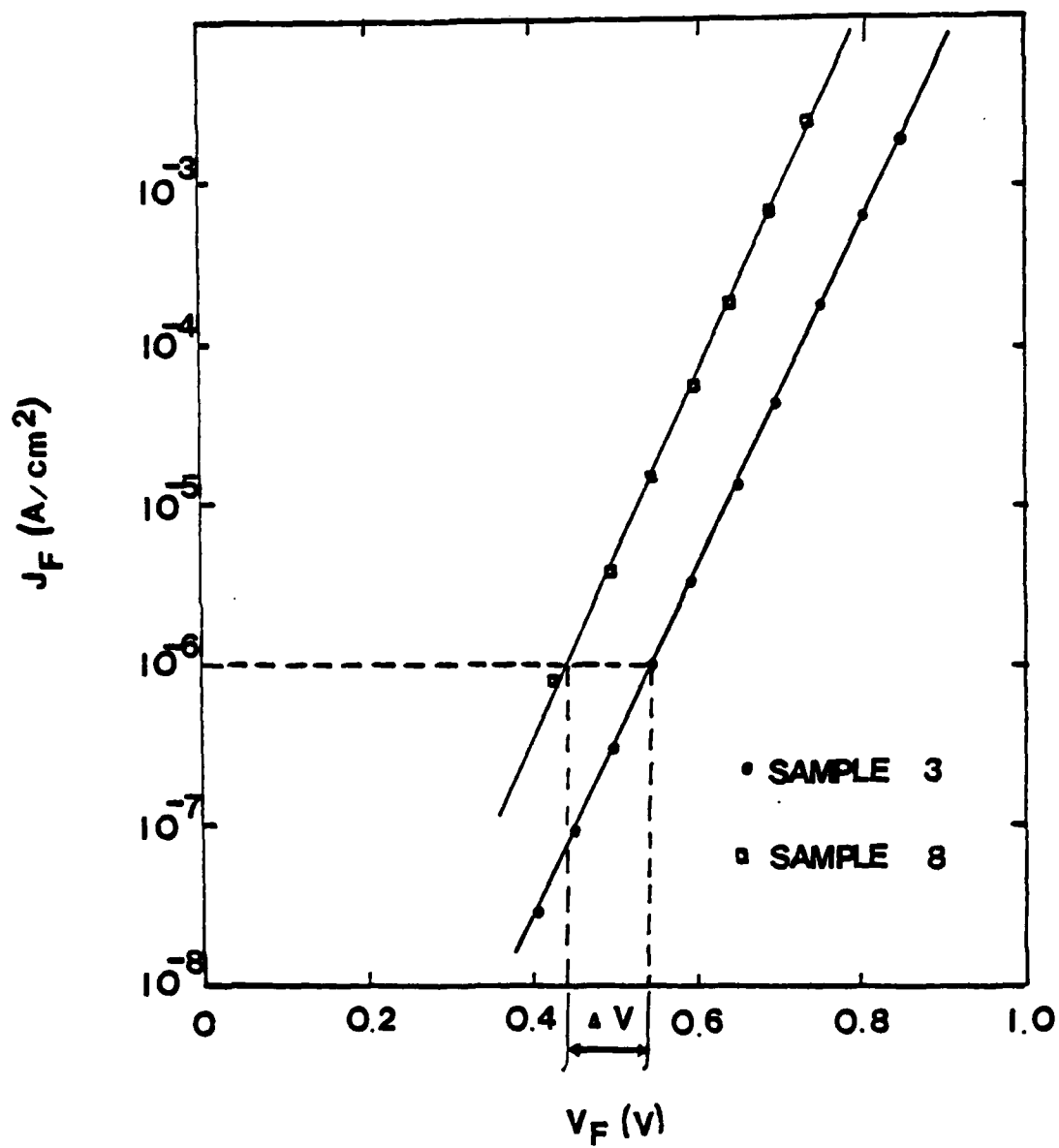


Fig. 5.10 I-V characteristic of sample Nos. 3 and 8.

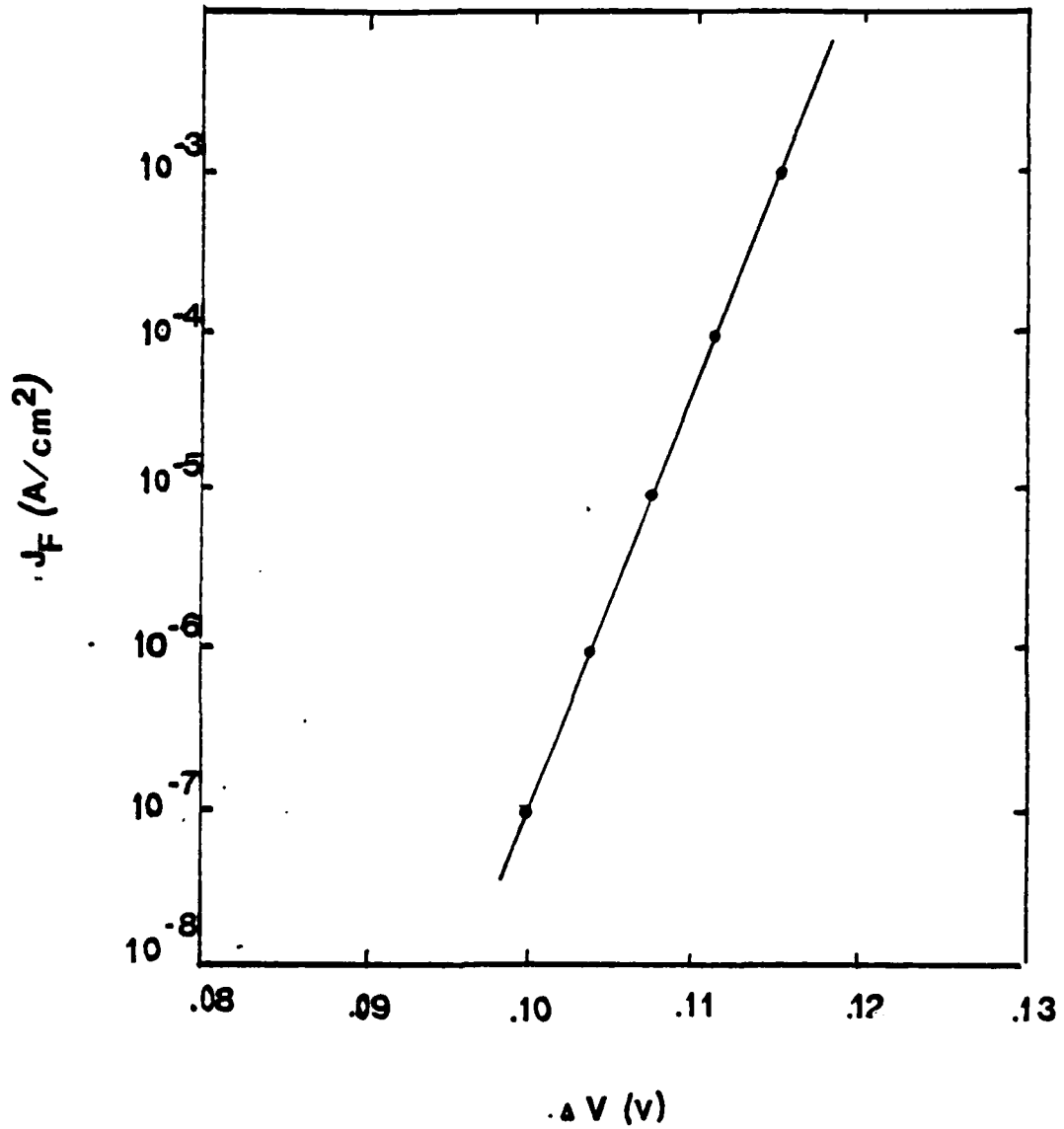


Fig. 5.11

$J_F$  verse  $\Delta V$ .  $J_F$  is the same as Fig. 5.10,  $\Delta V$  was obtained from Fig. 5.10 and it is the difference between the forward bias voltage of sample Nos. 3 and 8 at the same current.

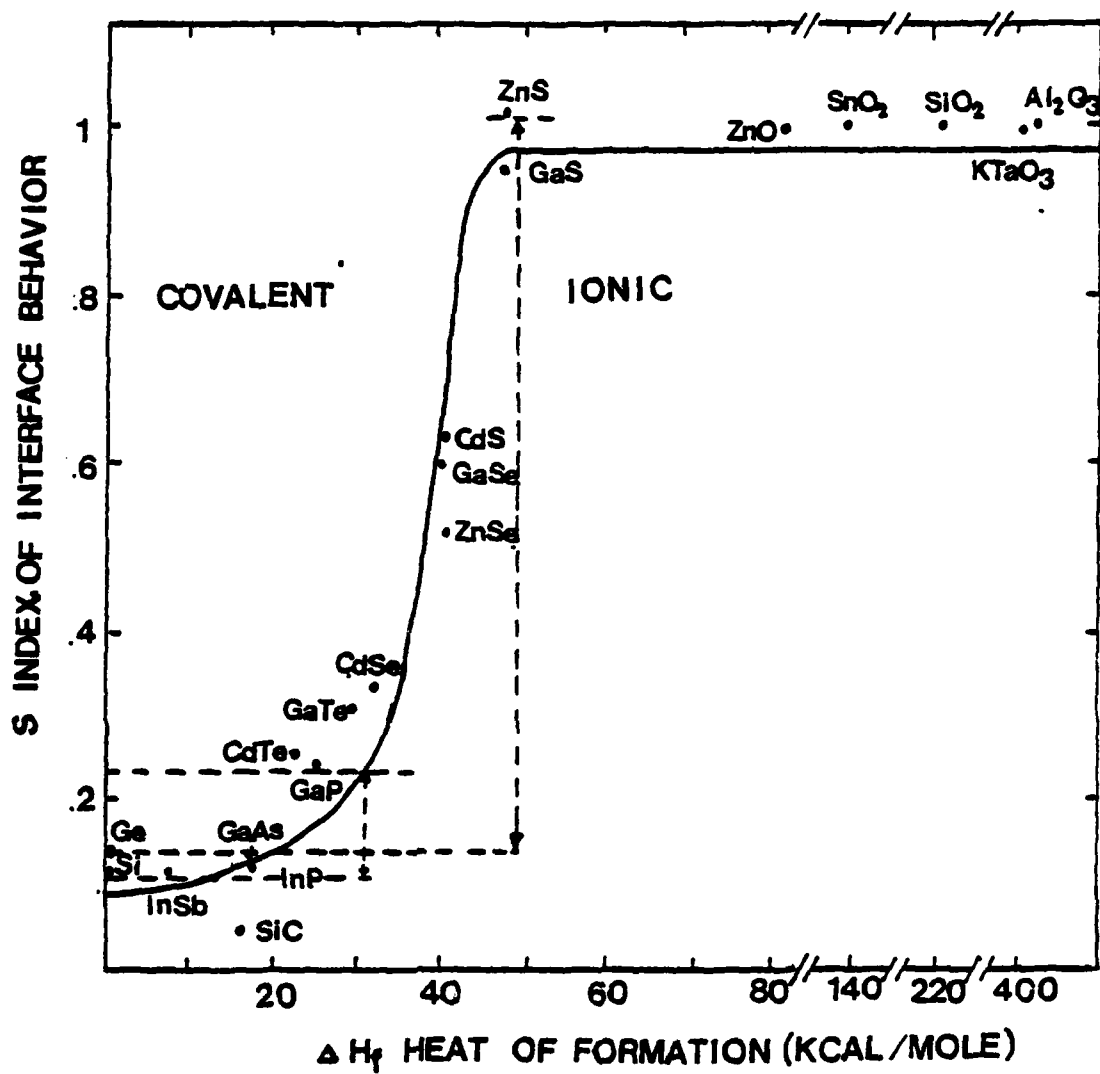


Fig. 5.12

Interface behavior S values plotted vs. chemical heat of formation. Interface behavior S values taken from Ref 79 and heat of formation  $\Delta H_f$  values taken from Ref 66.

## 5.5 Conclusions

A metal-amorphous film-semiconductor (MAS) model is suggested to be the physical structural model of a real Schottky diode. Based on this structural model, all the experimental results obtained from GaP (111) Schottky diodes can be explained. The higher Schottky barrier heights generally obtained by C-V methods than those obtained by other methods including I-V and photo emission can be explained by the existence of the amorphous interlayer in the diode. The deviation of diode factor from its ideal value can be attributed to this amorphous film. The existence of the amorphous layer has been demonstrated and material properties such as the resistivity and the dielectric constant of the amorphous film have been obtained experimentally. The structural model and the defect model are combined to explain the origin of Fermi-level pinning and the transition of interface behavior between the covalent and ionic semiconductors.

## CHAPTER 6

## INVESTIGATION OF SURFACE-SCATTERING LOSSES OF GaAs WAVEGUIDE

## 6.1 Introduction

Integrated optics is based primarily on the fact that light waves can propagate through, and be confined by very thin layers of dielectric materials. All optical functions must be obtained in a single material in monolithic integrated optics. These optical functions can be categorized as light generation, coupling, modulation, guiding and detection. III-V semiconductors are the most promising crystal family for monolithic integrated optics due to their high electro-optic coefficients and good electrical properties. These materials are also compatible with the most highly advanced fabrication techniques, including epitaxial growth<sup>81</sup>, diffusion<sup>82,83</sup>, ion implantation<sup>84</sup> and ion-beam sputtering.

Two approaches can be used to achieve the integration of optical circuits. One is to fabricate integrated optical components using materials best suited for each specific device, and then integrating all of the components into a circuit using an appropriate substrate. There are serious problems of coupling between various components using this technique, and it is difficult to achieve a high degree of integration. The other approach is to fabricate all optical components on a single substrate. This approach simplifies the problem of coupling between various

components and can achieve a very high degree of integration. There are, however, still problems. The most promising substrate material is GaAs, which has the electrical and optical properties potentially suitable for achieving high level integrated optics. The optical transmission losses in GaAs still cannot be reduced to an acceptable level (a few decibels per centimeter) by the present technologies for material preparation. A detailed understanding of the magnitude of the propagation loss in semiconductor waveguides at various wavelengths, is not available. It becomes important to gain a quantitative understanding of the surface and interface properties of the III-V compound semiconductors in order to develop a fabrication technology analogous to that of silicon in integrated electronics.

In this chapter, the results of a quantitative characterization of the surface geometry for semiconductor waveguides is reported. This surface geometric information will be correlated to formulate the calculation of the parameters in the surface scattering theory and to obtain theoretical data on scattering losses.

## 6.2 Surface Scattering and Losses

The foremost barrier in integrated optics is that the optical propagation losses in III-V compound semiconductor waveguides cannot be reduced to an acceptable level. The most important losses in a wave propagation along a thin film waveguide are (1) scattering from rough surfaces of the waveguide during the internal reflection along the zigzag path, and (2) band-to-band transitions. Losses caused by the first mechanism can be reduced by making the surface of the waveguide as smooth as possible. Losses caused by the second mechanism can be minimized by a proper choice of the energy gap of the guiding material relative to the operating wavelength.

As reviewed in section 2.2.2, a theoretical calculation of the surface scattering of a symmetric slab waveguide was reported by Marcuse<sup>16</sup> based on mode conversions to the guided and radiation modes. His results needed further approximation for practical application. A simple theory of the surface scattering for a symmetric waveguide developed by Tien, et al.<sup>18</sup> was introduced in section 2.2.3 and will be used to calculate the scattering loss of a rib waveguide. Rib waveguides are useful for lateral confinement and inter-connections<sup>85</sup> in monolithic integrated optics. As shown, Fig. 6.1 is a rib waveguide, comprised of a lightly-doped ( $10^{15} \text{ cm}^{-3}$ ) GaAs film of height  $t$ , refractive index  $n_f$  with a rib of width  $w$  and height  $\Delta h$  etched into this lightly-doped film. This structure is sandwiched between a highly-doped ( $3 \times 10^{18} \text{ cm}^{-3}$ ) GaAs substrate of refractive index  $n_1$  and air of refractive index  $n_2$ , where both  $n_1$

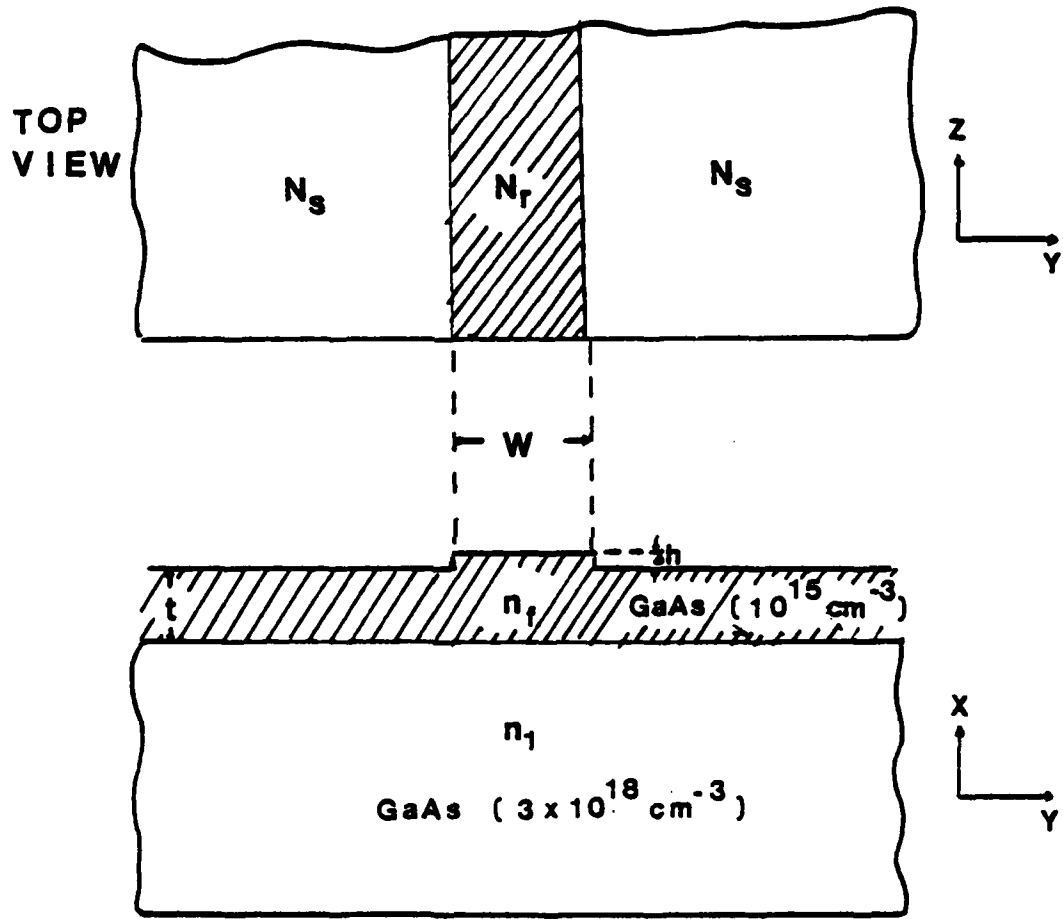


Fig. 6.1 Cross section (x,y) and top view (y,z) of a rib waveguide. The effective indices  $N_r$  and  $N_s$  of the rib and the surrounding regions.

and  $n_2$  are smaller than  $n_f$ . The presence of free carriers in a semiconductor reduces the refractive index of the material. This effect is sufficiently strong in n-type GaAs to enable wave confinement. The depression of the refractive index is primarily due to the negative contribution of the free-carrier plasma to the dielectric constant. This contribution for n-type GaAs is given<sup>86</sup> by

$$\Delta n = -9.6 \times 10^{-21} N/nE^2 \text{-----} (6.1)$$

where  $N$ ,  $n$  and  $E$  are the free-carrier concentration, the index of refraction of pure material, and the energy of guiding wave, respectively. The rib shape provides the lateral confinement, and will be discussed later.

The analysis of dielectric rib waveguides is much more complex than that of planar guides, and no exact analytic solutions for the modes of rib waveguides are available. A simple model, the effective index approximation first introduced by Knox and Toullos<sup>87</sup>, is followed for determining the characteristics of the waveguide. This method is closely related to the approximated analytical approach developed by Marcatili, as introduced in section 2.2.4.

Local solutions for the  $y$  dependence are solved first and are used to determine the  $x$  dependence of the effective refractive index  $N_e$ . The effective index model attributes the effective refractive indices to the rib ( $r$ ) region ( $N_r$ ) and to the region ( $s$ ) surrounding the rib ( $N_s$ ), as shown in the top view of the Fig. 6.1.

The effective refractive indices describing the r and s regions are determined by

$$N_e = (\beta\lambda/2) \text{ ----- (6.2)}$$

where  $\lambda$  is the incident wave length in free space. The propagation constant  $\beta$  in the uniform-layer problem is defined by

$$\beta = \sqrt{(n^2 k^2 - k_y^2)} \text{ ----- (6.3)}$$

where  $k = 2\pi/\lambda$ ,  $n$  is the refractive index in the guiding layer, and  $k_y$  is the y component of propagation vector in the guiding layer.

Taking  $S_i$  as a real function of  $k_y$ ,

$$S_i = \sqrt{(n^2 - n_i^2) k^2 - k_y^2} \text{ ----- (6.4)}$$

The subscript  $i$  designates the layer bounding the guiding layer (Fig. 6.1).  $i=1$  denotes the substrate layer and  $i=2$  denotes the cover layer.

There are two families of modes ( $E_{pq}^x$  and  $E_{pq}^y$ ) that the waveguide can support, as described in section 2.2.4. For the  $E_{pq}^x$  mode, the transcendental equation is similar to Eq. (2.95),

$$\tan k_y t = k_y (S_1 + S_2) / (k_y^2 - S_1 S_2) \text{ ----- (6.5)}$$

This can be used to evaluate the y component of the propagation vector ( $k_y$ ) within a guiding layer of thickness  $t$ . The effective refractive indices of the rib region ( $N_r$ ) and of the surrounding region ( $N_s$ ) is then obtained using equations (6.2) and (6.1).

The x dependence of the field with the artificial boundary conditions imposed at the edges of the rib at  $x=\pm 1/2W$  is proportional to

$$\cos(k_x X) \text{ for } |X| < 1/2 W$$

$$\text{-----}(6.6)$$

$$\exp(-|S_3 X|) \text{ for } |X| > 1/2 W$$

where  $S_3$ , a real function of  $k$ , is determined by  $\beta_r$ ,  $\beta_s$  and  $k$  through the following equation,

$$S_3^2 + k_x^2 = \beta_r^2 - \beta_s^2 \text{ -----}(6.7)$$

where  $k_x$  is the x component of the propagation vector and can be solved using transcendental equation given by Eq. (2.93); e.g.

$$\tan k_x W = 2 k_x S_3 / ((N_s/N_r)^2 - S_3(N_r/N_s)^2) \text{ -----}(6.8)$$

A computer program, (see appendix), can be used to obtain  $k_x$  and  $k_y$ . Once  $k_x$  and  $k_y$  are obtained, the propagation constant of the rib waveguide can be obtained using Eq. (2.91).

Consider a plane wave incident on the upper surface of the rib covering the width ( $W$ ) of the rib in the  $y$  direction, as shown in Fig. 6.1. To cover a unit length of the rib in the  $z$  direction, the plane wave has a width of  $\cos\theta$  in the direction parallel to the wavefront. The incident power  $P$  carried by the plane wave can be given

$$P = (1/2) n A^2 W \sqrt{\epsilon_0 / \mu_0} \cos\theta \quad \text{-----} (6.9)$$

where  $A$  is the field amplitude, and  $\epsilon_0$  and  $\mu_0$  are the permittivity and magnetic permeability of free space, respectively. The power loss  $\Delta p$  at two interface is given by

$$\Delta p = (1/2) n A^2 K^2 \cos^3\theta W \sqrt{\epsilon_0 / \mu_0} \quad \text{-----} (6.10)$$

$$\text{with } K = 4\pi / (\sigma_{r1}^2 + \sigma_{r2}^2)^{1/2}$$

where  $\sigma_{r1}$  and  $\sigma_{r2}$  are the standard deviation of the interfaces between the rib and cover layers, respectively. The total power  $P$  transmitted in the  $z$ -direction is given by

$$P = n \sin\theta A^2 / (4\sqrt{\mu_0 / \epsilon_0}) (t + \Delta h + 1/s_1 + 1/s_2) (w + 2(K^2 + s_3^2) / (s_3(N_s/N_r)K^2 + s_3^3(N_r/N_s)^2)) \quad \text{-----} (6.11)$$

The power attenuation per unit length of the rib waveguide by means of surface-scattering losses is then given by

$$\alpha = K^2 (\cos^3 \theta / \sin \theta) (t + \Delta h + l/s_1 + l/s_2)^{-1} (w + 2(K^2 + s_3^2) / (s_3 (N_s/N_r)^2 K^2 + s_3^3 (N_r/N_s)^2))^{-1} \text{-----}(6.12)$$

The first term K in the equation depends only on the surface properties of interfaces. The experimental techniques used for investigating the surface properties of interfaces will be discussed in the next section.

### 6.3 Outline of Experiments

Rib waveguide, described in the previous section, was used to investigate the surface-scattering losses of III-V compound semiconductor waveguides. The waveguide can be prepared on highly-doped n-type GaAs crystals. Both (111) and (100) orientations of GaAs wafers were used. The doping concentrations of these wafers were determined by resistivity measurements which were carried out by the four-point probe<sup>27,28</sup> and Van-der Pauw<sup>29</sup> methods, as stated in section 3.4.1. The GaAs crystals are 1.5 in.-diameter by 0.02 in.-thick wafers, and chemo-mechanically<sup>89</sup> polished with 0.075% bromine-in-methanol solution using a PAN-W polishing cloth. Five samples were cut from the same wafer by cleaving. These samples with surface areas varying from about 2.5 to 3 cm<sup>2</sup> were cleaned in an ultrasonic cleaner using trichloroethylene, acetone, methanol and D.I.-water, and then attached to a sample holder using Apiezon wax. Different degrees of surface roughness were obtained by polishing the samples with alumina powders of different particle sizes. Five different sizes, 0.05, 0.3, 0.5, 1.0 and 3.0 μms, were used. A new polishing cloth was installed once the size of polishing powders was changed. The speed of the polisher was set at a fixed rate for each polishing process. The sample holder was manually controlled to provide a random motion. Distilled water was used in the polishing process. After 4 minutes of polishing, the samples were removed from the sample holder using trichloroethylene and rinsed in an ultrasonic cleaner using acetone, methanol and D.I.-water. The samples were blown dry with nitrogen and ready for surface roughness analysis.

Laser scattering techniques<sup>23</sup>, described in section 3.2, were performed to characterize the surface geometry of the GaAs substrates. The incident laser beam of 0.5mm beam diameter scanned over an area of  $9\text{mm}^2$  around the center of each sample. Five locations of each sample shown in Fig. 3.4 were first rotationally scanned by the incident beam. The directions at which the maximum and minimum scatter occurred were determined. Each sample was then scanned translationally along these two directions separately. The average BRDF value by averaging the BRDF values in these two directions was obtained. The average BRDF value quantitatively characterizes the degree of surface roughness.

The last stage of the work is the fabrication of the rib waveguide and the study of the optical propagation losses of such waveguides. The first step of this stage is to grow a lightly-doped ( $\sim 10^{15}\text{cm}^{-3}$ ) GaAs thin film ( $\sim 2\mu$ ) upon the substrates. In order to preserve the original surface morphology of the substrates, the only possible growth technique can be used is molecular beam epitaxy (MBE). The growth rate of this technique can be controlled in the molecular order such that the surface morphology of the substrates can be kept. The next step is to form the rib on the lightly-doped thin film. As described in section 3.3, anodic oxidation<sup>25,90,91</sup> can be used in forming the rib geometry with a rib of width ( $w=3\mu$ ) and height ( $\Delta h=.2\mu$ ) etch into the thin film. Then the optical propagation losses of such waveguides will be measured and be used to develop the correlation between the surface roughness obtained from laser scattering measurements and surface-scattering parameters  $\sigma_{r1}, \sigma_{r2}$  and K.

#### 6.4 Results and Discussion

The carrier concentrations of GaAs wafers in (100) and (111) directions determined by resistivity measurements were  $2.4 \pm .2 \times 10^{18} \text{ cm}^{-3}$  and  $2.1 \pm 0.3 \times 10^{18} \text{ cm}^{-3}$ , respectively. According to equation 6.1, the depressions of the refractive index from that of the pure material at  $E=1.24\text{eV}$  were  $-4.5 \times 10^{-3}$  and  $-3.7 \times 10^{-3}$  for (100) and (111) orientations, respectively. The refractive index change between pure and the n-type wafers are large enough to confine the light vertically if a pure or lightly-doped layer of sufficient thickness can be fabricated on the n-type GaAs substrates.

10 samples were quantitatively analyzed by laser scattering technique. They were labeled in accordance to the crystal orientation of the substrate and the grit size of the polishing powders which were used to generate the surface roughness. As stated in Section 3.2, five locations of each sample depicted in Fig. 3.4 were first rotationally scanned by the incident beam. A circular plot of scatter intensity vs. rotation angle was obtained for each sample, as shown in Fig. 6.2. The curve provided a visual impression of the directions at which the maximum and minimum scatter occurred. Each sample was then translationally scanned by the incident beam along the maximum and minimum scattering directions separately. In Fig. 6.3, a three-dimensional plot shows the BRDF values of the sample scanned by the incident beam along one of the two directions. As shown in Fig. 6.4, average plots were made by averaging perpendicular to the direction of scan, and an average line was obtained. Finally, the overall

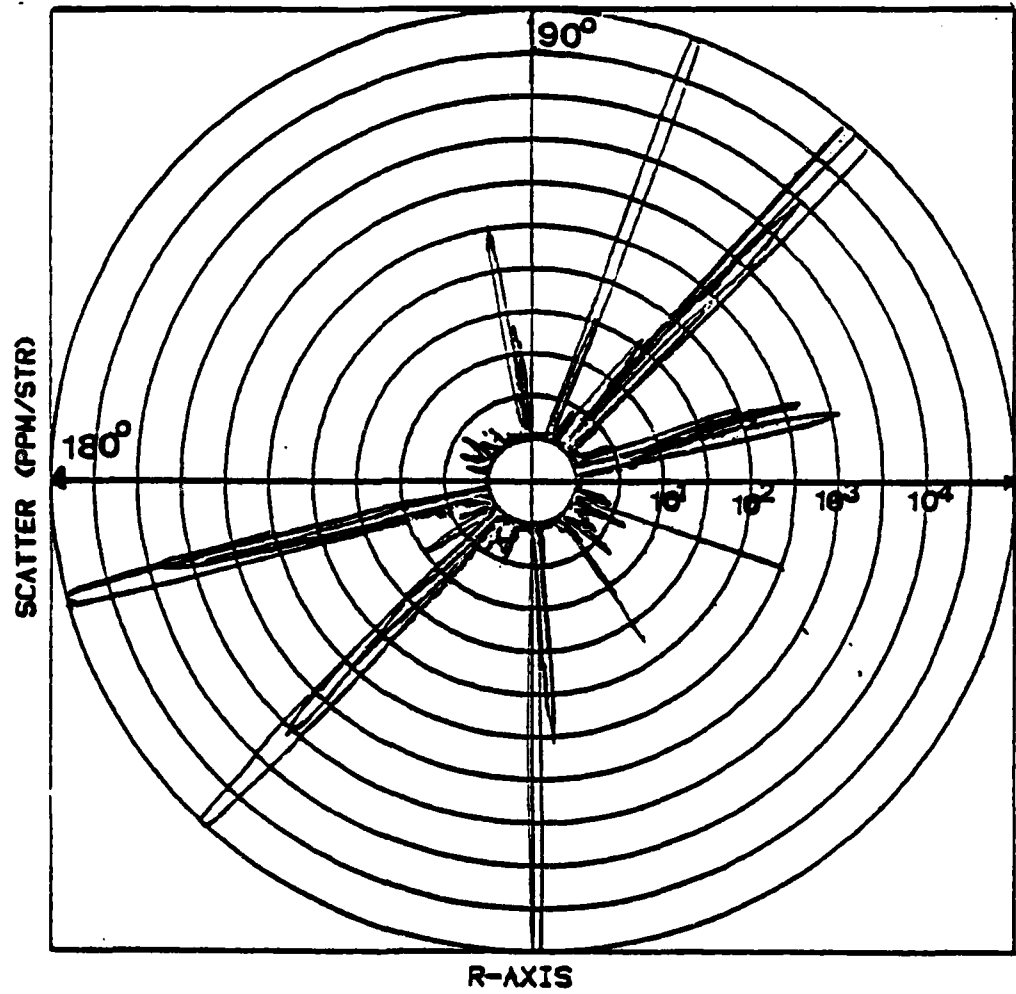


Fig. 6.2

A circular plot of intensity vs. rotation angle  
for sample No. 1.

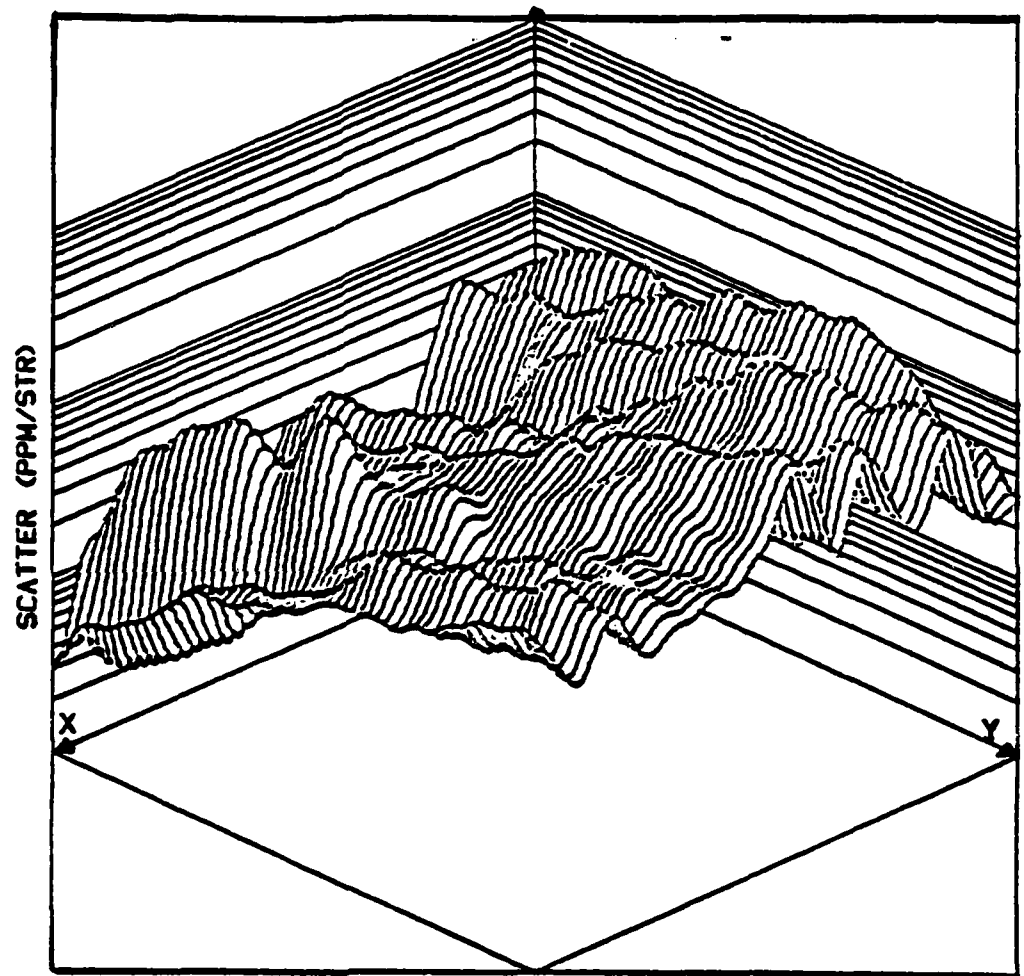


Fig. 6.3

The BRDF values of sample No. 1 obtained by scanning along the direction where maximum scattered occurred.

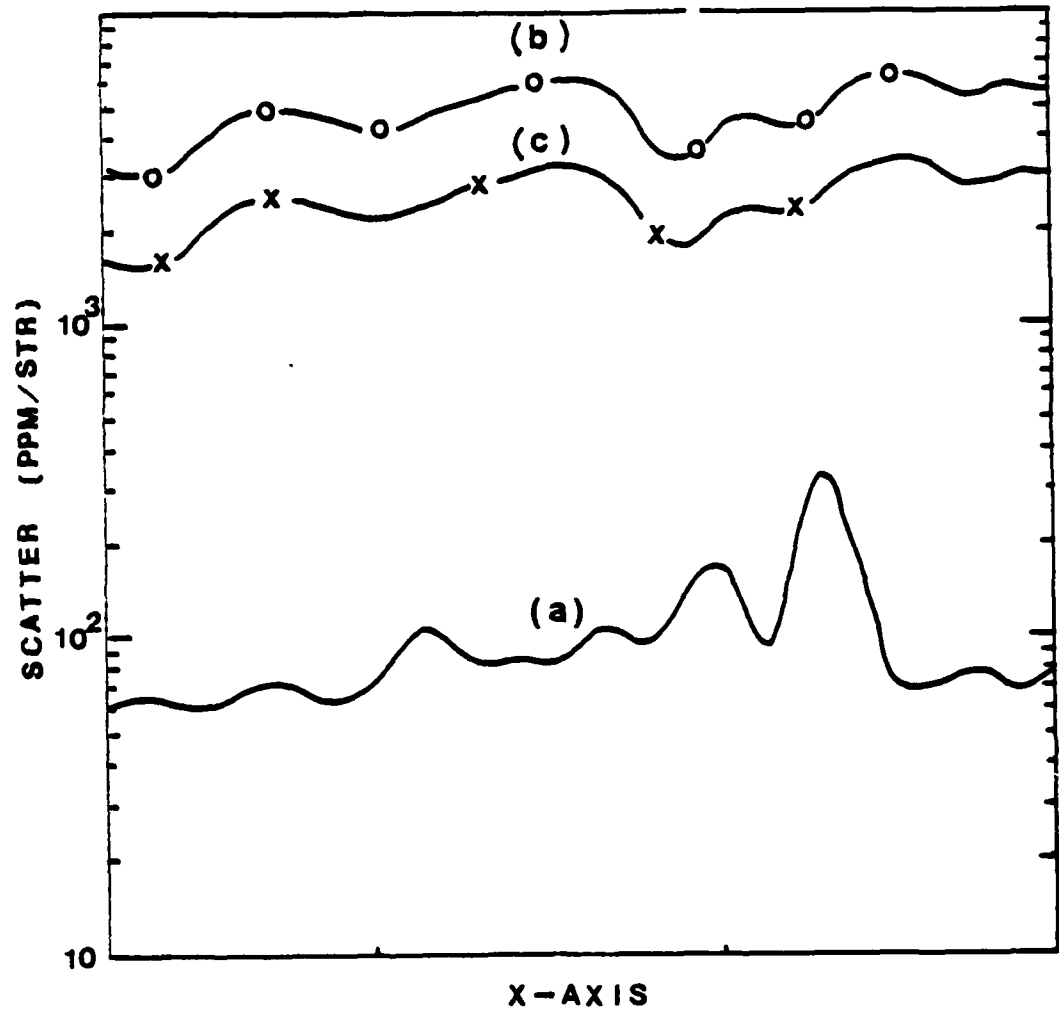


Fig. 6.4

Average BRDF values obtained by averaging perpendicular to the direction of scan where (a) is along the minimum scatter direction, (b) is along the maximum direction and (c) is the average of (a) and (b).

average scattered number (BRDF) as listed in Table 6.1 was obtained which quantitatively represented the degree of surface roughness of each sample. Samples 1 through 5 and samples 6 through 10 were cleaved from the same GaAs(100) and GaAs(111) wafers, respectively. They were polished through the same procedure. The only different parameter in the entire procedure between samples 1 through 5 was the size of powders used to polish them. The overall average scattered number (average BRDF) experimentally obtained for each sample was plotted against the size of the powders used to polish it as shown in Fig. 6.5. Similar plot for samples 6 through 10 was shown in Fig. 6.6. Both figures showed that the degrees of surface roughness of the samples were proportional to the grit size of the powder. The linear correlation between grit sizes shows that laser scattering technique can give a quantitative characterization of the degrees of surface roughness.

The last stage of the experiment is currently on going. Further work is needed in order to complete the measurements of the signal losses of the waveguides with different degrees of surface roughness, the development of the correlation between the surface roughness and the surface-scattering parameters and finally, the investigation of the optical properties of the waveguides.

Table 6.1 Surface Roughness of Samples 1 Through 10.

Sample No.	Label	Orientation	Grit Size( m)	Ave BRDF(PPM/ST)
1	GA100005	100	.05	40.61
2	GA10003	100	.3	2532.28
3	GA10005	100	.5	9235.28
4	GA10010	100	1.0	49523.00
5	GA10030	100	3.0	352.89
6	GA11103	111	.3	1170.61
7	GA11105	111	.5	12114.82
8	GA11110A	111	1.0	15866.00
9	GA11110B	111	1.0	41219.00
10	GA11130	111	3.0	3205.56

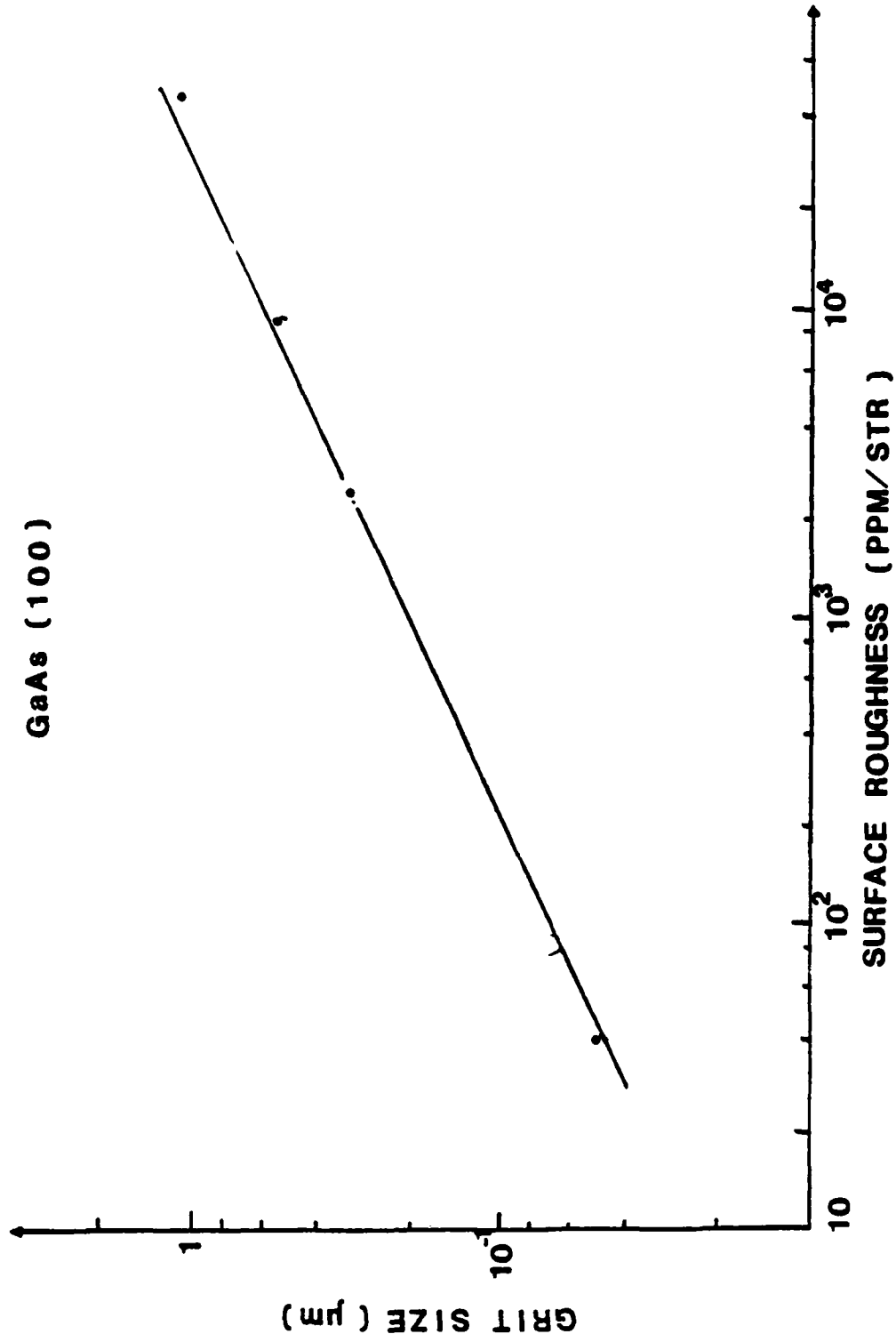


Fig. 6.5 The overall average number (surface roughness) plotted vs. the grit size of polishing powders for samples No. 1 through No. 5.

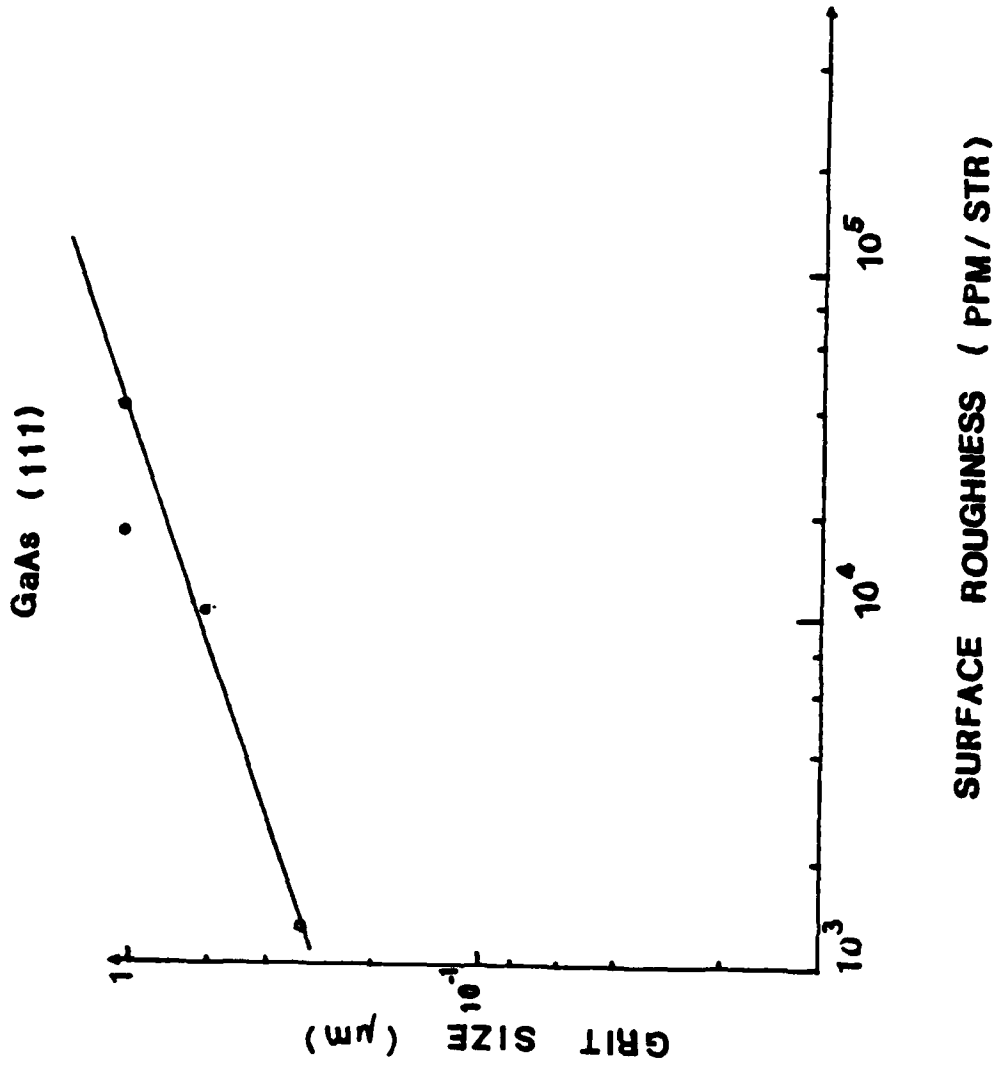


Fig. 6.6 The overall average number of samples No. 6 through No. 10 plotted vs. the grit size ( $\mu\text{m}$ ) of polishing powders.

## CHAPTER 7

## SUMMARY AND CONCLUSIONS

The theoretical formulation for determination of the atomic structure of solid surface by LEED intensity analysis was reviewed. A dynamical multiple scattering computer program provided by S. Y. Tong, et al. was slightly modified for calculating the theoretical I-V curves of GaP (110) face. The intralayer multiple scattering was treated exactly using direct summation method<sup>46</sup> while for the interlayer multiple scattering, the renormalized - forward - scattering (RFS)<sup>47,48</sup> perturbation theory was used. The inner potential was taken to be 8eV and the inelastic damping was set equal to 5eV. The electron-phonon interaction has been incorporated into the theoretical formalism. Both room and low temperatures LEED experimental I-V curves were recorded and essentially identical. I-V curves obtained for the first 16 inequivalent nonspecular beams emerging from the sample were compared with the theoretical curves calculated from 17 different proposed structures. Our study has indicated that the atomic structure of GaP (110) face is quite similar to that of GaAs (110) regarding the ripple geometry. The P atoms are rotated outward from the GaP (110) plane and Ga atoms are rotated inward from the plane by an angle of  $27^{\circ}$  in order to preserve the bond lengths between the nearest-neighbor. Furthermore, the top most layer is compressed by 5% such that the top layer spacing is reduced by approximately  $0.1\text{\AA}$ . The experimental LEED patterns of GaP (111) face were studied. It is concluded<sup>44</sup> that a good Schottky

contact should be relatively easy to obtain on the GaP (111) face. The complete surface structure analysis of GaP (111) is premature and needs further study.

As suggested in the previous LEED studies, Schottky barriers have been fabricated on n-type GaP (111) crystals to study the basic physical mechanism for the metal-semiconductor interaction and formation of Schottky barriers. Capacitance-Voltage (C-V), capacitance-frequency (C-f), current-voltage (I-V) and conductance-frequency were performed to analyze the electrical properties of the Schottky diodes. AES studies were used to study the interface chemical compositions. Strong interdiffusion of the metal and semiconductor atoms at the interface region was observed in the AES studies of Au-GaP and Al-GaP Schottky barriers. Based on the experimental observations, a metal-amorphous film-semiconductor (MAS) configuration is suggested<sup>72</sup> to be the physical structural model of a real Schottky barrier. The composition of the amorphous film is a random mixture of metal and semiconductor atoms. The thickness of this film,  $W$ , determined experimentally from AES depth-composition profiles, is in the range of  $50\text{\AA}$  to  $500\text{\AA}$  depending upon fabrication details. An electrical equivalent model is derived on the basis of the structural model to describe the fundamental behaviors of a real Schottky diode. The deviation of the diode factor  $n$  from its ideal value of unity is usually observed, and it has been demonstrated theoretically that a higher value of diode factor can be attributed to the existence of the amorphous film. The material properties such as the resistivity and the dielectric constant of the amorphous

film have been obtained experimentally. The model has provided a reasonable explanation for the higher Schottky barrier heights generally reported by C-V measurement than those obtained by other methods including I-V and photo emission. Based on the MAS structural model, extrinsic surface states on the semiconductor would be created before an amorphous film is formed, which strongly supports the defect model<sup>68,69</sup> proposed to explain the Fermi-level pinning of a real Schottky barrier. Our MAS model can also be combined with the defect model to explain the transition of interface electronic behavior between covalent and ionic semiconductors. However, our AES result cannot rule out the probability of Fermi-level pinning caused by a contamination of 1% of a monolayer at the metal-semiconductor interface due to the limitation of the Auger sensitivity. Further study, in an interlock system, which has the capability of fabricating Schottky diodes in an UHV chamber on a newly cleaved or ion-sputtering cleaned semiconductor surfaces to eliminate such contamination, is needed and currently underdeveloped. Studies involving different metals and other III-V compound semiconductors may be used in the future to demonstrate the suggested physical structural model of a real Schottky barrier.

The theoretical calculation of surface scattering theory was reviewed. The simple theory<sup>18</sup> of surface scattering and the effective index approximation<sup>87</sup> were used to calculate the surface-scattering losses of a rib waveguide. The doping concentration of the GaAs substrates in (100) and (111) directions obtained by resistivity measurements were  $2.4 \times 10^{18} \text{ cm}^{-3}$  and  $2.1 \times 10^{18} \text{ cm}^{-3}$ ,

respectively. The vertical confinement of the light in the waveguide can be provided if a lightly-doped layer of sufficient thickness is fabricated on the highly-doped GaAs substrates. Different degrees of surface roughness were prepared by polishing the samples with alumina powders of different particle sizes. Laser scattering technique was then conducted to characterize the surface geometry of these samples. The overall average scattered numbers (average BRDF) obtained for all the samples showed that the degrees of surface roughness of the samples were proportional to the grit size used to polish them. We conclude that the laser scattering method can be used quantitatively to characterize the degrees of surface roughness.

Further work, comparing the experimental measurements of the signal losses obtained from the waveguides with different degrees of surface smoothness with the theoretical data of scattering loss, is needed in order to develop the correlation between the surface roughness and the parameters in the surface scattering theory; and finally, to investigate the optical properties of the waveguides.

## REFERENCES

1. J. B. Pendry, in : LOW ENERGY ELECTRON DIFFRACTION (Academic Press, London and New York, 1974).
2. E. A. Wood. J. of Appl. Phys. 35, No. 4, 1306 (1964).
3. N. F. Mott, and H. Jones, in : THEORY OF THE PROPERTIES OF METAL AND ALLOYS (p.65. Dover, New York, 1958).
4. E. L. Blount, Solid State Phys., 13,305 (1962).
5. H. Bethe, Ann. Phys. 87,55 (1928).
6. M. H. Mittleman, and K. M. Watson, Phys. Rev. 113, 198 (1959).
7. B. Lippman, M. H. Mittleman, and K. M. Watson, Phys. Rev. 116, 920 (1959).
8. J. L. Beeby, J. Phys. Cl, 82 (1968).
9. J. Korringa, J. Phys. (France) Suppl. 66 33, 117 (1972).
10. E. G. MacRae, J. Chem. Phys. 45 3258 (1966).
11. L. I. Shift, "QUANTUM MECHANICS", (3rd Edition, McGraw-Hill, 1968) Chap 5.
12. C. B. Duke and G. E. Laramore, Phys. Rev. B2, 4765 (1970).
13. Eq. (6.55) (6.56) in Ref. 1.
14. B. W. Holland, Surface Science, 28, 258-66 (1971).
15. G. E. Laramore and C. B. Duke, Phys. Rev. B2, 4783-95 (1970).
16. D. Marcuse, Bell Syst. Tech. J. 48, 3187 (1969); 48, 3233 (1969); 49, 273 (1970).
17. D. Marcuse, in : THEORY OF DIELECTRIC OPTICAL (Academic Press, New York, 1974), Chap 8.
18. P. K. Tien, Appl. Optics, 10, 2395 (1971).
19. P. Beckmann and A. Spizzichino, International Series of Monographs on Electromagnetic Waves (Oxford, New York, 1963), Chap 5.
20. E. A. J. Marcatili, Bell Syst., Tech. J. 48, 2071-2102 (1969).

21. P. Auger J. Phys. Radium 6, 205 (1925).
22. Chuan C. Chang, in : CHARACTERIZATION OF SOLID SURFACE (Plenum Press, London, N.Y. 1974) Ed. Philip F. Kane and Graydon B. Larrabee, Chap 20.
23. These Measurements were done at the Air Force Base in Dayton, Ohio.
24. William J. Davis, SPIE Vol. 107, 166 (1977).
25. F. K. Reinhart, R. A. Logan and J. P. Lee, Appl. Phys. Lett. Vol. 24, 270 (1974).
26. B. Schwartz, F. Ermanis and M. H. Brastad, J. Electrochem. Soc. 123, 1089 (1976).
27. W. F. Beadle, R. D. Plummer and J.C.C. Tsui, Quick Reference Manual for Semiconductor Energies, to be published.
28. F. M. Smits, Bell Syst. Tech. J.37, 711 (1958).
29. L. J. Van-der Pauw Philips Res. Repts. 13, 1, 1968.
30. S. M. Sze, in : PHYSICS OF SEMICONDUCTOR, (2nd Edition, John Willey & Sons, Inc. 1981).
31. A. R. Lubinsky, B. W. Lee, and P. Mark, Phys. Rev. Lett. 36, 1958 (1976).
32. C. B. Duke, A. R. Lubinsky, B. W. Lee, and P. Mark, J. Vac. Sci. Technol. 13, 761 (1976).
33. A. Kahn, E. So, P. Mark, C. B. Duke, and R. J. Meyer, J. Vac. Sci. Technol. 15, 1223 (1978).
34. S. Y. Tong, A. R. Lubinsky, B. J. Mrstik, and M. A. Van Hove, Phys. Rev. B17(B), 3303 (1978).
35. S. P. Tear, M. R. Welton-Cook, M. Prutton, and J. A. Walker, Surf. Sci. 99,598 (1980).
36. W. E. Spicer, P. Pianetta, I. Lindau, and P. W. Chye, J. Vac. Sci. Technol. 14, 885 (1977).
37. C. R. Brundle and D. Seybold, J. Vac. Sci. Technol. 15, 1186 (1979).
38. P. W. Chye, C. Y. Su, I. Lindau, P. Skeath, and W. E. Spicer, J. Vac. Sci. Technol. 15, 1191 (1979).

39. R. N. Bhargava, Recent Advances in Visible LEDs, I.EEE Trans. Electron Devices, Ed-22, 69 (1975).
40. C. Piaget, P. Saget, and J. Vannimenus, J. Appl. Phys. 48, 3907 (1977).
41. M. Miyao, R. Goto, T. Sukegawa, and M. Hagino, Surf. Sci. 71, 148 (1978).
42. M. Miyao, R. Gogo, T. Fujioka, T. Sukegawa, and M. A. Hagino, Surf. Sci. 86, 888 (1979).
43. A. J. Van Bommel and J. E. Crombeen, Surf. Sci. 93, 383 (1980).
44. B. W. Lee, R. K. Ni, N. Masud, X. R. Wang, and M. Rowe, J. Vac. Sci. Technol. 19 (3), 294 (1981).
45. B. W. Lee, Ph.D. Thesis, Princeton University, January 1976.
46. J. L. Beeby, J. Phys. C. 1, 82 (1968).
47. J. B. Pendry, Phys. Rev. Lett. 27, 856 (1971).
48. S. Y. Tong, Solid State Commun. 16, 91 (1975).
49. L. F. Matheiss, Phys. Rev. 133, A1399 (1964).
50. T. L. Loueks, in : AUGMENTED PLANE WAVE METHOD, (Benjamin, New York, 1967).
51. E. Clementi and C. Roetti, in : ATOMIC DATA AND NUCLEAR DATA TABLES, Vol. 14, 177, Academic 1974.
52. J. C. Slater, Phys. Soc. Jpn. 22, 710 (1951).
53. C. B. Duke, N. O. Lipari, and V. Landman, Phys. Rev. B8, 2454 (1973).
54. Addamiano, J. Am. Chem. Soc. 82, 1537, or G. Giesecke and Pfister, Acta Cryst. 11, 369 (1958).
55. J. J. Lander, in : PROGRESS IN SOLID STATE CHEMISTRY, Vol. 2, (Pergaman Press, London, N.Y. 1965) Ed. Reiss, Chap. 3.
56. A. V. MacRae, Surf. Sci. 4, 247 (1966).
57. E. Zanazzi and F. Jona, Surf. Sci. 62, 61 (1977).
58. C. B. Duke, R. J. Meyer, A. Paton, P. Mark, A. Kahn, E. So and J. L. Yeh, J. Vac Sci Technol. 16, 1252 (1979).

59. J. Bardeen, Phys. Rev. 71, 717 (1947).
60. A. M. Cowley and S. M. Sze, J. Appl. Phys. 36, 3212 (1965).
61. V. Heine, Phys. Rev. 138, A1689 (1965).
62. J. C. Inkson, J. Phys. C5, 2599 (1972).
63. J. C. Phillips, J. Vac. Sci. Technol. 11, 947 (1974).
64. J. M. Andrew and J. C. Phillips, Phys. Rev. Lett. 35, 56 (1975).
65. C. Tejedor, F. Flores and E. Louis, J. Phys. C10, 2163 (1977).
66. L. J. Brillson, J. Vac. Sci. Technol. 15 (4), 379 (1978); Phys. Rev. Lett. 40, 260 (1978).
67. A. Amith and P. Mark, J. Vac. Sci. Technol. 15 (4), 1344 (1978).
68. P. W. Chye, I. Lindau, P. Pianetta, C. M. Garner and W. E. Spicer, Phys. Rev. B17, 2682 (1978); Phys. Rev. B18, 5545 (1978).
69. I. Lindau, P. W. Chye, C. M. Garner, P. Pianetta, C. Y. Su and W. E. Spicer, J. Vac. Sci. Technol. 15, 1332 (1978).
70. W. E. Spicer, P. W. Chye, Dr. P. Skeath, C. Y. Su and I. Lindau, J. Vac. Sci. Technol. 16 (5), 1422 (1979).
71. W. E. Spicer, I. Lindau, P. R. Skeath and C. Y. Su, J. Vac. Sci. Technol. 17, 1019 (1980).
72. B. W. Lee, D. C. Wang, R. K. Ni, G. Xu and M. Rowe, J. Vac. Sci. Technol, 21 (2), 577 (1982).
73. W. E. Spicer, I. Lindau, P. E. Gregory, C. M. Garner, P. Pianetta and P. Chye, J. Vac. Sci. Technol. 13, 780 (1976).
74. A. M. Cowley, J. Appl. Phys. 37 (8), 3024 (1966).
75. A. M. Goodman, J. Appl. Phys. 34, 329 (1963).
76. L. J. Brillson, Phys. Rev. Lett. 35 (5), 245 (1977).
77. P. Nagels, in : AMORPHOUS SEMICONDUCTOR, Topics in Applied Physics, Vol. 36, Ed M. H. Brodsky, Springer-Verlag, 1979, Chap 5.

78. I. G. Austin and N. F. Mott, *Philos. Mag.* 22, 903 (1970).
79. S. Kurtin, T. C. McGill and C. A. Mead, *Phys. Rev. Lett.* 22 (26), 1433 (1969).
80. J. Derrien and F. A. D'Avitoya, *Surf. Sci.* 65, 668 (1977).
81. B. E. Barry, in : *GaAs AND RELATED COMPOUNDS* (Institute of Physics, London, 1971) paper 19
82. F. K. Reinhart, D. F. Nelson, J. McKenna, *Phys. Rev.* 177, 1208 (1969).
83. H. Zoroofchi, J. K. Butler, *J. Appl. Phys.* 44, 3697 (1973).
84. E. Garmire, H. Stoll, A. Yariu, *Appl. Phys. Letts.* 21, 87 (1972).
85. J. C. Shelton, F. K. Reinhart and R. A. Logan, *Appl. Opt.* 17, 2548 (1978).
86. F. Stern, in : *SOLID STATE PHYSICS* (Academic, New York, 1963) edited by F. Seitz and D. Turnbull, Vol. 15, p.327.
87. R. M. Knox and P. P. Toullos, *Proc. symp. Submillimeter Waves, Microwave Res. Ins. symp. ser. 20*, 497 (1970).
88. E. A. J. Marcatili, *Bell Syst., Tech. J.* 48, 1392-1425 (1969).
89. M. V. Sullivan and G. A. Kolb, *Ibid*, 110, 585 (1963).
90. J. C. Shelton, F. K. Reinhart, and R. A. Logan, *J. Appl. Phys.* 50 (11), 6675 (1979).
91. F. K. Reinhart, J. C. Shelton, R. A. Logan, and B. W. Lee, *Appl. Phys. Lett.* 36 (4), 237 (1980).

## APPENDIX

Calculation of the Propagation Constant in a  
Rectangular Waveguide

The following programs calculate the propagation constant  $\beta$  of a waveguide propagating along z-direction in a rectangular dielectric waveguide with dimension a and b as shown in Fig. 2.9. The program uses Newton's method to solve the transcendental equations (2.93) and (2.95), for  $k_x$  and  $k_y$ , respectively. Once  $k_x$  and  $k_y$  are determined, the propagation constant  $\beta$  can be obtained from Eq. (2.97). Programming was in standard fortran IV, and programs have been tested in an IBM 360 under WATFIV compilers.

The first step calculates  $k_x$  and  $k_y$ . Eqs. (2.93) and (2.95) can be written as

$$f(k_x) = k_x a - p\pi - \arctan(n_1^2 s_5 / n_5^2 k_x) - \arctan(n_1^2 s_3 / n_3^2 k_x) \text{-----(A-1)}$$

and

$$f(k_y) = k_y b - q\pi - \arctan(s_2 / k_y) - \arctan(s_4 / k_y) \text{------(A-2)}$$

where the integers p and q indicate the number of maxima of the field distribution in x and y directions. Newton's method for finding zeros of  $f(x)$  is most widely known, and it can be expressed by an iteration process

$$x_{k+1} = x_k - f(x_k) / E'(x_k) \text{-----} (A-3)$$

After  $k_x$  and  $k_y$  are obtained, the propagation constant  $\beta$  can be determined.

COMMENT PROGRAM TO CALCULATE THE PROPAGATION CONSTANT IN A

C RECTANGULAR WAVEGUIDE USING NEWTON'S METHOD

COMPLEX CN1,CKX,CS3,CS5,CDS3,CDS5,CFKX,CFKY

COMPLEX CSQRT,CIN,CEN,CS2,CS4,CDS2,CDS4,CN2

COMPLEX CN3,CN4,CN5,CBETA,CMLX,CATAN

PHI=3.14159625

CN1=CMLX(3.4700,-0.0005)

CN2=1.0

CN3=3.42

CN4=3.4

CN5=3.42

RK=2\*PHI\*1.424/1.44

A=3.0

B=1.0

C THIS SECTION CALCULATES CKX

N=1

P=1.0

CKX=CMLX(0.4027,-0.005)

15 CS3=CSQRT((CN1\*\*2-CN3\*\*2)\*RK\*\*2-CKX\*\*2)

CS5=CSQRT((CN1\*\*2-CN5\*\*2)\*RK\*\*2-CKX\*\*2)

CDS3=(-1)\*CKX\*CN3\*\*2/CN1\*\*2/CS3

CDS5=(-1)\*CKX\*CN5\*\*2/CN1\*\*2/CS5

CFKX=CKX\*A-P\*PHI+CATAN(-CDS3)+CATAN(-CDS5)

CDFKX=A+(CS3\*CN\*\*2/CN1\*\*2-CDS3\*CKX)/(1+CDS3\*\*2)

1/CS3\*\*2+(CS5\*CN5\*\*2/CN1\*\*2-CDS5\*CKX)/(1+CDS5\*\*2)

1/CS5\*\*2

```

CIN=CFKX/CDFKX

CKXN=CKX-CIN

WRITE(6,4)N,CKXN

4   FORMAT(4H, N= ,14,7H, CKXN= ,2E19.9)
    IF(CABS(CIN)-.1E-07)10,17,17

17  CKX=CKXN
    IF(N-200)21,22,22

21  N=N+1
    GO TO 15

22  WRITE(6,23)CKX
23  FORMAT(16H, CHOOSE NEW CKX,2E19.9)
10  WRITE(6,24)N,CKX
24  FORMAT(4H, N= ,14,6H, CKX= ,2E19.9)

COMMENT THIS SECTIONCALCULATE CKY

M=1

Q=1.0

CKY=(1.8334,-0.002)

45  CS2=CSQRT((CN1**2-CN2**2)*RK**2-CKY**2)
    CS4=CSQRT((CN1**2-CN4**2)*RK**2-CKY**2)
    CDS2=(-1)*CKY/CS2
    CDS4=(-1)*CKY/CS4
    CFKY=CKY*B-Q*PHI+CATAN(-CDS2)+CATAN(-CDS4)
    CDFKY+B+(CS2-CDS2*CKY)/(1+CDS2**2)/CS2**2
    I+(CS4-CDS4*CKY)/(1+CDS4**2)/CS4**2

CEN=CFKY/CDFKY

CKYN=CKY-CEN

WRITE(6,44)M,CKYN

```

```
44   FORMAT(4H, M= ,14,7H, CKYN= ,2E19.9)
      IF(CABS(CEN)-.1E-07)40,40,47
47   CKY=CKYN
      IF(M-200)41,42,42
41   M=M+1
      GO TO 45
42   WRITE(6,43)CKY
43   FORMAT(16H, CHOOSE NEW CKY ,2E19.9)
40   WRITE(6,64)M,CKY
64   FORMAT(4H, M= ,14,6H, CKY= ,2E19.9)
COMMENT THIS SECTION CALCULATE CBETA
      CBETA=CSQRT(CN1**2*RK**2-CKX**2-CKY**2)
      WRITE(6,65)CBETA
65   FORMAT(8H, CBETA= ,2E19.9)
      STOP
      END
```

C

```
COMMENT FUNCTION CATAN PROVIDES THE VALUE OF COMPLEX ARCTANGENT
FUNCTION CATAN(CZ)
COMPLEX CATAN,CZ,CMLX,CI
CI=CMLX(0.0,0.1)
X=REAL(CZ)
Y=AIMAG(CZ)
CATAN=ATAN(2*X/(1-X**2-Y**2))/2+CI/4*ALOG((1+Y)**2
1+X**2)/((1-y)**2+X**2))
RETURN
END
```

4-8  
DTI